NANOPATTERNING CHEMISTRY TO CONTROL THE GROWTH OF TRANSITION METAL OXIDES

A Dissertation

Presented to the Faculty of the Graduate School

of Cornell University

In Partial Fulfillment of the Requirements for the Degree of

Doctor of Philosophy

by

Katharine Wanda Oleske

December 2017

NANOPATTERNING CHEMISTRY TO CONTROL THE GROWTH OF TRANSITION METAL OXIDES

Katharine Wanda Oleske, Ph. D.

Cornell University 2017

Despite advances in nanomaterials synthesis, the bottom-up preparation of nanopatterned films as templates for spatially confined surface reactions and nucleation of crystalline inorganics remains a challenge. I developed an approach to fabricating nanoscale thin film surface structures with periodicities on the order of 20 to 50 nm and with the capacity to localize reactions with small molecules and nanoparticles. A block copolymer (BCP) of polystyrene-*block*-poly[(allyl glycidyl ether)-*co*-(ethylene oxide)] (PS-*b*-P(AGE-*co*-EO)) is used to prepare periodically-ordered, reactive thin films. As proof-of-principle demonstrations of the versatility of the chemical functionalization, a small organic molecule, an amino acid, and ultrasmall silica nanoparticles are selectively attached via thiol-ene click chemistry to the exposed P(AGE-*co*-EO) domains of the BCP thin film. My approach employing click chemistry on the spatially confined reactive surfaces of a BCP thin film overcomes the solvent incompatibilities typically encountered when synthetic polymers are functionalized with water-soluble molecules. Moreover, this post-assembly functionalization of a reactive thin film surface preserves the original patterning, reduces the amount of required reactant, and leads to short reaction times. The small molecule functionalized area can subsequently template the confined

crystallization of copper (I) oxide (Cu_2O) and zinc oxide (ZnO) with high fidelity, from aqueous solutions at low temperatures (below 60 °C) with periodicities on the order of 50 nm. The demonstrated method provides a versatile materials platform to control the growth of nanostructured crystalline materials via the introduction of a plethora of surface functional groups. The resulting organic substrates can be used to template the growth and control the crystal orientation and texturing of multiple different crystalline inorganic materials on surfaces nanostructured via BCP self-assembly. The demonstrated approach is expected to provide a new materials platform in applications including sensing, catalysis, pattern recognition, or microelectronics.

BIOGRAPHICAL SKETCH

Katharine “Kasia” Wanda Oleske is from Lancaster, PA. Katharine (hereafter referred to as Kasia) wanted to experience city life and therefore decided to attend the University of Pennsylvania to major in Materials Science and Engineering. With the threat from her mom to work as a lifeguard over the summer once again, she searched for an alternative research job and got her first taste of polymer research in Dr. Karen Winey’s lab in June 2010. Kasia loved her first research experience and went on to explore industry research at both Proctor and Gamble (P&G) and Boeing. After seeing what a career in industry research was like for those with a Ph.D., Kasia decided to apply to graduate schools in Materials Science and Engineering. Kasia enrolled in a Ph.D. program at Cornell University working with Professors Lara Estroff and Ulrich Wiesner. After graduating in December 2017, Kasia plans to work for Pratt and Whitney.

As for the origin of the nickname Kasia, it started off as a childhood nickname replacing her parents’ previous nickname for her “pumpkin.” This is because she is not a pumpkin, she’s Kasia. Kasia is a common Polish name, which translates to Katie or Kathy. This name permeated through all aspects of her life from family to friends, and eventually, even though Kasia is not intuitive to spell or pronounce, everyone called her Kasia.

Kasia’s current aspirations include materials science and engineering, polymer science, and getting a dog. When not in the lab, Kasia enjoys meeting new people, eating with friends, outdoor adventures, and all sorts of sports including soccer, softball, and rugby.

This is dedicated to all the nasty women

ACKNOWLEDGMENTS

I am grateful to Professors Lara Estroff and Uli Wiesner for hiring me as a joint student. I was exposed to so many different aspects of polymer chemistry and biomineralization. Thank you for your support.

Thank you to Professor David Putnam for not only serving on my committee but supporting me throughout my time at Cornell both academically and professionally.

I worked with so many people at Cornell, including two large research groups that I learned such a wide variety of skills from. Thank you to all my group members from both the Estroff and Wiesner groups. From the Estroff Group: Dr. Emily Asenath-Smith, Abby Goldman, Reum Scott, Amnon Ortoll-Bloch, Dr. Coit Hendley IV, Jennie Russ Kunitake, Dr. Netta Vidavsky, Alex Boys, Dr. Fei Wu, Dr. Kate Barteau, Ethan Susca, JooHo Kim, Dr. Joe Carloni, and Konrad Hedderick. From the Wiesner Group: Tom Gardinier, Melik Turker, Dr. Hiroaki Sai, Dr. C Cowman-Eggert, Dr. Kwan Wee Tan, Peter Beaucage, Dr. Tangi Aubert, Yuk Mun Li, Qi Zhang, Teresa Kao, Dr. Joerg Werner, Fumiaki Matsuoka, Dr. Yibei Gu, R. Paxton Thedford, Parth Vaidya, Swathi Rao, Sarah Hesse, Ferdinand Kohle, Josh Hinckley, Dr. Kai Ma, Dr. Yusuke Hibi, and Dana Chapman.

Thank you to Dr. Ivan Keresztes and Tony Condo for keeping the NMR and polymer facilities running smoothly. Thank you to Mick Thomas for all the SEM training and discussions. Thank you to John Grazul for all your support including the excellent assistance and research discussions over the years with TEM sample prep and imaging as well as for all the fun stories and silly but informative emails.

Thank you to my wonderful girlfriend, Dr. Voula Collins, for all your love and support throughout graduate school. You helped me through the hard times and you made the good times even more joyous. I am excited to see where life takes us and

hopefully we can get a dog together soon! Thank you to my loving family, my parents Krystyna and Peter Oleske, and my brother Michael Oleske. Mom and Dad, you two have always supported me throughout my whole life and I am forever grateful to both of you. Thank you to Dr. Karen Winey, Nina Cummings and Julia Bensur for all your support and help during graduate school. Thank you to all my friends including all of those in oSTEM, SWE, my various sports teams, and all the random friends I have made along the way. You all truly made my time in Ithaca special and enjoyable.

Thank you to the U.S. Department of Energy, Office of Science, Basic Energy Sciences for project funding as well as the NSF for support through an IGERT traineeship to support my scientific endeavors.

TABLE OF CONTENTS

LIST OF FIGURES

CHAPTER ONE

CHAPTER TWO

CHAPTER FOUR

LIST OF SCHEMES

CHAPTER TWO

CHAPTER THREE

CHAPTER FOUR

LIST OF TABLES

CHAPTER FOUR

CHAPTER ONE

A REVIEW OF ORGANIC SUBSTRATES TO TEMPLATE INORGANIC NUCLEATION

1.1 Introduction

Over the years, many different methods have been developed for patterning specific chemistries onto various substrates, but far fewer of those have then successfully been used to template inorganic materials growth. Confined surface reactions are explored as a pathway to promote heterogenous nucleation and create nanostructured, crystalline inorganics at low temperatures (below 60°C) where the confined functionality determines the texturing and orientation of the final crystal. The scope of my research was to develop a post-assembly reactive block copolymer thin film method where the attached functional groups not only promoted heterogenous nucleation of a crystalline inorganic confined to one block, but also controlled the final texturing and orientation of the respective inorganic at low temperatures and at standard pressure. This chapter introduces some fundamental concepts of patterning organic substrates via microcontact printing, scanning-probe based methods, and block copolymers, and how these patterned substrates can subsequently be used to template inorganic materials growth.

1.2 Patterning surface chemistry with microcontact printing

Developed by the Whitesides group in 1993, microcontact printing or μCP uses an elastomeric, typically polydimethylsiloxane (PDMS) stamp to transfer the desired chemistry or "ink" material onto a substrate.[1] To create the features on the stamp, first a master pattern is needed, which is typically synthesized by spin coating a photoresist onto a silicon wafer, exposing it to UV light through a mask, and finally

exposing it to a solution of developer. Once the master pattern is made, a solution of prepolymer and curing agent is poured onto the master pattern and cured to crosslink the polymer (Figure 1.1).[2,3]

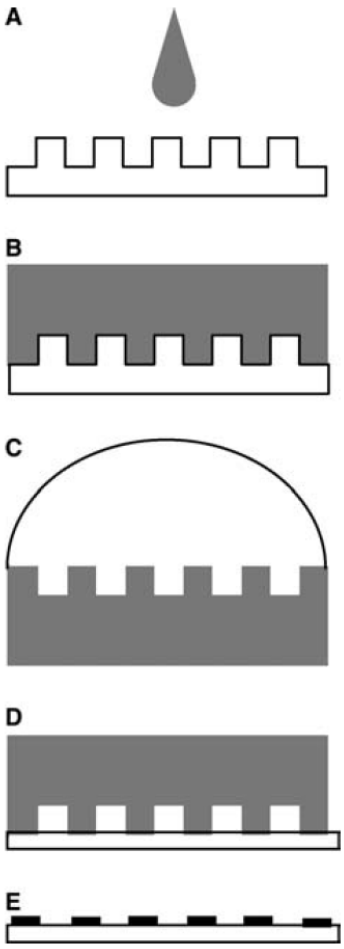

Figure 1.1: Schematic representation of the microcontact printing process. PDMS is applied to a master design (a) and allowed to cure (b), forming a mold/stamp. After peeling the stamp from the master, ''ink'' is applied (c), and the ink is transferred to a substrate (d) by stamping. After removal of the stamp, the ink is patterned on the substrate (e)[3]

Originally μCP was used to chemically pattern gold with alkanethiols to form spatially confined self assembled monolayers (SAMs), but has rapidly grown to allow chemically patterning surfaces with polymers, DNA, or proteins.[4]

A wide variety of polymers, from conducting to biological polymers, have

been used as inks for μCP due to their strong adhesion to the contact area and minimal diffusion into the non-contact area. If a polymer is soluble in a suitable solvent for μCP it can be patterned on a variety of surfaces and attached through electrostatic interactions, covalently, or they can be physisorbed onto substrates depending on the specific polymer and surface.[5–7] Another method to μCP polymers is by depositing an initiator into a pattern, which then serves as a template for graft polymerization to create a microstructured polymer brush pattern.[8–10] One of the first polymers to be microcontact printed was a maleic acid terminated poly(ethylene oxide) onto an amine terminated polyelectrolyte multilayer. A multilevel architecture was achieved by repeated μCP of several polymers.[11] In addition, poly(acrylic acid) was also printed onto a poly(allylamine hydrochloride) substrate with up to 80 nm resolution.[12] These patterns are particularly interesting because of their charge and have been used to pattern anionic PS nanospheres. Hydrophilic/hydrophobic patterns can also be printed.[13]

Polymer patterns can be printed onto substrates using a combined hot embossing/μCP method. First, a layer of the desired polymer is deposited onto a flat PDMS stamp followed by hot embossing the stamp with a negative polymer master. To create the desired polymer pattern, the substrate is then heated above the glass transition temperature of the transferred polymer and the stamp is pressed onto the hot substrate.[14] Patterns of polymer/fullerene photodiodes onto (3,4-ethylenedioxythiophene/poly(4-styrenesulfonate) films as well as polythiophenes onto Au coated surfaces[15] have been synthesized to make organic light emitting devices as well as thin film transistors.[16,17] μCP polymers have also been of interest to biological applications, especially poly(-L-lysine) and RGD functionalized poly(ethylene glycol)-*co*-poly(-L-lysine) for cell adhesion studies.[18,19] Over the years it has been demonstrated that a variety of polymers can be used to direct the attachment of many

different types of cells[20–23] and fibroblasts[24] depending on the printed polymer. Furthermore, DNA can be microcontacted printed using PDMS and PMMA structures.[25]

Not only are patterned polymers and DNA of interest to biological applications, but there is also a strong push towards patterning proteins for cell biology research, biosensors, and tissue engineering.[26–30] The traditional SAMs printing led the way towards being able to pattern proteins but had some versatility issues for biological settings due to requiring access to an evaporator to deposit a layer of gold onto the substrate and some alkanethiols needed to be synthesized in house. In order to be more versatile for biological applications, a technique was developed in order to eliminate the need for SAMs.[31] On the millimeter length scale, a PDMS master pattern was synthesized and made more hydrophilic by plasma oxidizing the stamp allowing the PDMS surface to absorb polylysine. Further studies expanding the method showed many different kinds of proteins could be transferred onto a variety of different surfaces using the master pattern including glass, polystyrene, and silicon.[32] Later, transfer efficiency studies were performed on a variety of different SAMs to see how functionality affected how much protein was transferred to the substrate. While more hydrophobic moieties tend to mediate protein absorption better, it was actually found that increasing the hydrophilicity of the substrate increased the amount of protein that was transferred from the master pattern to the substrate. The protein transfer efficiency was found to improve even more by increasing the hydrophobicity of the master pattern.[33]

Another route towards increasing the efficiency of protein transfer is changing the type of interaction between the protein and the substrate. Instead of using polar and nonpolar interactions, the hydrophobic interactions between biotin and aromatic amino acids inside the avidin binding pockets, the strongest noncovalent bond in

nature, could be used to pattern proteins. Techniques have been developed in order to print both avidin patterns and biotin patterns.[34,35] Moving beyond proteins, the biotin-avidin route has also been used to pattern cells by first patterning biotinylated RGD onto a substrate, which recognizes integrins sitting on the cell surface. The integrins are then bound by the RGD, and causes the cells to adhere to the patterned substrate.[35] Although the transfer efficiency increases, there is an extra synthesis step which increases the cost and the biotinylation reaction also results in loss of function for some proteins.[36,37]

1.3 Patterning surface chemistry with scanning probe microscopy-based methods

Direct writing methods have been developed over time as another pathway to patterned surface chemistry. This first started with the invention of the scanning tunneling microscope (STM) followed by other instruments such as the atomic force microscope (AFM).[38–40] While STM first allowed for patterns to be created moving one molecule at a time with serial STM under ultrahigh vacuum and low temperatures,[41] most direct writing based patterned surface chemistry techniques have moved toward AFM based methods or dip-pen nanolithography (DPN).[42]

The Mirkin group introduced DPN in 1999 where an AFM tip is dipped into a solution or "ink" of the desired chemical reagents and directly draws nanopatterned chemistries onto a solid substrate (Figure 1.2).[43]

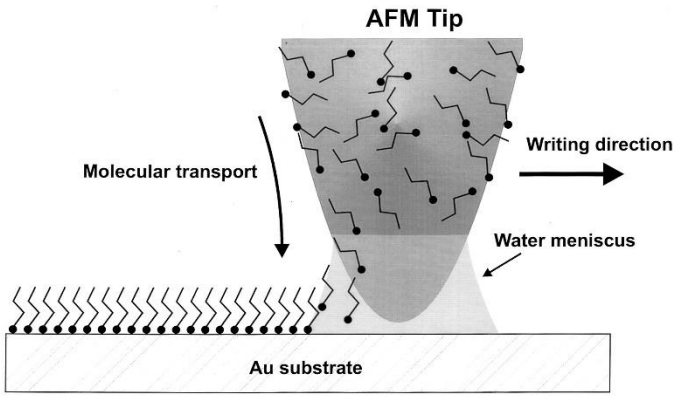

Figure 1.2: Schematic representation of DPN. A water meniscus forms between the AFM tip coated with 1-octadecanethiol and the Au substrate. The size of the meniscus, which is controlled by relative humidity, affects the 1-octadecanethiol transport rate, the effective tip-substrate contact area, and DPN resolution.[43]

The first studies demonstrated that various alkanethiols, including 1-octadecanethiol and 16-mercaptohexadecanoic acid with potential etch resist applications for metal and semiconductor nanostructures, could be patterned onto gold surfaces with sub-100-nm alignment.[43–46] Since then DPN has been able to chemically pattern many different types of molecules using the same basic principles including small organic molecules[47–50] and polymers.[51–56]

While DPN started off in the realm of microelectronics, there is an increasing amount of interest and literature in biomolecular arrays for DNA, small molecule, and protein detection.[57] While cross contamination is generally eliminated with DPN methods, because of issues with cross-reactivity and nonspecific binding of analytes or other species to array spots, it was necessary to start developing new patterning techniques within the DPN realm for certain biomolecules. To start realizing DPN patterns for screening, indirect adsorption techniques were developed to create protein and oligonucleotide arrays. These techniques involve first creating a DPN pattern, one of the first examples uses 16-mercaptohexadecanoic acid as described earlier, known to attract a certain protein, in this case IgG protein. The DPN patterned surface is then passivated followed by dipping the patterned surface into a solution of protein

allowing for protein adsorption onto the DPN patterned surface. Once the protein is adsorbed onto the pattern by either electrostatic interactions or covalent coupling it can be used to recognize specific antibodies.[58,59] It has also been shown that it is possible to produce biomolecular arrays with spots of many different types using parallel-pen and integrated-inking systems.[60–63]

Since then, proteins have also been directly patterned using tapping-mode AFM by depositing thiolated collagen and peptides onto gold surfaces. The patterned collagen assembled into helical structures with a 65 nm periodicity, indicating that the DPN process did not damage the collagen.[54] Antibodies can also be directly written into nanoscale patterns such as human chorionic gonadotropin antibody onto 3-glycidoxypropyltrimethoxysilane-modified glass surfaces but it was unclear if the antibody's biological activity remained after it had been patterned.[53] Since these first initial studies, many groups have worked toward preserving the biological activity of various proteins by having more precise control of the AFM tip surface, humidity, and temperature.[58,64] DPN based techniques have also patterned DNA on both conducting and insulating surfaces, but once again it was critical to have precise control of the AFM tip surface and humidity while writing.[55] To pattern onto gold surfaces, hexanethiol-modified oligonucleotides were used, while acrylamide modified oligonucleotides were used to create patterned surfaces onto 3'-mercaptopropyltrimethoxysilane modified silicon wafers.[55]

While one can create a wide variety of chemical patterns with potentially higher resolution and registration than the microcontact printing methods described in section 1.2 using direct writing methods, the amount of time it takes to create the pattern is dependent on the size of the pattern. Unlike microcontact printing, the size dependent time makes DPN difficult to scale up efficiently. One potential solution which would provide the high resolution and registration of chemical patterns but does

not increase the patterning time when scaled up is block copolymer self-assembly.

1.4 Patterning surface chemistry with block copolymers

A block copolymer (BCP) is made up of two or more polymer chains that are chemically different, and each different polymer chain is a "block", which are covalently bonded to one another. When mobilized, BCPs are driven to microphase segregate or self-assemble into various ordered structures on the order of 10s of nms, determined by the relative volume fractions of each block, the molar mass or size of the BCP, and the interaction between each of the different blocks. The ordered structures can be plotted into a BCP phase diagram as seen in Figure 1.3.

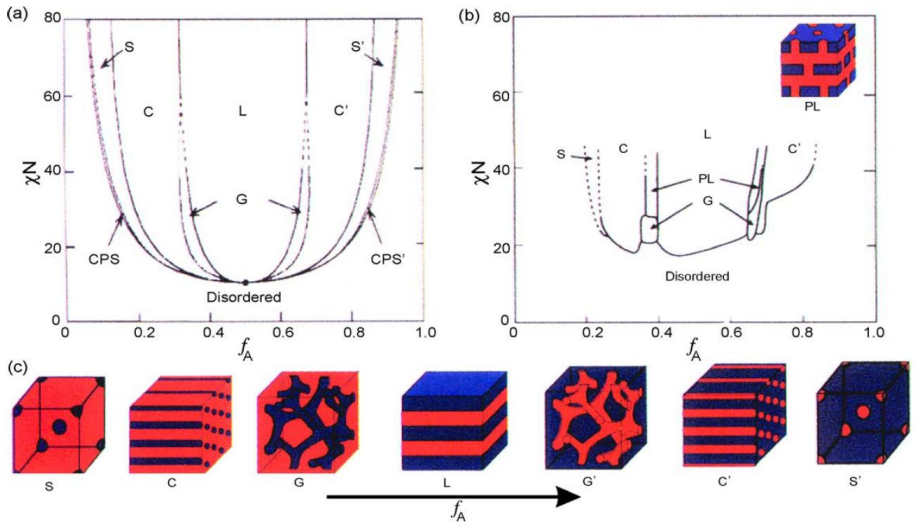

Figure 1.3: Diblock copolymers are predicted to self-assemble according to a phase diagram predicted by self-consistent mean field theory (a) and proven experimentally (b). A variety of constant-radius geometries are observed as a function of relative lengths of the two blocks (c).[65]

These structures are thermodynamically a result of the competition between enthalpy driving the microphase segregation and configurational entropy driving the individual blocks to be coiled rather than stretched.[65]

When moving to thin films, the microphase segregated structure formation is

heavily influenced by the interfaces of the film with substrate and air. These structures tend to assemble in a certain orientation relative to the substrate surface. The orientation can be controlled by both the chemistry of the surface as well as the mobilizing solvent incorporated through spin coating and solvent annealing the BCP thin film (Figure 1.4).[66]

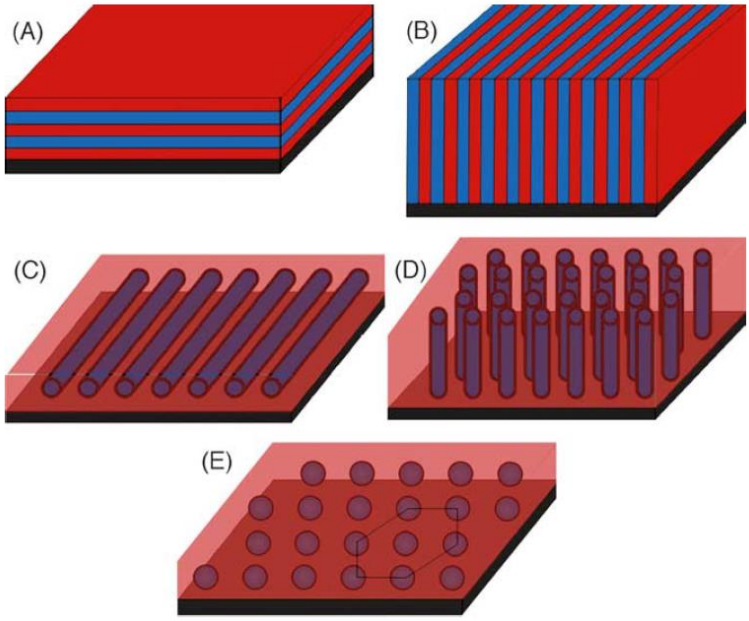

Figure 1.4: When confined to a thin film, the orientation of block copolymer domains with respect to the substrate surface is crucial for many applications. (A) Lamellae lying parallel to the substrate, (B) lamellae aligned perpendicular, (C) cylinders lying parallel, (D) cylinders perpendicular, and (E) spheres. In the case of lamellae in the perpendicular orientation and cylinders in parallel, lines can be patterned if the persistence length of the structure can be controlled. In the case of upright cylinders and spheres, the grain size and perfection of the hexagonal array is of primary importance.[66]

In this thesis, the hexagonally packed cylinder morphology is explored. The orientation of the cylinders, standing up perpendicular to the substrate versus laying down parallel to the substrate, is controlled by the solvent used for BCP assembly but can also be controlled by the hydrophilic versus hydrophobic surface chemistry of the

substrate.

While there have been many groups that have synthesized and assembled a vast number of functional BCPs into a variety of different chemical patterns,[67–88] there is far less literature where one BCP can be post-functionalized with an array of different functionalities while still retaining its thermodynamically favored BCP structure. A step towards this was synthesizing BCPs that had at least one block that could be post-functionalized with different functional groups utilizing various "click" chemistries. "Click" chemistry refers to reactions that are modular, wide in scope, high yielding, stereospecific, create only byproducts that can be removed by non-chromatographic methods, be conducted in easily removable or benign solvents, and the product must be stable in physiological conditions.[89] Some examples include copper (I) catalyzed and strain-promoted azide-alkyne cycloadditions, Diels-Alder cycloadditions, and UV photoinitiated thiol-ene reactions. This thesis focuses on thiol-ene "click" chemistry, which is further discussed in Chapter 2. Many different BCPs have been synthesized where one or more blocks are post-functionalized using one of the "click" chemistries listed above with side groups such as pentafluorostyrenes, alkenes, carboxylates, amines, and azlactones. Usually the post-functionalization step occurs before BCP self-assembly, leading to the loss of thermodynamically favored BCP structures, metastable BCP structures, or continuously changing assembly conditions, which are usually undesirable.[90–96]

To keep the same BCP assembly conditions while still being able to change the functionality of the BCP, it is necessary to first assemble the BCP and then post-functionalize the assembled BCP. One of the first groups to do this synthesized a poly(styrene)-*b*-poly(2-vinyl-4,4-dimethylazlactone) BCP which assembled into lamellar BCP thin films.[97] The azlactone functionality was selected because it readily reacts through ring-opening reactions with a broad range of nucleophiles and primary

amines, and is stable under typical BCP assembly conditions.[98,99] Once assembled, the BCP was functionalized with a red dye containing a primary amine and then characterized with fluorescence and contact angle measurements. While it was demonstrated that it was possible to first assemble and then post-functionalize a BCP throughout the thin film, it did not visualize the localization of the post-functionalization, provide chemical characterization indicating the functional groups were covalently attached, or show a potential route to control the number of functional groups attached to the desired block. Chapter 2 of this thesis explores a new surface functionalization BCP thin film synthesis method and answers questions such as how can we gain insights into how and where the functional groups are attached? It also provides a future route to control the number of functional groups attached to the desired block. Now that the main three methods to pattern surface chemistry have been described, it is time to discuss how these different patterned surface chemistry methods are used to template the growth of inorganics starting with microcontact printing.

1.5 Templating the growth of inorganics with microcontact printing

As described in Section 1.2, microcontact printing typically works by transferring material directly to the substrate using a patterned stamp (see Section 1.2 for more details). While most inorganic patterns created using microcontact printing are implemented by printing monolayer resists on metallic films and etching the unprinted regions or by printing seeding solutions or catalysts for electroless deposition from solution,[4,100–104,3,105] this section will only focus on how microcontact printing patterns are used to template the nucleation and growth of inorganics. To template the nucleation and growth of inorganics, first a chemical pattern must be created where one section prefers the inorganic crystal to nucleate while the other

section does not induce nucleation and growth of the inorganic. In 1999, SAMs were patterned on metal substrates, silver, gold, or palladium, with polar acid functional groups as the nucleating region separated by methyl groups as the non-nucleating region via microcontact printing. The patterned surface was submerged in a calcium chloride solution and then exposed to carbon dioxide to template the nucleation and growth of calcite, a polymorph of calcium carbonate.[106]

It was proposed that mass transport helped to template the nucleation of calcite on the polar regions and prevent nucleation on the methyl regions. SAMs functionalized with polar groups nucleate inorganic materials, specifically calcite, faster than SAMs functionalized with methyl groups. Once crystal nucleation and growth starts in the polar region, calcium and carbonate ions move to the growing crystals through mass transport decreasing the local concentration of those ions over the methyl regions to the point of undersaturation inhibiting nucleation in the methyl regions.[107] On top of controlling where the crystal nucleates, the number of crystals formed per active site could also be controlled by varying the area and distribution of functional groups in the patterned polar regions. The specific polar functional group, carboxylic acid, sulfonic acid, or hydroxyl, that was patterned also controlled the crystallographic orientation of the final calcite crystal. It was found that there was a relationship between the SAMs' structure and crystal plane they nucleate. Therefore, the facet-selective nucleation is thought to originate from a match between the functionalized SAMs pattern and orientation of ions adsorbed on the organic surface and those in the nucleating crystal plane.[108–110] This method was the first to achieve both patterned area-selective nucleation and specific growth of crystals in a single crystallographic direction.[106] Since then, other functionalities have been introduced to study how they interact with different facets of calcite,[111] and the method has been expanded up to create 3D templates of crystalline calcite.[112] While these works

carefully studied and proposed a mechanism for controlling the nucleating plane of calcite, Chapter 4 will introduce a potential new mechanism for controlling the orientation and texturing of the nucleating crystal plane of transition metal oxides. It is also interesting to note that a related approach was able to pattern and template the nucleation and growth of several different organic semiconductor crystals,[113] although it is outside the scope of this introduction.

One of the only other studies, to the best of my knowledge, that uses microcontact printed surfaces to template the nucleation and growth of inorganics other than calcite was performed in 2007 to grow zinc oxide (ZnO) nanostructured arrays.[114] First, a hydrophilic PDMS stamp was used for microcontact printing of an aqueous zinc acetate dihydrate ink onto a substrate, either glass, plastic, or silicon which then was annealed in a furnace. Once annealed, ZnO nanowires were grown using an aqueous zinc acetate dihydrate with no organic additives at 85-90°C, washed with distilled water, and then dried at 100°C. It was found that the concentration of zinc acetate dihydrate helped control the dimensions of the ZnO nanostructures grown on the substrates. At low concentrations (1 mM), individual long, thin ZnO nanowires were grown with an average diameter of 20 nm and a length of 2 μm. When the concentration increased to 0.1 M, monodisperse 250 nm in diameter, hexagonal ZnO crystals formed. It is also interesting to note that at intermediate concentrations (greater than or equal to 5 mM), the ZnO nanowires were mostly aligned, rather than randomly oriented which was seen at both high and low concentrations. Chapters 3 and 4 of this thesis will template the growth of various crystalline inorganics, including ZnO, on a smaller length scale at lower temperatures (below 60°C) and control the crystal orientation and texturing of the final templated inorganic.

1.5 Templating the nucleation of inorganics with scanning probe microscopy-based methods

As described in section 1.3, scanning probe microscopy-based methods are direct writing techniques that draw out the desired chemical pattern. While there are many methods to create nanostructured inorganic materials,[42,115–117] it is rare that a patterned surface templates the nucleation and growth of the respective inorganic. Typically colloids or nanoparticles are first synthesized and then directly drawn onto a substrate in the desired pattern,[118–126,48,127–129] patterned onto a surface, or the nanoparticles are functionalized with a target ligand that selectively attaches to the DPN patterned surface chemistry.[48,129] In both of these cases the actual nucleation of the respective inorganic is not templated and therefore these cases are outside the realm of this introduction.

The first step towards templating the nucleation and growth of inorganics with DPN patterned surface chemistry was a method developed in 2010 that allowed for nanoparticles encapsulated in a polymer to be deposited into a pattern on a substrate.[130] The polymer, here poly(ethylene glycol), was primarily used because it is soluble in a broad range of solvents, chemically inert, and easily transported by DPN. While the technique allowed for nanopatterned gold, iron oxide, and buckminsterfullerene encapsulated in poly(ethylene glycol) on various substrates, it did not template the nucleation of the respective inorganic but set the foundation for future related techniques to template the nucleation of inorganics.

To move onto templating the nucleation and growth of an inorganic material, a block copolymer based method was developed.[131] Poly(ethylene oxide)-*b*-poly(2-vinylpyridine) (PEO-*b*-P2VP) was selected because polyethylene has been previously shown to be easily transported through DPN, while poly(2-vinylpyridine) coordinates metal ions that can go on to produce a single nanoparticle in each block copolymer

feature. As a proof of principle study, cadmium was selected to coordinate with the P2VP for patterning and then once patterned onto a substrate, was exposed to hydrogen sulfide to form crystalline cadmium sulfide at high pressures (850-1000 Torr). The size of the resulting cadmium sulfide crystals was determined by the tip's contact time with the substrate and block copolymer feature size.

Now that a DPN patterned surface had been demonstrated to template the nucleation of cadmium sulfide, the next step was to expand the method to a variety of different metal and metal oxides and gain further insights into how the crystalline inorganic forms within the pattern. Previously, when metal patterns were created using printed block copolymers, oxygen plasma was used to reduce the embedded metal ions.[132] Two important steps were investigated, precursor phase separation and nanoparticle formation. To separate out these two steps and to determine whether or not it is required for metal ions within the polymer to aggregate before metal ion reduction and particle nucleation, oxygen plasma treatment was replaced with two annealing steps. The first annealing step was at a lower temperature (150°C) to initiate phase separation, while the second annealing step was at a higher temperature (500°C) to reduce the metal ion, form the particle, and decompose the polymer. As described earlier, first the respective metal precursors were mixed with an aqueous solution of PEO-*b*-P2VP, transferred onto a DPN tip, and then patterned onto a substrate. Once patterned, the metal ions are evenly distributed throughout the block copolymer. After the DPN process, the patterned ions were heated at the lower temperature to aggregate the precursors, concentrating them into one region. Once the precursors aggregated, the second annealing step was applied and the respective metal or metal oxide was reduced into a single nanoparticle. It has been demonstrated that the nucleation and growth of crystalline Au, Ag, Pt, Pd, Fe_2O_3, Co_2O_3, NiO, CuO, and alloys of Au and Ag can be templated using the above DPN patterning and annealing

method.[133] While numerous inorganics have been templated, it is difficult to scale up direct writing methods, requires high temperatures to template the nucleation and growth of crystalline inorganics, and does not control the orientation or texturing of the final inorganic crystal. In Chapter 3 and 4 of this thesis, I describe a method to control the nucleation and growth of various transition metal oxides at low temperatures (below 60°C).

1.6 Templating the growth of inorganics with block copolymers

BCPs, described in Section 1.4, have been used extensively in the past to chemically pattern surfaces, but once again have been rarely used in thin films to template the nucleation and growth of crystalline inorganics. Most times small nanoparticles are synthesized with functional groups that are compatible with one of the blocks in the BCP, then mixed with the respective BCP, assembled, and heat treated to create nanostructured inorganics.[134–149] Although these techniques have been applied to a wide variety of inorganics, they do not template the nucleation and growth of the respective inorganic, therefore are outside of the scope of this introduction. In addition, it has been a challenge to achieve highly crystalline nanostructured inorganic materials through these routes directly, without applying trips to control crystal overgrowth and nanostructure collapse.

The first work that templated the nucleation and growth of an inorganic with a BCP patterned surface was done in 2009.[150] Poly(styrene)-block-poly(acrylic acid) (PS-b-PAA) was selected as the BCP template because the interfacial energy difference between the hydrophobic PS domain and the hydrophilic PAA domain caused preferential heterogeneous nucleation and growth of inorganic material on the PAA domains. Once the BCP was assembled in standing up hexagonally packed PAA

cylinders, it was exposed to various metal chloride salts, Cd, Zn, or Pb, and then sulfurized to form the respective metal sulfide. CdS, ZnS, and PbS were selected because of their small critical nucleation size, which is smaller than the PAA domain size and therefore could be confined within that domain. It is thought that the carboxylic acid groups at the surface of the PAA domains interact with the metal ions leading to metal ion concentrated regions on the PAA domain, which cause preferential heterogenous nucleation on the PAA surfaces rather than the hydrophobic PS surfaces. In addition, the authors hypothesize that the topography of the PS and PAA domains also play a role in confining the nucleation to only the PAA domain. Compared to a flat PAA surface, the depressed surface topography could have an even higher density of surface carboxylic acid groups to metal ions which diffuse into the PAA domain, but they were unable to demonstrate their hypothesis experimentally due to surface energy restrictions of the BCP template.

One of the only other studies that used a BCP template to template the nucleation and growth of an inorganic was performed in 2016.[151] Poly(styrene)-block-Poly(2-vinylpyridine) (PS-b-P2VP) was assembled into laying down hexagonal cylinders, and then exposed to a selective seeding solution of molybdenum precursors, ammonium tetrathiomolybdate or ammonium heptamolybdate at 90°C. The inorganic precursors selectively infiltrate the P2VP domains because of the amine group, creating a local concentration of molybdenum ions. Once loaded with metal ions, the BCP template was annealed and sulfurized to nucleate and grow molybdenum sulfide. The annealing temperature could be tuned to produce either amorphous (340°C – 480°C) or polycrystalline molybdenum sulfide nanowires (515°C – 700°C). Although these methods were able to template the nucleation and growth of inorganic metal sulfides, they required high temperature processing, were unable to control the final inorganic crystal texturing and orientation, and did not expand to templating transition

metal oxides. Chapter 3 of this thesis expands the number of inorganics that can be templated with BCP surfaces by introducing a new method to template the nucleation and growth of various transition metal oxides using a post-assembly functionalized BCP template. Chapter 4 expands upon these ideas further by demonstrating control over the texturing and orientation of the templated transition metal oxide and proposes a mechanism of how the confined oxide nucleates and grows on different functional groups leading to the final crystal texturing and orientation.

1.7 Summary and Outlook

Developing and gaining understanding of the molecular interactions at the interface between nanostructured organic and inorganic materials is imperative to foraging fundamental knowledge for controlling the crystallization of inorganics within nanostructured organic templates. Applications that depend on understanding these interfaces include energy storage and conversion devices.[152] While there have been many techniques developed over the years to pattern surface chemistry for inorganic templating, most methods are at a micron length scale and do not control the final texturing and orientation of the inorganic crystal. Continued research is needed to elucidate key fundamental materials questions such as: how do we control the final crystal and orientation of the inorganic using an organic template, how does the functional group determine the final crystal, what happens when we change the concentration of confined functional groups, how large of a molecule can we confine and can larger molecules provide even further control over the final inorganic formation? To be able to utilize chemical functionalities control over inorganic nucleation and growth, continued efforts in fundamental materials interface research is required.

1.8 Outline of the dissertation

In this dissertation, I develop a versatile method to template the nucleation and growth of two nanostructured transition metal oxides at low temperatures and at standard pressures on the 10s of nm length scale. First, I describe a reactive BCP thin film template for localized confined surface reactions. Then, to study the control of crystalline inorganic texturing and orientation, I systematically alter the BCP thin film by changing the confined chemical group to understand the function of the organic on the final transition metal oxide crystal. I also probe the initial nucleation site to better understand the inorganic's subsequent growth and propose a mechanism for controlling the texture and orientation of the final oxide.

The first part of this dissertation (Chapter 2) focuses on the development of a reactive block copolymer film for confined surface reactions; specifically looking at the chemical and visual localization of the respective functional group or nanoparticle. Chapter 3 uses the chemistry developed in Chapter 2 to introduce a low temperature and standard pressure route to templating the nucleation and growth of transition metal oxides on the 10s of nm length scale. The last part describes the systematic attachment of different functional groups, to study how different functional groups affect the template surface, initial inorganic nucleation, final texturing and orientation of the inorganic crystal. Finally, a mechanism is proposed for how the inorganic nucleates and grows within the functionalized domain of the BCP (Chapter 4).

1.9 References

(1) Kumar, A.; Whitesides, G. M. Features of Gold Having Micrometer to Centimeter Dimensions Can Be Formed through a Combination of Stamping with an Elastomeric Stamp and an Alkanethiol "ink" followed by Chemical Etching. *Appl. Phys. Lett.* **1993**, *63* (14), 2002–2004.

(2) Li, H. W.; Muir, B. V. O.; Fichet, G.; Huck, W. T. S. Nanocontact Printing: A Route to Sub-50-Nm-Scale Chemical and Biological Patterning. *Langmuir* **2003**, *19* (6), 1963–1965.

(3) Quist, A. P.; Pavlovic, E.; Oscarsson, S. Recent Advances in Microcontact Printing. *Anal. Bioanal. Chem.* **2005**, *381* (3), 591–600.

(4) Alom Ruiz, S.; Chen, C. S. Microcontact Printing: A Tool to Pattern. *Soft Matter* **2007**, *3* (2), 168–177.

(5) Kaufmann, T.; Ravoo, B. J. Stamps, Inks and Substrates: Polymers in Microcontact Printing. *Polym. Chem.* **2010**, *1* (4), 371.

(6) Ghosh, P.; Lackowski, W. M.; Crooks, R. M. Two New Approaches for Patterning Polymer Films Using Templates Prepared by Microcontact Printing. *Macromolecules* **2001**, *34* (5), 1230–1236.

(7) Arrington, D.; Curry, M.; Street, S. C. Patterned Thin Films of Polyamidoamine Dendrimers Formed Using Microcontact Printing. *Langmuir* **2002**, *18* (21), 7788–7791.

(8) Jeon, N. L.; Choi, I. S.; Whitesides, G. M.; Kim, N. Y.; Laibinis, P. E.; Harada, Y.; Finnie, K. R.; Girolami, G. S.; Nuzzo, R. G. Patterned Polymer Growth on Silicon Surfaces Using Microcontact Printing and Surface-Initiated Polymerization. *Appl. Phys. Lett.* **1999**, *75* (26), 4201–4203.

(9) Shah, R. R.; Merreceyes, D.; Husemann, M.; Rees, I.; Abbott, N. L.; Hawker, C. J.; Hedrick, J. L. Using Atom Transfer Radical Polymerization to Amplify

Monolayers of Initiators Patterned by Microcontact Printing into Polymer Brushes for Pattern Transfer. *Macromolecules* **2000**, *33* (2), 597–605.

(10) Marikkar, F. S.; Carter, C.; Kieltyka, K.; Robertson, J. W. F.; Williamson, C.; Simmonds, A.; Zangmeister, R.; Fritz, T.; Armstrong, N. R. Conducting Polymer Diffraction Gratings on Gold Surfaces Created by Microcontact Printing and Electropolymerization at Submicron Length Scales. *Langmuir* **2007**, *23* (20), 10395–10402.

(11) Jiang, X.; Hammond, P. T. Selective Deposition in Layer-by-Layer Assembly: Functional Graft Copolymers as Molecular Templates. *Langmuir* **2000**, *16* (22), 8501–8509.

(12) Park, J.; Kim, Y. S.; Hammond, P. T. Chemically Nanopatterned Surfaces Using Polyelectrolytes and Ultraviolet-Cured Hard Molds. *Nano Lett.* **2005**, *5* (7), 1347–1350.

(13) Jiang, X.; Zheng, H.; Gourdin, S.; Hammond, P. T. Polymer-on-Polymer Stamping: Universal Approaches to Chemically Patterned Surfaces. *Langmuir* **2002**, *18* (7), 2607–2615.

(14) Chen, L.; Degenaar, P.; Bradley, D. D. C. Polymer Transfer Printing: Application to Layer Coating, Pattern Definition, and Diode Dark Current Blocking. *Adv. Mater.* **2008**, *20* (9), 1679–1683.

(15) Zhai, L.; Laird, D. W.; McCullough, R. D. Soft-Lithography Patterning of Functionalized Regioregular Polythiophenes. *Langmuir* **2003**, *19* (16), 6492–6497.

(16) Li, D.; Guo, L. J. Micron-Scale Organic Thin Film Transistors with Conducting Polymer Electrodes Patterned by Polymer Inking and Stamping. *Appl. Phys. Lett.* **2006**, *88* (6), 2004–2007.

(17) Granlund, T.; Nyberg, T.; Roman, L. S.; Svensson, M.; Inganas, O. Patterning

of Polymer Light-Emitting Diodes with Soft Lithography. *Adv. Mater.* **2000**, *12* (4), 269–273.

(18) Chang, J. C.; Brewer, G. J.; Wheeler, B. C. A Modified Microstamping Technique Enhances Polylysine Transfer and Neuronal Cell Patterning. *Biomaterials* **2003**, *24* (17), 2863–2870.

(19) Csucs, G.; Michel, R.; Lussi, J. W.; Textor, M.; Danuser, G. Microcontact Printing of Novel Co-Polymers in Combination with Proteins for Cell-Biological Applications. *Biomaterials* **2003**, *24* (10), 1713–1720.

(20) Kim, P.; Lee, S. E.; Jung, H. S.; Lee, H. Y.; Kawai, T.; Suh, K. Y. Soft Lithographic Patterning of Supported Lipid Bilayers onto a Surface and inside Microfluidic Channels. *Lab Chip* **2006**, *6* (1), 54–59.

(21) Na, K.; Jung, J.; Shin, B.; Hyun, J. Micropatterning of Cell-Repellent Polymer on a Glass Substrate for the Highly Resolved Virus Microarray. *Langmuir* **2006**, *22* (26), 10889–10892.

(22) Kidambi, S.; Lee, I.; Chan, C. Controlling Primary Hepatocyte Adhesion and Spreading on Protein-Free Polyelectrolyte Multilayer Films. *J. Am. Chem. Soc.* **2004**, *126* (50), 16286–16287.

(23) Barrett, E. W.; Phelps, M. V. B.; Silva, R. J.; Gaumond, R. P.; Allcock, H. R. Patterning Poly(organophosphazenes) for Selective Cell Adhesion Applications. *Biomacromolecules* **2005**, *6* (3), 1689–1697.

(24) Kidambi, S.; Sheng, L.; Yarmush, M. L.; Toner, M.; Lee, I.; Chan, C. Patterned Co-Culture of Primary Hepatocytes and Fibroblasts Using Polyelectrolyte Multilayer Templates. *Macromol. Biosci.* **2007**, *7* (3), 344–353.

(25) Bjork, P.; Holmstrom, S.; Inganas, O. Soft Lithographic Printing of Patterns of Stretched DNA and DNA/electronic Polymer Wires by Surface-Energy Modification and Transfer. *Small* **2006**, *2* (8–9), 1068–1074.

(26) Singhvi, R.; Kumar, A.; Lopez, G. P.; Stephanopoulos, G. N.; Wang, D. I.; Whitesides, G. M.; Ingber, D. E. Engineering Cell Shape and Function. *Science* **1994**, *264* (5159), 696–698.

(27) Mrksich, M.; Whitesides, G. M. Patterning Self-Assembled Monolayers Using Microcontact Printing: A New Technology for Biosensors? *Trends Biotechnol.* **1995**, *13* (6), 228–235.

(28) Gross, G. W.; Rhoades, B. K.; Azzazy, H. M. E.; Ming-Chi Wu. The Use of Neuronal Networks on Multielectrode Arrays as Biosensors. *Biosens. Bioelectron.* **1995**, *10* (6–7), 553–567.

(29) Chen, C. S.; Mrksich, M.; Huang, S.; Whitesides, G. M.; Ingber, D. E. Geometric Control of Cell Life and Death. *Technology* **1997**, *276* (May), 1425–1428.

(30) Bhatia, S. N.; Balis, U. J.; Yarmush, M. L.; Toner, M. Effect of Cell–cell Interactions in Preservation of Cellular Phenotype: Cocultivation of Hepatocytes and Nonparenchymal Cells. *FASEB J.* **1999**, *13* (14), 1883–1900.

(31) James, C. D.; Davis, R. C.; Kam, L.; Craighead, H. G.; Isaacson, M.; Turner, J. N.; Shain, W. Patterned Protein Layers on Solid Substrates by Thin Stamp Microcontact Printing. *Langmuir* **1998**, *14* (4), 741–744.

(32) Bernard, A.; Delamarche, E.; Schmid, H.; Michel, B.; Bosshard, H. R.; Biebuyck, H. Printing Patterns of Proteins. *Langmuir* **1998**, *14* (9), 2225–2229.

(33) Tan, J. L.; Tien, J.; Chen, C. S. Microcontact Printing of Proteins on Mixed Self-Assembled Monolayers Microcontact Printing of Proteins on Mixed Self-Assembled Monolayers. *Society* **2002**, *18* (2), 519–523.

(34) Patel, N.; Bhandari, R.; Shakesheff, K. M.; Roberts, C. J.; Tendler, S. J. B.; Williams, P. M. Printing Patterns of Biospecifically-Adsorbed Protein. *J. Biomater. Sci., Polym. Ed.* **2000**, *11* (3), 319–331.

(35) Yang, Z. P.; Chilkoti, A. Microstamping of a Biological Ligand onto an Activated Polymer Surface. *Adv. Mater.* **2000**, *12* (6), 413.

(36) Biasco, A.; Pisignano, D.; Krebs, B.; Pompa, P. P.; Persano, L.; Cingolani, R.; Rinaldi, R. Conformation of Microcontact-Printed Proteins by Atomic Force Microscopy Molecular Sizing. *Langmuir* **2005**, *21* (11), 5154–5158.

(37) Hyun, J.; Zhu, Y.; Liebmann-Vinson, A.; Beebe, T. P.; Chilkoti, A. Microstamping on an Activated Polymer Surface: Patterning Biotin and Streptavidin onto Common Polymeric Biomaterials. *Langmuir* **2001**, *17* (20), 6358–6367.

(38) Binnig, G.; Rohrer, H.; Gerber, C.; Weibel, E. Tunneling through a Controllable Vacuum Gap. *Appl. Phys. Lett.* **1982**, *40* (September 1981), 178–180.

(39) Binnig, G.; Rohrer, H.; Gerber, C.; Weibel, E. Surface Studies by Scanning Tunneling Microscopy. *Phys. Rev. Lett.* **1982**, *49* (1), 57–61.

(40) Binnig, G.; Quate, C. F.; Gerber, C. Atomic Force Microscope. *Phys. Rev. Lett.* **1986**, *56* (9), 930–933.

(41) Schweizer, D. K.; Eigler, E. K. Positioning Single Atoms with a Scanning Tunneling Microscop. *Nature*. 1990, pp 524–525.

(42) Ginger, D. S.; Zhang, H.; Mirkin, C. A. The Evolution of Dip-Pen Nanolithography. *Angew. Chemie - Int. Ed.* **2004**, *43* (1), 30–45.

(43) Piner, R. D.; Zhu, J.; Xu, F.; Hong, S. "Dip-Pen" Nanolithography. *Science (80-.).* **1999**, *283* (5402), 661–663.

(44) Hong, S. Multiple Ink Nanolithography: Toward a Multiple-Pen Nano-Plotter. *Science (80-.).* **1999**, *286* (5439), 523–525.

(45) Hong, S. A Nanoplotter with Both Parallel and Serial Writing Capabilities. *Science (80-.).* **2000**, *288* (5472), 1808–1811.

(46) Dana A. Weinberger; Hong, S.; Mirkin, C. A.; Wessels, B. W.; Higgins, T. B.

Combinatorial Generation and Analysis ofNanometer- and Micrometer-Scale SiliconFeatures via [a]Dip-Pen[o] Nanolithography and WetChemical Etching. *Adv. Mater.* **2000**, *12* (21), 1600.

(47) Jung, H.; Kulkarni, R.; Collier, C. P. Dip-Pen Nanolithography of Reactive Alkoxysilanes on Glass. *J. Am. Chem. Soc.* **2003**, *125* (40), 12096–12097.

(48) Liu, X.; Fu, L.; Hong, S.; Dravid, V. P.; Mirkin, C. A. Arrays of Magnetic Nanoparticles Patterned Via "dip-Pen" nanolithography. *Adv. Mater.* **2002**, *14* (3), 231–234.

(49) Pena, D. J.; Raphael, M. P.; Byers, J. M. "Dip-Pen" Nanolithography in Registry with Photolithography for Biosensor Development. *Langmuir* **2003**, *19* (21), 9028–9032.

(50) Ivanisevic, A.; McCumber, K. V.; Mirkin, C. A. Site-Directed Exchange Studies with Combinatorial Libraries of Nanostructures. *J. Am. Chem. Soc.* **2002**, *124* (40), 11997–12001.

(51) Maynor, B. W.; Filocamo, S. F.; Grinstaff, M. W.; Liu, J. Direct-Writing of Polymer Nanostructures: Poly(thiophene) Nanowires on Semiconducting and Insulating Surfaces. *J. Am. Chem. Soc.* **2002**, *124* (4), 522–523.

(52) Lim, J. H.; Mirkin, C. A. Electrostatically Driven Dip-Pen Nanolithography of Conducting Polymers. *Adv. Mater.* **2002**, *14* (20), 1474–1477.

(53) Noy, A.; Miller, A. E.; Klare, J. E.; Weeks, B. L.; Woods, B. W.; DeYoreo, J. J. Fabrication of Luminescent Nanostructures and Polymer Nanowires Using Dip-Pen Nanolithography. *Nano Lett.* **2002**, *2* (2), 109–112.

(54) Wilson, D. L.; Martin, R.; Hong, S.; Cronin-Golomb, M.; Mirkin, C. A.; Kaplan, D. L. DPN105-Surface Organization and Nanopatterning of Collagen by Dip-Pen Nanolithography. *Proc. Natl. Acad. Sci. U. S. A.* **2001**, *98* (24), 13660–13664.

(55) Demers, L. M. Direct Patterning of Modified Oligonucleotides on Metals and Insulators by Dip-Pen Nanolithography. *Science (80-.).* **2002**, *296* (5574), 1836–1838.

(56) Liu, X.; Guo, S.; Mirkin, C. A. Surface and Site-Specific Ring-Opening Metathesis Polymerization Initiated by Dip-Pen Nanolithography. *Angew. Chemie - Int. Ed.* **2003**, *42* (39), 4785–4789.

(57) Schulze, a; Downward, J. Navigating Gene Expression Using Microarrays--a Technology Review. *Nat. Cell Biol.* **2001**, *3* (8), E190–E195.

(58) Lee, K. B.; Lim, J. H.; Mirkin, C. A. Protein Nanoarrays Generated By Dip-Pen Nanolithography. *Science (80-.).* **2002**, *295* (5560), 1702–1705.

(59) Hyun, J.; Ahn, S. J.; Lee, W. K.; Chilkoti, A.; Zauscher, S. Molecular Recognition-Mediated Fabrication of Protein Nanostructures by Dip-Pen Lithography. *Nano Lett.* **2002**, *2* (11), 1203–1207.

(60) Binnig, G. K. The " Millipede "— More than One Thousand Tips for Future AFM Data Storage We Report on a New Atomic Force Microscope. *IBM J. Res. Dev.* **2000**, *44* (3), 323–340.

(61) Sulchek, T.; Grow, R. J.; Yaralioglu, G. G.; Minne, S. C.; Quate, C. F.; Manalis, S. R.; Kiraz, A.; Aydine, A.; Atalar, A. Parallel Atomic Force Microscopy with Optical Interferometric Detection. *Appl. Phys. Lett.* **2001**, *78* (12), 1787–1789.

(62) King, W. P.; Kenny, T. W.; Goodson, K. E.; Cross, G. L. W.; Despont, M.; Dürig, U. T.; Rothuizen, H.; Binnig, G.; Vettiger, P. Design of Atomic Force Microscope Cantilevers for Combined Thermomechanical Writing and Thermal Reading in Array Operation. *J. Microelectromechanical Syst.* **2002**, *11* (6), 765–774.

(63) Chow, E. M.; Yaralioglu, G. G.; Quate, C. F.; Kenny, T. W. Characterization of

a Two-Dimensional Cantilever Array with through-Wafer Electrical Interconnects. *Appl. Phys. Lett.* **2002**, *80* (4), 664–666.

(64) Lim, J. H.; Ginger, D. S.; Lee, K. B.; Heo, J.; Nam, J. M.; Mirkin, C. A. Direct-Write Dip-Pen Nanolithography of Proteins on Modified Silicon Oxide Surfaces. *Angew. Chemie - Int. Ed.* **2003**, *42* (20), 2309–2312.

(65) Bates, F. S.; Fredrickson, G. H. Block Copolymers—Designer Soft Materials. *Phys. Today* **1999**, *52* (2), 32.

(66) Segalman, R. A. Patterning with Block Copolymer Thin Films. *Mater. Sci. Eng. R Reports* **2005**, *48* (6), 191–226.

(67) Almdal, K.; koppi, K. A.; Bates, F. S.; Mortensen, K. Multiple Ordered Phases in a Block Copolymer Melt. *Macromolecules* **1992**, *25* (6), 1743–1751.

(68) Bates, F. S.; Schulz, M. F.; Rosedale, J. H.; Almdal, K. Correlation of Binary Polyolefin Phase Behavior with Statistical Segment Length Asymmetry. *Macromolecules* **1992**, *25* (20), 5547–5550.

(69) Bates, F. S.; Schulz, M. F.; Khandpur, A. K.; Forster, S.; Rosedale, J. H.; Almdal, K.; Mortensen, K. Fluctuations, Conformational Asymmetry and Block Copolymer Phase Behaviour. *Faraday Discuss.* **1994**, *98*, 7–18.

(70) Bates, F. S.; Fredrickson, G. H. Conformational Asymmetry and Polymer-Polymer Thermodynamics. *Macromolecules* **1994**, *27* (4), 1065–1067.

(71) Krishnamoorti, R.; Graessley, W. W.; Balsara, N. P.; Lohse, D. J. Structural Origin of Thermodynamic Interactions in Blends of Saturated Hydrocarbon Polymers. *Macromolecules* **1994**, *27* (11), 3073–3081.

(72) Lin, C. C.; Jonnalagadda, S. V.; Kesani, P. K.; Dai, H. J.; Balsara, N. P. Effect of Molecular Structure on the Thermodynamics of Block Copolymer Melts. *Macromolecules* **1994**, *27* (26), 7769–7780.

(73) Graessley, W. W.; Krishnamoorti, R.; Reichart, G. C.; Balsara, N. P.; Fetters, L.

J.; Lohse, D. J. Regular and Irregular Mixing in Blends of Saturated Hydrocarbon Polymers. *Macromolecules* **1995**, *28* (4), 1260–1270.

(74) Chen, J. T.; Thomas, E. L.; Ober, C. K.; Hwang, S. S. Zigzag Morphology of a Poly(styrene-B-Hexyl Isocyanate) Rod-Coil Block Copolymer. *Macromolecules* **1995**, *28* (5), 1688–1697.

(75) Halperin, A. Rod-Coil Copolymers: Their Aggregation Behavior. *Macromolecules* **1990**, *23* (10), 2724–2731.

(76) Jeon, H. S.; Lee, J. H.; Balsara, N. P. Predictions of the Thermodynamic Properties of Multicomponent Polyolefin Blends from Measurements on Two-Component Systems. *Macromolecules* **1998**, *31* (10), 3328–3339.

(77) Almdal, K.; Hillmyer, M. A.; Bates, F. S. Influence of Conformational Asymmetry on Polymer-Polymer Interactions: An Entropic or Enthalpic Effect? *Macromolecules* **2002**, *35* (20), 7685–7691.

(78) Müller, M.; Schick, M. Ordered Phases in Rod−Coil Diblock Copolymers. *Macromolecules* **1996**, *29* (27), 8900–8903.

(79) Matsen, M. W.; Barrett, C. Liquid-Crystalline Behavior of Rod-Coil Diblock Copolymers. *J. Chem. Phys.* **1998**, *109* (10), 4108–4118.

(80) Li, W.; Gersappe, D. Self-Assembly of Rod-Coil Diblock Copolymers. *Macromolecules* **2001**, *34* (19), 6783–6789.

(81) Reenders, M.; Ten Brinke, G. Compositional and Orientational Ordering in Rod-Coil Diblock Copolymer Melts. *Macromolecules* **2002**, *35* (8), 3266–3280.

(82) Chen, J. T.; Thomas, E. L.; Ober, C. K.; Mao, G. -p. Self-Assembled Smectic Phases in Rod-Coil Block Copolymers. *Science (80-.).* **1996**, *273* (5273), 343–346.

(83) Deming, T. J. Methodologies for Preparation of Synthetic Block Copolypeptides: Materials with Future Promise in Drug Delivery. *Adv. Drug*

Deliv. Rev. **2002**, *54* (8), 1145–1155.

(84) Schlaad, H.; Antonietti, M. Block Copolymers with Amino Acid Sequences: Molecular Chimeras of Polypeptides and Synthetic Polymers. *Eur. Phys. J. E* **2003**, *10* (1), 17–23.

(85) Kukula, H.; Schlaad, H.; Antonietti, M.; F??rster, S. The Formation of Polymer Vesicles Or "peptosomes" by Polybutadiene-Block-poly(L-Glutamate)s in Dilute Aqueous Solution. *J. Am. Chem. Soc.* **2002**, *124* (8), 1658–1663.

(86) Discher, B. M. Polymersomes: Tough Vesicles Made from Diblock Copolymers. *Science (80-.).* **1999**, *284* (5417), 1143–1146.

(87) Lecommandoux, S.; Klok, H. A.; Sayar, M.; Stupp, S. I. Synthesis and Self-Organization of Rod-Dendron and Dendron-Rod-Dendron Molecules. *J. Polym. Sci. Part A Polym. Chem.* **2003**, *41* (22), 3501–3518.

(88) Breedveld, V.; Nowak, A. P.; Sato, J.; Deming, T. J.; Pine, D. J. Rheology of Block Copolypeptide Solutions: Hydrogels with Tunable Properties. *Macromolecules* **2004**, *37* (10), 3943–3953.

(89) Kolb, H. C.; Finn, M. G.; Sharpless, K. B. Click Chemistry: Diverse Chemical Function from a Few Good Reactions. *Angew. Chemie - Int. Ed.* **2001**, *40* (11), 2004–2021.

(90) Sumerlin, B. S.; Vogt, A. P. Macromolecular Engineering through Click Chemistry and Other Efficient Transformations. *Macromolecules* **2010**, *43* (1), 1–13.

(91) Lowe, A. B. Thiol-Yne "Click"/coupling Chemistry and Recent Applications in Polymer and Materials Synthesis and Modification. *Polym. (United Kingdom)* **2014**, *55* (22), 5517–5549.

(92) Arnold, R. M.; Huddleston, N. E.; Locklin, J. Utilizing Click Chemistry to Design Functional Interfaces through Post-Polymerization Modification. *J.*

Mater. Chem. **2012**, *22* (2007), 19357.

(93) Dimitriou, M. D.; Zhou, Z.; Yoo, H.-S.; Killops, K. L.; Finlay, J. A.; Cone, G.; Sundaram, H. S.; Lynd, N. A.; Barteau, K. P.; Campos, L. M.; et al. A General Approach to Controlling the Surface Composition of Poly(ethylene Oxide)-Based Block Copolymers for Antifouling Coatings. *Langmuir* **2011**, *27* (22), 13762–13772.

(94) Pelet, J. M.; Putnam, D. An in-Depth Analysis of Polymer-Analogous Conjugation Using DMTMM. *Bioconjug. Chem.* **2011**, *22* (3), 329–337.

(95) Romulus, J.; Henssler, J. T.; Weck, M. Postpolymerization Modification of Block Copolymers. *Macromolecules* **2014**, *47* (16), 5437–5449.

(96) Fournier, D.; Hoogenboom, R.; Schubert, U. S. Clicking Polymers: A Straightforward Approach to Novel Macromolecular Architectures. *Chem. Soc. Rev.* **2007**, *36* (8), 1369–1380.

(97) Speetjens, F. W.; Carter, M. C. D.; Kim, M.; Gopalan, P.; Mahanthappa, M. K.; Lynn, D. M. Post-Fabrication Placement of Arbitrary Chemical Functionality on Microphase-Separated Thin Films of Amine-Reactive Block Copolymers. *ACS Macro Lett.* **2014**, *3* (11), 1178–1182.

(98) Nam, H.; Wi, S.; Rokni, H.; Chen, M.; Priessnitz, G.; Lu, W.; Liang, X. MoS2 Transistors Fabricated via Plasma-Assisted Nanoprinting of Few-Layer MoS2 Flakes into Large-Area Arrays. *ACS Nano* **2013**, *7* (7), 5870–5881.

(99) Park, W.; Baik, J.; Kim, T. Y.; Cho, K.; Hong, W. K.; Shin, H. J.; Lee, T. Photoelectron Spectroscopic Imaging and Device Applications of Large-Area Patternable Single-Layer MoS2 Synthesized by Chemical Vapor Deposition. *ACS Nano* **2014**, *8* (5), 4961–4968.

(100) Lipomi, D. J.; Martinez, R. V.; Cademartiri, L.; Whitesides, G. M. *Soft Lithographic Approaches to Nanofabrication*; Elsevier B.V., 2012; Vol. 7.

(101) Geissler, M.; Wolf, H.; Stutz, R.; Delamarche, E.; Grummt, U. W.; Michel, B.; Bietsch, A. Fabrication of Metal Nanowires Using Microcontact Printing. *Langmuir* **2003**, *19* (15), 6301–6311.

(102) Pagliara, S.; Persano, L.; Camposeo, A.; Cingolani, R.; Pisignano, D. Registration Accuracy in Multilevel Soft Lithography. *Nanotechnology* **2007**, *18* (17), 175302.

(103) Jiang, X.; Bent, S. Area-Selective ALD with Soft Lithographic Methods: Using Self-Assembled Monolayers to Direct Film Deposition. *J. Phys. Chem. C* **2009**, *113*, 17613–17625.

(104) Shi, G.; Lu, N.; Gao, L.; Xu, H.; Yang, B.; Li, Y.; Wu, Y.; Chi, L. Fabrication of TiO2 Arrays Using Solvent-Assisted Soft Lithography. *Langmuir* **2009**, *25* (17), 9639–9643.

(105) Xia, Y. N.; Whitesides, G. M. Soft Lithography. *Annu. Rev. Mater. Sci.* **1998**, *37* (5), 551–575.

(106) Aizenberg, J.; Black, a J.; Whitesides, G. M. Control of Crystal Nucleation by Patterned Self-Assembled Monolayers. *Nature* **1999**, *398* (6727), 495–498.

(107) Barabasi, A.-L.; Stanley, H. E. Fractal Concepts in Surface Growth. *Zeitschrift für Physikalische Chemie*. 1996, pp 218–219.

(108) Addadi, L.; Moradian, J.; Shay, E.; Maroudas, N. G.; Weiner, S. A Chemical Model for the Cooperation of Sulfates and Carboxylates in Calcite Crystal Nucleation: Relevance to Biomineralization. *Proc. Natl. Acad. Sci. U. S. A.* **1987**, *84* (9), 2732–2736.

(109) Mann, S. Molecular Tectonics in Biomineralization and Biomimetic Materials Chemistry. *Nature* **1993**, *365*, 499–505.

(110) Mann, S.; Archibald, D. D.; Didymus, J. M.; Douglas, T.; Heywood, B. R.; Meldrum, F. C.; Reeves, N. J. Crystallization at Inorganic-Organic Interfaces:

Biominerals and Biomimetic Synthesis. *Science (80-.).* **1993**, *261* (43), 1286–1292.

(111) Aizenberg, J. Crystallization in Patterns: A Bio-Inspired Approach. *Adv. Mater.* **2004**, *16* (15), 1295–1302.

(112) Aizenberg, J. Direct Fabrication of Large Micropatterned Single Crystals. *Science (80-.).* **2003**, *299* (5610), 1205–1208.

(113) Briseno, A. L.; Mannsfeld, S. C. B.; Ling, M. M.; Liu, S.; Tseng, R. J.; Reese, C.; Roberts, M. E.; Yang, Y.; Wudl, F.; Bao, Z. Patterning Organic Single-Crystal Transistor Arrays. *Nature* **2006**, *444* (7121), 913–917.

(114) Wang, C. H.; Wong, A. S. W.; Ho, G. W. Facile Solution Route to Vertically Aligned, Selective Growth of ZnO Nanostructure Arrays. *Langmuir* **2007**, *23* (24), 11960–11963.

(115) Gates, B. D.; Xu, Q.; Stewart, M.; Ryan, D.; Willson, C. G.; Whitesides, G. M. New Approaches to Nanofabrication: Molding, Printing, and Other Techniques. *Chem. Rev.* **2005**, *105* (4), 1171–1196.

(116) Wouters, D.; Schubert, U. S. Nanolithography and Nanochemistry: Probe-Related Patterning Techniques and Chemical Modification for Nanometer-Sized Devices. *Angew. Chemie - Int. Ed.* **2004**, *43* (19), 2480–2495.

(117) Braunschweig, A. B.; Huo, F.; Mirkin, C. A. Molecular Printing. *Nat. Chem.* **2009**, *1* (5), 353–358.

(118) Su, M.; Li, S.; Dravid, V. P. Miniaturized Chemical Multiplexed Sensor Array. *J. Am. Chem. Soc.* **2003**, *125* (33), 9930–9931.

(119) Garno, J. C.; Yang, Y.; Amro, N. A.; Cruchon-Dupeyrat, S.; Chen, S.; Liu, G. Y. Precise Positioning of Nanoparticles on Surfaces Using Scanning Probe Lithography. *Nano Lett.* **2003**, *3* (3), 389–395.

(120) Ben Ali, M.; Ondarçuhu, T.; Brust, M.; Joachim, C. Atomic Force Microscope

Tip Nanoprinting of Gold Nanoclusters. *Langmuir* **2002**, *18* (3), 872–876.

(121) Maynor, B. W.; Li, Y.; Liu, J. Au "Ink" for AFM "Dip-Pen" Nanolithography. *Langmuir* **2001**, *17* (9), 2575–2578.

(122) Porter, L. A.; Choi, H. C.; Schmeltzer, J. M.; Ribbe, A. E.; Elliott, L. C. C.; Buriak, J. M. Electroless Nanoparticle Film Deposition Compatible with Photolithography, Microcontact Printing, and Dip-Pen Nanolithography Patterning Technologies. *Nano Lett.* **2002**, *2* (12), 1369–1372.

(123) Fu, L.; Liu, X.; Zhang, Y.; Dravid, V. P.; Mirkin, C. A. Nanopatterning Of "hard" magnetic Nanostructures via Dip-Pen Nanolithography and a Sol-Based Ink. *Nano Lett.* **2003**, *3* (6), 757–760.

(124) Su, M.; Liu, X.; Li, S. Y.; Dravid, V. P.; Mirkin, C. A. Moving beyond Molecules: Patterning Solid-State Features via Dip-Pen Nanolithography with Sol-Based Inks. *J. Am. Chem. Soc.* **2002**, *124* (8), 1560–1561.

(125) Liao, J. H.; Huang, L.; Gu, N. Fabrication of Nanoparticle Pattern through Atomic Force Microscopy Tip-Induced Deposition on Modified Silicon Surfaces. *Chin. Phys. Lett.* **2002**, *19* (1), 134–136.

(126) Li, Y.; Maynor, B.; Liu, J. Electrochemical AFM "dip-Pen" nanolithography. *J. Am. Chem. Soc.* **2001**, *123* (9), 2105–2106.

(127) Gundiah, G.; John, N. S.; Thomas, P. J.; Kulkarni, G. U.; Rao, C. N. R.; Heun, S. Dip-Pen Nanolithography with Magnetic Fe2O3 Nanocrystals. *Appl. Phys. Lett.* **2004**, *84* (26), 5341–5343.

(128) Ding, L.; Li, Y.; Chu, H.; Li, X.; Liu, J. Creation of Cadmium Sulfide Nanostructures Using AFM Dip-Pen Nanolithography. *J. Phys. Chem. B* **2005**, *109* (47), 22337–22340.

(129) Wang, Y.; Maspoch, D.; Zou, S.; Schatz, G. C.; Smalley, R. E.; Mirkin, C. a. Controlling the Shape, Orientation, and Linkage of Carbon Nanotube Features

with Nano Affinity Templates. *Proc. Natl. Acad. Sci.* **2006**, *103* (7), 2026–2031.

(130) Huang, L.; Braunschweig, A. B.; Shim, W.; Qin, L.; Lim, J. K.; Hurst, S. J.; Huo, F.; Xue, C.; Jang, J. W.; Mirkin, C. A. Matrix-Assisted Dip-Pen Nanolithography and Polymer Pen Lithography. *Small* **2010**, *6* (10), 1077–1081.

(131) Giam, L. R.; He, S.; Horwitz, N. E.; Eichelsdoerfer, D. J.; Chai, J.; Zheng, Z.; Kim, D.; Shim, W.; Mirkin, C. A. Positionally Defined, Binary Semiconductor Nanoparticles Synthesized by Scanning Probe Block Copolymer Lithography. *Nano Lett.* **2012**, *12* (2), 1022–1025.

(132) Chai, J.; Huo, F.; Zheng, Z.; Giam, L. R.; Shim, W.; Mirkin, C. a. Scanning Probe Block Copolymer Lithography. *Proc. Natl. Acad. Sci. U. S. A.* **2010**, *107* (47), 20202–20206.

(133) Liu, G.; Eichelsdoerfer, D. J.; Rasin, B.; Zhou, Y.; Brown, K. A.; Liao, X.; Mirkin, C. A. Delineating the Pathways for the Site-Directed Synthesis of Individual Nanoparticles on Surfaces. *Proc. Natl. Acad. Sci. U. S. A.* **2013**, *110* (3), 887–891.

(134) Chai, J.; Buriak, J. M. Using Cylindrical Domains of Block Copolymers to Self-Assemble and Align Metallic Nanowires. *ACS Nano* **2008**, *2* (3), 489–501.

(135) Chai, J.; Wang, D.; Fan, X. N.; Buriak, J. M. Assembly of Aligned Linear Metallic Patterns on Silicon. *Nat. Nanotechnol.* **2007**, *2* (8), 500–506.

(136) Chen, X.; Perepichka, I. I.; Bazuin, C. G. Double-Striped Metallic Patterns from PS-B-P4VP Nanostrand Templates. *ACS Appl. Mater. Interfaces* **2014**, *6* (20), 18360–18367.

(137) Kim, D. H.; Sun, Z.; Russell, T. P.; Knoll, W.; Gutmann, J. S. Organic-Inorganic Nanohybridization by Block Copolymer Thin Films. *Adv. Funct.*

Mater. **2005**, *15* (7), 1160–1164.

(138) Templin, M.; Franck, A.; Chesne, A. Du; Leist, H.; Zhang, Y.; Ulrich, R.; Schädler, V.; Wiesner, U. Organically Modified Aluminosilicate Mesostructures from Block Copolymer Phases. *Science (80-.).* **1997**, *278* (5344), 1795–1798.

(139) Lee, J.; Orilall, M. C.; Warren, S. C.; Kamperman, M.; Disalvo, F. J.; Wiesner, U. Direct Access to Thermally Stable and Highly Crystalline Mesoporous Transition-Metal Oxides with Uniform Pores. **2008**, *7* (March).

(140) Warren, S. C.; Messina, L. C.; Slaughter, L. S.; Kamperman, M.; Zhou, Q.; Gruner, S. M.; DiSalvo, F. J.; Wiesner, U. Ordered Mesoporous Materials from Metal Nanoparticle-Block Copolymer Self-Assembly. *Science (80-.).* **2008**, *320* (5884), 1748–1752.

(141) Robbins, S. W.; Beaucage, P. A.; Sai, H.; Tan, K. W.; Werner, J. G.; Sethna, J. P.; DiSalvo, F. J.; Gruner, S. M.; Van Dover, R. B.; Wiesner, U. Block Copolymer Self-Assembly-Directed Synthesis of Mesoporous Gyroidal Superconductors. *Sci. Adv.* **2016**, *2* (1), 1–8.

(142) Hur, K.; Wiesner, U. Design and Applications of Multi-Scale Organic-Inorganic Hybrid Materials Derived From Block Copolymer Self-Assembly, Special Issue on: Hierarchical Polymer Structures: 60 Years after the Staudinger Nobel Prize. *Adv. Polym. Sci.* **2013**, *262*, 259–294.

(143) Warren, S. C.; Disalvo, F. J.; Wiesner, U. Nanoparticle-Tuned Assembly and Disassembly of Mesostructured Silica Hybrids. *Nat. Mater.* **2007**, *6* (2), 156–161.

(144) Hoheisel, T. N.; Hur, K.; Wiesner, U. B. Block Copolymer-Nanoparticle Hybrid Self-Assembly. *Prog. Polym. Sci.* **2015**, *40* (1), 3–32.

(145) Song, R. Q.; Hoheisel, T. N.; Sai, H.; Li, Z.; Carloni, J. D.; Wang, S.;

Youngman, R. E.; Baker, S. P.; Gruner, S. M.; Wiesner, U.; et al. Formation of Periodically-Ordered Calcium Phosphate Nanostructures by Block Copolymer-Directed Self-Assembly. *Chem. Mater.* **2016**, *28* (3), 838–847.

(146) Gu, Y.; Dorin, R. M.; Wiesner, U. Asymmetric Organic − Inorganic Hybrid Membrane Formation via Block Copolymer − Nanoparticle Co-Assembly. *Nano Lett.* **2013**, *13*, 5323–5328.

(147) Gu, Y.; Werner, J. G.; Dorin, R. M.; Robbins, S. W.; Wiesner, U. Graded Porous Inorganic Materials Derived from Self-Assembled Block Copolymer Templates. *Nanoscale* **2015**, *7* (13), 5826–5834.

(148) Tan, K. W.; Jung, B.; Werner, J. G.; Rhoades, E. R.; Thompson, M. O.; Wiesner, U. Transient Laser Heating Induced Hierarchical Porous Structures from Block Copolymer-Directed Self-Assembly. *Science (80-.).* **2015**, *349* (6243), 54–58.

(149) Orilall, M. C.; Wiesner, U. Block Copolymer Based Composition and Morphology Control in Nanostructured Hybrid Materials for Energy Conversion and Storage: Solar Cells, Batteries, and Fuel Cells. *Chem. Soc. Rev.* **2011**, *40* (2), 520–535.

(150) Morin, S. A.; La, Y. H.; Liu, C. C.; Streifer, J. A.; Hamers, R. J.; Nealey, P. F.; Jin, S. Assembly of Nanocrystal Arrays by Block-Copolymer-Directed Nucleation. *Angew. Chemie - Int. Ed.* **2009**, *48* (12), 2135–2139.

(151) Wei, W.; Samad, L.; Choi, J. W.; Joo, Y.; Way, A.; Arnold, M. S.; Jin, S.; Gopalan, P. Synthesis of Molybdenum Disulfide Nanowire Arrays Using a Block Copolymer Template. *Chem. Mater.* **2016**, *28* (11), 4017–4023.

(152) Rolison, D. R.; Long, J. W.; Lytle, J. C.; Fischer, A. E.; Rhodes, C. P.; McEvoy, T. M.; Bourg, M. E.; Lubers, A. M. Multifunctional 3D Nanoarchitectures for Energy Storage and Conversion. *Chem. Soc. Rev.* **2009**,

38 (1), 226–252.

CHAPTER TWO

BLOCK COPOLYMER DIRECTED NANOSTRUCTURED SURFACES AS TEMPLATES FOR CONFINED SURFACE REACTIONS*

2.1 Abstract

Despite advances in nanomaterials synthesis, the bottom-up preparation of nanopatterned films as templates for spatially confined surface reactions remains a challenge. We report an approach to fabricating nanoscale thin film surface structures with periodicities on the order of 20 nm and with the capacity to localize reactions with small molecules and nanoparticles. A block copolymer (BCP) of polystyrene-*block*-poly[(allyl glycidyl ether)-*co*-(ethylene oxide)] (PS-*b*-P(AGE-*co*-EO)) is used to prepare periodically-ordered, reactive thin films. As proof-of-principle demonstrations of the versatility of the chemical functionalization, a small organic molecule, an amino acid, and ultrasmall silica nanoparticles are selectively attached via thiol-ene click chemistry to the exposed P(AGE-*co*-EO) domains of the BCP thin film. Our approach employing click chemistry on the spatially confined reactive surfaces of a BCP thin film overcomes solvent incompatibilities typically encountered when synthetic polymers are functionalized with water-soluble molecules. Moreover, this post-assembly functionalization of a reactive thin film surface preserves the original patterning, reduces the amount of required reactant, and leads to short reaction times. The demonstrated approach is expected to provide a new materials platform in applications including sensing, catalysis, pattern recognition, or microelectronics.

---

*Reprinted (adapted) with permission from K.W. Oleske, K.P. Barteau, M.Z. Turker, P.A. Beaucage, L.A. Estroff, and U. Wiesner, Block Copolymer Directed Nanostructured Surfaces as Templates for Confined Surface Reactions, *Macromolecules*, **2017**, 50 (2), 542–549 Copyright 2017 American Chemical Society.

2.2 Introduction

The demand for chemical patterning with well-defined spatial control on thin films has increased in recent years as a central part of many technologies, including photolithography and microelectronics,[1] scanning probe patterning,[2] and diagnostic arrays and lab-on-a-chip technologies in biological sciences.[3,4] Previously, polymer brush surfaces that contain a reactive functional group have been shown to have distinct advantages over pure polymers for designing and producing structured complex coatings.[5,6] While surface modification of both polymer and inorganic surfaces has taken a variety of approaches, "click" chemistries have become particularly valued for their high conversion efficiencies, chemical orthogonality, and mild reaction conditions.[7,8] Some examples include the surface reaction between propynone ferrocene and self-assembled monolayers (SAMs) of azide terminated alkylthiols on gold,[9] as well as azide-alkyne click chemistry, thiol-based additions, active ester coupling, Diels-Alder reactions, and non-aldol carbonyl chemistry to modify polymer surfaces.[10,11] These approaches generally achieve good conversion efficiencies and, via photopatterning, can yield chemical patterns with resolution on the order of microns.

Shrinking this chemical patterning down to the nanometer scale would allow for the creation of more complex nano-devices and sensors for applications where traditional lithographic fabrication has been too expensive to mass produce. In contrast to top-down lithographic techniques, bottom-up approaches utilize the chemical properties of individual molecules and their molecular recognition to control self-assembly of patterned structures. Bottom-up fabrication methods are typically more cost effective than lithography and are not limited by the spatial resolution barriers typically encountered in the latter.[12,13] Additionally, top-down and bottom-up techniques can be employed together for improved resolution and spatial control.[14]

Block copolymers (BCPs) offer high spatial resolution through their self-assembly into periodically-ordered, microphase-separated nanoscale morphologies at equilibrium.[15,16] The ability to tune BCPs by their architecture, relative block volumes, and Flory-Huggins interaction parameter to form a variety of morphologies with length scales on the order of tens of nanometers makes them an ideal platform for templating thin films.[17,18] However, while BCP self-assembly methods typically yield thin films with high spatial resolution, the chemical variety of patterned surfaces has generally been limited by a small range of block chemistries, most without moieties that can be chemically modified. Furthermore, for those BCPs with reactive groups, post-polymerization functionalization often leads to the loss of well-ordered morphologies and good spatial resolution.[19]

Synthesis of a BCP with specific reactive blocks that can be chemically modified after thin film self-assembly would allow for controlled pitch, well-defined morphology, and confined top surface chemistry. Thiol-ene chemistry is particularly desirable for this purpose due to high reaction yields, stereoselectivity, and fast reaction rates.[20,21] It has previously been shown that fluorine containing oligomers can be coupled via thiol-ene chemistry to block copolymer polystyrene-*block*-poly[(allyl glycidyl ether)-*co*-(ethylene oxide)] (PS-*b*-P(AGE-*co*-EO)) to produce polymer films with improved anti-fouling properties.[22,23] However, these reactions were carried out in solution prior to film casting, and no morphology of the parent block copolymer or functionalized polymer was reported. Moreover, by performing the reaction in solution, many of the attached moieties remain buried in the film after casting, which is not cost-effective if attaching complex molecules such as peptides or enzymes. In order to move more of the functionality to the surface of the BCP thin films, other groups have used azlactone-amine chemistry as well as sequential infiltration synthesis which utilizes organic precursors to selectively react with one domain in a

BCP.[24–27]

With these design criteria in mind, we have developed a nanostructured surface based on PS-*b*-P(AGE-*co*-EO) BCPs, on which to periodically immobilize functional groups as templates for confined surface reactions, with a spatial resolution of approximately 25 nm (Scheme 2.1). The spatial resolution and density of functional groups can be tailored by the initial BCP molar mass, volume fractions, and P(AGE-*co*-EO) block composition, respectively. Once the BCP is assembled via a combination of spin-coating and solvent annealing, small molecules and inorganic nanoparticles are attached via thiol-ene surface chemistry. This provides a top surface functionalization approach with BCP self-assembly controlled spatial resolution, which we refer to as *surface templating on assembled mesostructured polymers*, or simply "STAMP." Furthermore, in contrast to previous surface chemistries performed overnight and/or at elevated temperatures,[28] the surface chemistry described here is fast and mild, requiring as little as 30 minutes at room temperature. This approach allows for breaking through the spatial resolution barrier of top-down methods and combines ease of bottom-up processing with rapid functionalization chemistry.

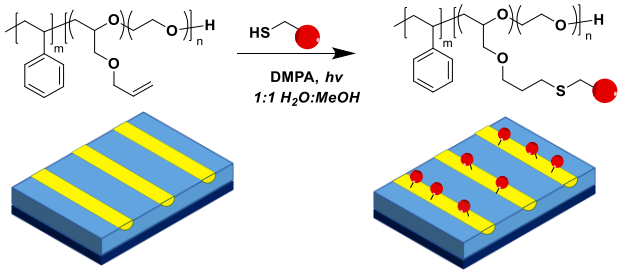

Scheme 2.1: Thin film thiol-ene chemistry where the PS is marked in blue, P(AGE-*co*-EO) in yellow, and the thiolated entity in red. In this study, the thiolated entity is either cysteine or thiolated silica nanoparticles. The PS domain width is 16 nm and the P(AGE-*co*-EO) domain width is 8 nm.

2.3 Results and Discussion

PS-*b*-P(AGE-*co*-EO) was synthesized by anionic polymerization according to previously reported methods[22] that have been modified as noted in the Experimental

Section. The resulting polymer had a molar mass of 28.5 kg/mol, a dispersity of 1.08, and volume fractions of 0.7 for PS and 0.3 for the P(AGE-*co*-EO) polyether block, as determined through a combination of ^{1}H-NMR and GPC (see Supporting Information for characterization, Figure A1.1, Figure A1.2, and Table A1.1). A ratio of 3:1 EO:AGE incorporation in the polyether block was used in order to provide a reasonable number of allyl groups for post-polymerization reaction while simultaneously suppressing any PEO crystallization.[29] The bulk BCP structure was first characterized using transmission small angle x-ray scattering (SAXS). The integrated scattering pattern, shown in Figure 2.1a, is consistent with a hexagonal cylinder morphology, as indicated by higher order reflections appearing at angular positions of $\sqrt{3}$, $\sqrt{4}$ and $\sqrt{7}$ relative to the first-order maximum. The first-order peak was centered around $q = 0.033$ Å^{-1}, corresponding to an average cylinder to cylinder distance of 22 nm.

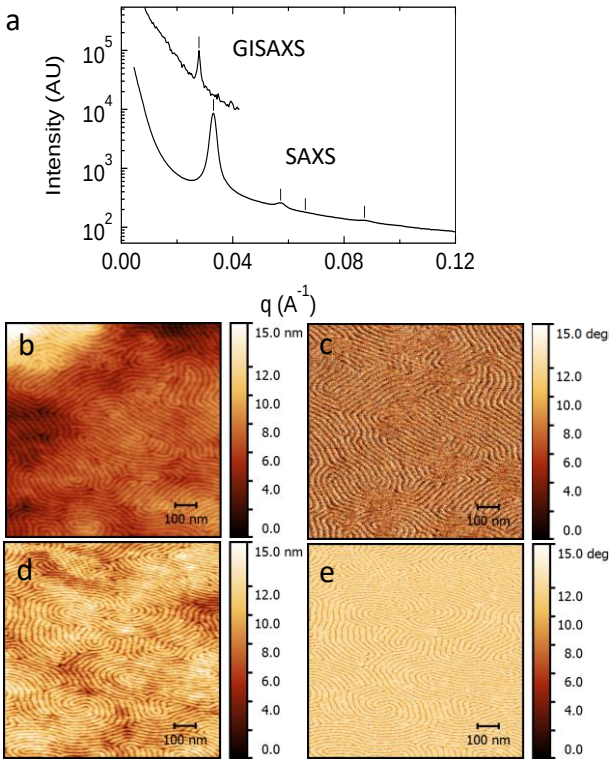

Figure 2.1: Characterization of mesophase separated BCP in the bulk and in thin films before and after functionalization with cysteines via thiol-ene reaction. (a) Integrated SAXS pattern (bottom trace) of bulk BCP sample with tick marks corresponding to expected peak positions from a hexagonal lattice with a cylinder to cylinder distance of 22 nm; GISAXS line integration (top trace) of unfunctionalized BCP thin film displaying a peak at an in-plane position corresponding to a cylinder to cylinder spacing of 26 nm. (b–e) AFM height (b, d) and phase (c, e) profiles of BCP thin film before (b, c) and after (d, e) reaction.

Nanostructured thin films with thickness of approximately 150 nm (measured by atomic force microscopy, AFM) were produced by spin-coating the BCP from a 1.2 wt% benzene solution onto a silicon wafer and then annealing in toluene vapor for 18 hours. Since it is well established that bulk and thin film morphologies can differ due to surface energy effects,[30,31] the thin film morphologies were assessed by a combination of AFM and grazing incidence small angle x-ray scattering (GISAXS). The two dimensional (2D) GISAXS pattern (see Supporting Information, Figure A1.3) displays a reflection at an in-plane position corresponding to a periodic spacing of 26

nm. For comparison to the bulk pattern, a GISAXS line cut of this reflection is also shown in Figure 2.1a. The appearance of a discrete reflection spot is consistent with the presence of phase separated domains. However, no higher-order peaks were observed by GISAXS, making a lattice assignment by GISAXS alone impossible. AFM height and phase images for these films were therefore assessed and were consistent with the presence of lying down cylinders (Figure 2.1b,c). The widths of the BCP domains were measured by AFM line traces over 30 cylinders and found to be 16±1 nm and 8±1 nm for PS and P(AGE-*co*-EO) domains, respectively. This led to a cylinder to cylinder spacing measurement of 24±2 nm, in good agreement with the periodic spacing of 26 nm obtained from the GISAXS measurement.

Since the polyether domains are expected to have reactive allyl groups on their exposed surface from the AGE moieties, it should be possible to selectively functionalize these nanodomains with thiolated molecules or nanoparticles. In general, functionalization with peptides would be very interesting as their amino acid sequence could lead to specific surface site chemistries and interactions with inorganic materials.[32–34] As a proof-of-principle toward demonstrating spatially confined surface reactivity using our STAMP method, we started with the building block of a peptide, namely the single thiol containing amino acid cysteine. The BCP thin film was surface functionalized with cysteine via thiol-ene chemistry (see Experimental Methods for reaction details) and irradiated for 8 hours. AFM was performed before and after thin film functionalization to confirm that the overall surface nanostructure of lying down BCP cylinders was preserved (Fig. 2.1b–e).

X-ray photoelectron spectroscopy (XPS) was performed on the parent, unfunctionalized BCP film and on the reacted BCP thin film to confirm the presence of cysteine after the thiol-ene reaction. As one would expect, the XPS spectrum (Supporting Information, Figure A1.4) of the parent BCP thin film lacked the peaks

for the binding energies of nitrogen N 1s (398 eV) and sulfur S 2p (164 eV). The composition of the parent polymer was calculated to be 88 atomic percent (at%) carbon and 12 at% oxygen, which is close to the expected values assuming the surface coverage of each block is the same as the bulk block fraction, estimated to be 90 at% carbon and 10 at% oxygen from ^{1}H NMR. In comparison, the XPS spectrum for the cysteine functionalized thin BCP film had both N 1s and S 2p peaks, resulting in a calculated composition of 85 at% carbon, 13 at% oxygen, 0.9 at% nitrogen, and 0.9 at% sulfur. This closely matches expected values of 88 at%, 10 at%, 1 at%, and 1 at% for C, O, N, and S, respectively, again assuming the surface coverage of each polymer block is the same as the bulk block fraction and that the yield of the thiol-ene click reaction with cysteine is quantitative. Results suggest that the surface reaction had reached near completion after 8 hours.

Fourier transform infrared spectroscopy (FTIR) measurements were performed on the BCP film before and after functionalization to look for evidence of a successful reaction. The spectra of bulk and thin film samples of the parent BCP (blue and black curves in Figure 2.2), did not contain either thioether or thiol bands at 1406 cm^{-1} and 1064 cm^{-1}, respectively.[35]

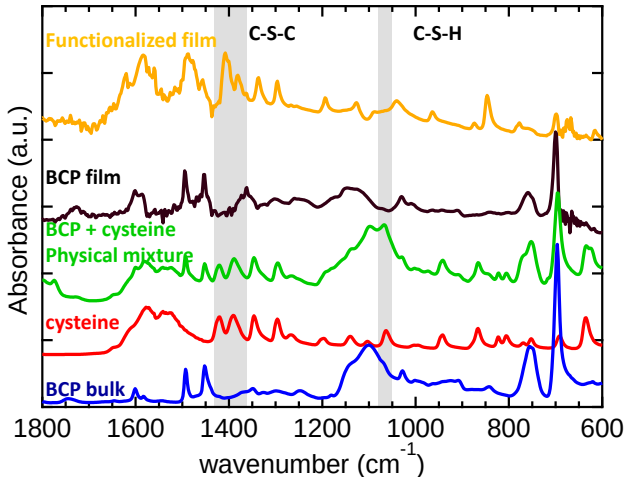

Figure 2.2: FTIR transmission spectra, from bottom to top: bulk BCP in KBr (blue), bulk cysteine in KBr (red), a bulk mixture of 3 wt% cysteine and 97 wt% BCP in a KBr pellet (green), a thin, unfunctionalized BCP film (black), and a thin BCP film functionalized with cysteine (yellow). A thiol band (C-S-H) is originally present at 1075–1045 cm^{-1} (highlighted in grey) in samples of bulk cysteine and bulk mixtures of BCP and cysteine, but disappears in the cysteine functionalized thin BCP film. Simultaneously, a thioether band (C-S-C) appears at 1420–1370 cm^{-1}, also highlighted in grey.

In contrast, the cysteine-reacted BCP thin film displayed a thioether band at 1406 cm^{-1} (yellow curve in Figure 2.2), consistent with the formation of a new C-S bond upon thiol-ene reaction. For comparison, the pure cysteine spectrum (Figure 2.2, red curve) indicates a thiol band at 1064 cm^{-1}, but no thioether band. Finally, the FTIR spectrum of a physical, unreacted mixture of 3% cysteine and 97% BCP displayed a thiol band but no thio-ether band (Figure 2.2). In summary, the appearance of the thioether band in only the FTIR spectrum of the cysteine functionalized thin film, as well as the complete disappearance of the thiol band of the cysteine, supports the covalent linkage of cysteine to the BCP film rather than physisorption.

It is worth noting that while polymer amphiphiles and peptides have been combined previously, simultaneously maintaining BCP mesostructure and achieving high reaction conversion can be challenging due to solvent incompatibilities and changes in molecule dynamics once the peptide has been attached.[36] Solvent

incompatibilities between BCPs and amino acids derive from the predominance of BCPs containing a hydrophobic block with preference for nonpolar, organic solvents, whereas, amino acids, peptides, and most biomaterials tend to dissolve well in aqueous or very polar solvents. Our approach of employing thiol-ene chemistry selectively on the reactive blocks of BCP thin films overcomes this solvent incompatibility. This approach allows free choice of an appropriate solvent for the formation of a nanostructured thin BCP film, here from PS-*b*-P(AGE-*co*-EO); it then enables functionalization of only one nanodomain of the film by independent choice of a second solvent that does not dissolve or delaminate the BCP film but selectively swells the hydrophilic block containing the AGE reactive groups. Our proof-of-principle experiments demonstrate that the thiolated small molecule is attached to the BCP without destroying the original thin film structure.

In order to verify small molecule localization within the polyether domain and to demonstrate the application of this system to inorganic constituents, an ultrasmall (diameter below 10 nm) thiolated fluorescent core-shell silica nanoparticle (NP) was designed and synthesized (for chemical and structural details, see Scheme 2.2) in aqueous solution using a modified approach to what are referred to as Cornell prime dots (C' dots).[37]

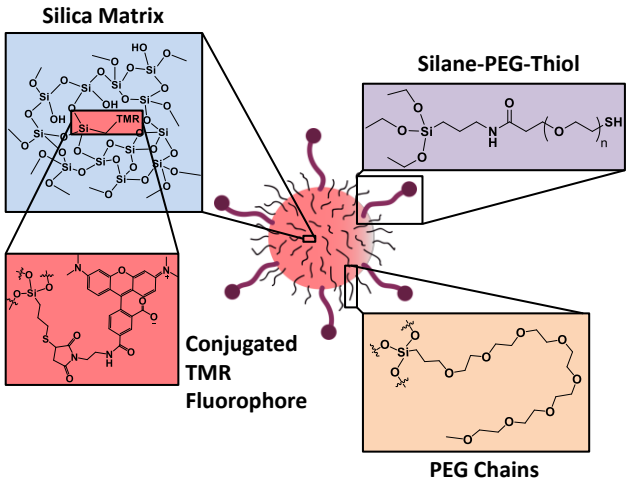

Scheme 2.2: Structure of thiolated C' dots used to confirm nanoconfined surface reactivity of nanostructured thin BCP films via inorganic patterning.

The core of the particle contains covalently encapsulated TMR dye in a silica matrix, which allows for particle size characterization by fluorescence correlation spectroscopy (FCS), a technique similar to dynamic light scattering (DLS) but more sensitive to small particle sizes.[37] The NPs were stabilized via surface PEGylation with poly(ethylene glycol)-silanes (PEG-silane). A small fraction of thiol-PEG-silanes were included in the PEGylation mixture to introduce reactive thiol ligands onto the particle, analogous to previously described methods to include fluorophore surface ligands onto C'dots.[38] The thiol-PEG-silane was chosen to be approximately 10–15 ethylene glycol repeat units longer than the unfunctionalized PEG-silane in order to make the thiol functional group more accessible to the reactive allyl-sites on the BCP thin film surface. Particle size measurements by FCS estimate the average hydrodynamic diameter of the particles to be 5–6 nm (Supporting Information, Figure A1.5) and, together with steady state optical fluorescence and absorption spectroscopy, suggest an average of 2–3 TMR dyes and 5–10 thiol groups per particle. These values are determined using optical techniques similar to previous work utilizing RGD surface ligand functionalization.[37,38]

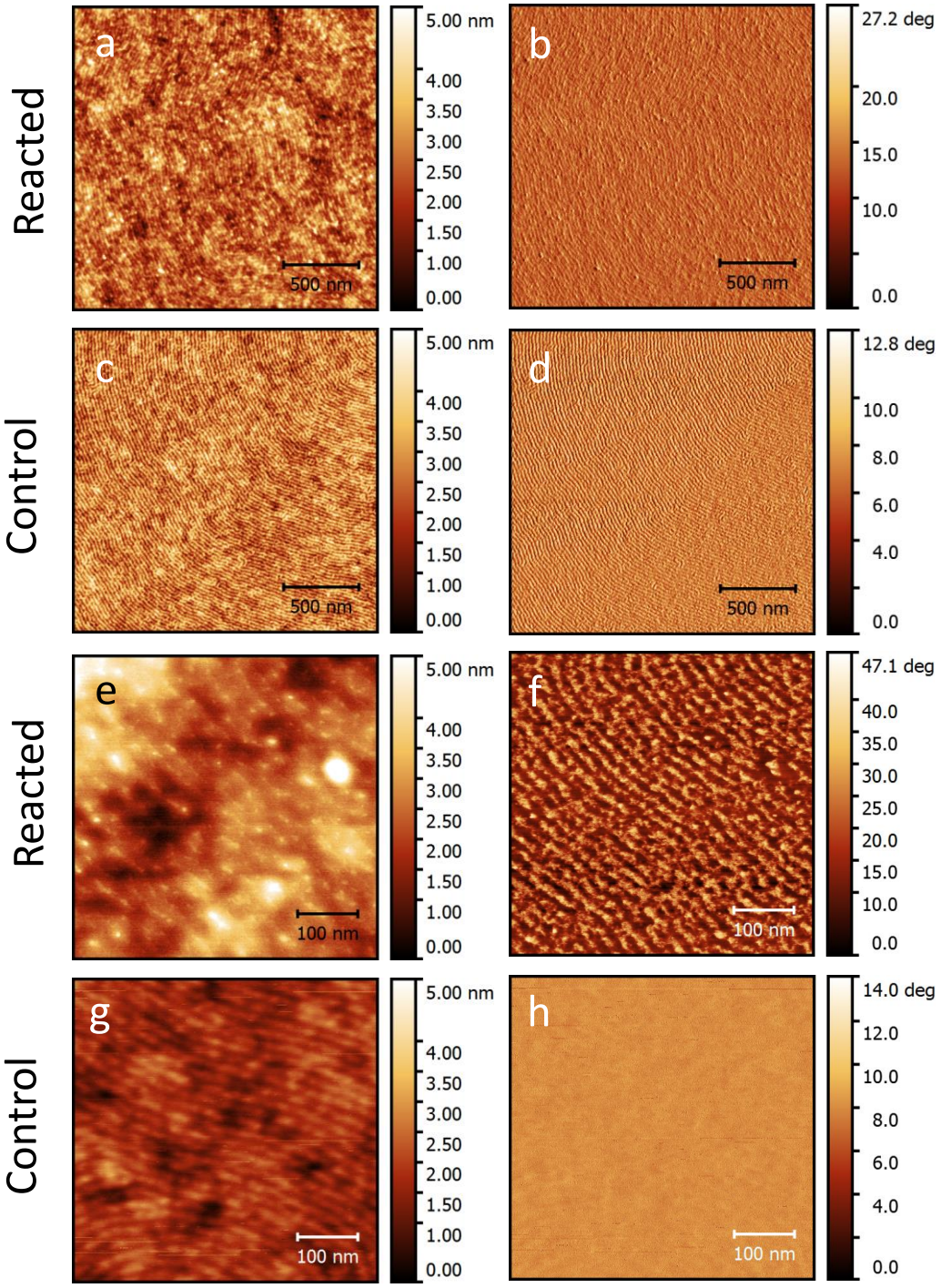

Figure 2.3: Representative AFM height (a, c, e, g) and phase (b, d, f, h) images of BCP thin films soaked in the reaction mixture containing thiolated C' dots and thiol-ene initiator (DMPA), with (a, b, e, f) and without exposure to UV light (c, d, g, h). All films were rinsed with DI water after reaction and prior to imaging. Dramatic differences, particularly in the phase profiles, appear once the BCP thin film is patterned with NPs. The phase contrast is amplified by a factor of 2 at a 2 μm scan size (b, d) and up to a factor of 5 at 500 nm scan size (f, h).

Once the small thiolated silica NPs were synthesized and characterized, a similar thiol-ene surface reaction to the cysteine reaction already described was carried out with exposure to UV light for 30 minutes (see Experimental Methods). After removal from the reaction solution, the films were washed 3 times in de-ionized (DI) water and imaged using AFM (Figure 2.3). The height profile of the NP functionalized BCP thin film surface (Figure 2.3a, 2.3e) revealed the same BCP morphology in the AFM images of the original BCP film (Figure 2.3g compared to Figure 2.1b), but with more height variation, consistent with the attachment of small (5-6 nm) particles. The phase profile also showed the same lying down cylinder BCP nanostructure as AFM images of films in Figure 1, but with increased phase contrast. In AFM, the phase contrast results from changes in the modulus of the material, and so the over 2x enhancement of phase contrast in the reacted films is consistent with the hard silica NPs being selectively reacted with just one block of the BCP. Control experiments were run to verify that there are no non-specific binding interactions of the silica NPs. BCP thin films were put into the reaction solution for 30 minutes (identical to the functionalization conditions), but were not exposed to UV light required for the thiol-ene click reaction. For the control BCP film (no UV light exposure, Figure 2.3(c, d, g, h), no particles were observed on the thin film surface, and the BCP mesostructure is well defined and matches the mesostructure seen in Figure 2.1 in both the height and phase images at a 2 μm scan displayed in Figure 2.3a and 2.3b. It is also important to note in the 2 μm scan size (Figure 2.3b and 2.3d), the phase contrast is increased by over two times, which we attribute to the relatively hard silica NPs. The phase contrast is enhanced even further at the smaller 500 nm scan size. These visual AFM results support the conclusion that the thiol-ene surface chemistry is localized to nanoscopic domains of the BCP thin film structure.

There are several interesting consequences of reacting NPs with multiple thiol

groups with the BCP films. First, the silica patterning was achieved on a much shorter time scale than the modification with cysteine (30 minutes as compared to 8 hours), and second, irradiating the silica NP reaction for longer times (1 hour) completely covers the BCP films in NPs, and the mesostructure is no longer seen by AFM (Supporting Information, Figure A1.6). Both of these observations are related to the multivalency of the silica NPs and their size. Since on average there are 5-10 thiols per particle, each particle can react multiple times with the substrate via thiol-ene chemistry. Kinetic enhancements due to proximity effects and multivalency are well-established in the literature.[39–41] More studies are necessary, however, to quantitatively evaluate the reactivity differences between monovalent small molecules like Cys, and the multivalent NPs. The size difference between the particles and the small molecules will also have to be accounted for in these models. Further complicating the picture, after the initial attachment of NPs to the surface, further reaction with NPs can occur either via thiol-ene chemistry with the BCP thin film or via disulfide formation between particles. As particles react with each other, the BCP mesostructure is obscured by multilayers of NPs. Once all of these factors are accounted for, it should be possible to control the density of particles attached to the BCP films by varying the amount of AGE groups in the P(AGE-*co*-EO) block, the number of thiols per particle, as well as the amount of time for which the reaction is irradiated.

2.4 Conclusion

A versatile approach was developed to prepare nanostructured surfaces as templates for spatially confined surface reactions. To this end, a block copolymer was used to generate periodically-ordered thin films that carry reactive functional groups in only one block, thereby enabling attachment of another species via thiol-ene click chemistry in confined, nanoscopic surface areas. The adaptability of our STAMP

method to organic and inorganic materials was demonstrated through the attachment of a small organic molecule, cysteine, and ultrasmall silica nanoparticles. It was further shown that the surface chemical reactivity overcomes limitations of bulk reactions in terms of solvent compatibilities and leads to shorter reaction times. The resulting confinement of the reactive regions of the BCP thin film surfaces to nanoscale dimensions may allow testing ideas of confinement on the reactivity of various organic and inorganic species. The demonstrated approach is further expected to provide a new materials platform taking advantage of reactivity towards different chemical species in nanoscopically confined surface areas for applications in sensing, catalysis, pattern recognition, or microelectronics.

2.5 Experimental Methods

Materials

Allyl glycidyl ether was purchased from TCI America. Deionized (DI) water was generated using a Millipore Milli-Q system. Double polished <100> silicon wafers were purchased from WRS Materials. Tetramethylrhodamine (TMR) fluorescent dye was purchased from AnaSpec. Thiol-poly(ethylene glycol) (PEG)-NHS (MW 2000 g/mol) was purchased from NanoCS, and PEG-silane (MW 500 g/mol) and (3-mercaptopropyl)trimethoxysilane (MPTMS) were purchased from Gelest. All other chemicals used were purchased from Sigma-Aldrich and used as received unless otherwise noted.

Polymer Synthesis and Characterization

PS-*b*-P(AGE-*co*-EO) was synthesized by anionic polymerization as follows: Benzene (EMD) was cleaned over *n*-butyllithium (*n*BuLi) and 1,1-diphenylethylene (DPE) prior to distillation into a dried reactor with a magnetic stir bar. Caution: *n*BuLi is pyrophoric and reacts violently with water. Styrene monomer was dried over CaH_2 overnight, degassed by three freeze-pump-thaw cycles, and distilled into a buret. In a

nitrogen glove box, sec-butyllithium was added to the reactor as the initiator followed by the distilled styrene, and the polymerization was carried out overnight. Hydroxy terminated poly(styrene) (PS-OH) was synthesized by end-capping with ethylene oxide, which had been distilled onto *n*BuLi, degassed by three freeze-pump-thaw cycles, distilled into an ampoule, and added to the reactor through inverse injection. Caution: *n*BuLi is pyrophoric and reacts violently with water. Methanolic HCl was degassed and injected to terminate the polymerization. The reaction solution was washed with aqueous sodium bicarbonate three times and deionized water twice before being returned to a clean, dry reactor with a glass coated magnetic stir bar. The benzene was removed from the PS-OH solution in the reactor by distillation, and PS-OH was dried in the reactor on the schlenk line at 130 °C for 3–4 days. Molar mass and dispersity were determined to be M_n = 20,300 g/mol and Đ = 1.02 by refractive index gel permeation chromatography (GPC) in unmodified THF using polystyrene standards.

To polymerize the copolymer block, P(AGE-*co*-EO), THF was cleaned over *n*BuLi and DPE, distilled into a separate buret, and poured into the PS-OH containing reactor inside a nitrogen filled glove box. Caution: *n*BuLi is pyrophoric and reacts violently with water. After dissolving PS-OH in THF, ca. 100 mg of potassium chloride was added to the reactor, and the chain end oxyanion was generated by adding potassium naphthalenide in THF (1 M) until the solution was green and the color persisted. Allyl glycidyl ether was stirred over butyl magnesium chloride for 30 minutes before it was distilled into an ampoule and kept frozen. Ethylene oxide was cleaned as described above and distilled directly onto the frozen AGE. The two monomers were then added to the reactor by inverse injection and polymerized for four days. After termination by degassed methanolic HCl, the THF in the reactor was exchanged for chloroform, and the polymer solution was washed with deionized water three times and precipitated

into cold methanol. The resulting copolymer had a dispersity of Đ = 1.08, as measured by THF GPC relative to polystyrene standards. Molar mass was determined to be M_n = 28,500 g/mol as calculated by ^{1}H NMR using the PS-OH M_n reported above. The assigned ^{1}H NMR spectrum of the polymer can be found in Supporting Information Figure A1.1 and agrees with the previously reported synthesis of PS-*b*-P(AGE-*co*-EO).[22]

Polymer Thin Film Assembly and Characterization

A 1.2 wt% solution of PS-*b*-P(AGE-*co*-EO) in benzene was stirred for at least 3 hours to ensure complete dissolution. Immediately prior to spin-coating, silicon wafers cut into 15 mm by 15 mm squares were cleaned by sonication in acetone for 15 minutes, followed by sonication in isopropanol for 15 minutes. The wafers were then rinsed with isopropanol, dried with nitrogen gas, and baked at 110 °C for 10 minutes. The polymer solution (~50 µL) was deposited on the dried wafer to completely cover the surface and then spun-coat for 30 seconds at 3000 rpm with an acceleration of 2000 rpm/A1.2. The films were self-assembled by solvent annealing in a toluene saturated atmosphere for 18 hours at room temperature. The morphologies and quality of the assembled films were examined by AFM and GISAXS.

Thin Film Surface Functionalization by Thiol-ene Chemistry

2,2-dimethoxy-2-phenylacetophenone (DMPA) and cysteine were added to a 10 mL 1:1 (v:v) water-methanol mixture to achieve a solution concentration of 0.05 M DMPA and 0.1 M cysteine. After the solution was stirred vigorously for 20 minutes, the solvent-annealed BCP thin film was added to the quiescent solution. The system was then sparged with nitrogen gas for 15 minutes to remove all oxygen, and the reaction mixture was exposed to UV light using a Spectroline Model ENF-260C 6W lamp with a wavelength of 365 nm and allowed to run for 8 hours. Throughout the reaction, the solution was gently agitated to prevent reagent depletion near the reacting

surface without delaminating the polymer film. The reacted film was then washed three times with DI water and allowed to dry in air. For silica nanoparticle attachment, the procedure was performed as described above, except that a 6 pM solution of thiolated C'dots (see below) with a 0.05 mM concentration of DMPA, was prepared in a 1:1 (v:v) water-methanol mixture, and the irradiation time was reduced to 30 minutes.

Synthesis of Sub-10 nm Thiolated and PEGylated Fluorescent Silica Nanoparticles

Thiolated C' Dots were synthesized following a slightly modified version of the C' Dot protocol previously reported.[37,38] Thiol-PEG-silane was synthesized in a glovebox by conjugating 0.86 µmol APTES and 0.95 µmol thiol-PEG-NHS (conjugation ratio 0.9:1.0) in dimethylsulfoxide two days prior to the PEGylation of the nanoparticles. 0.403 µmol TMR dye (Tetramethylrhodamine-6 C2 maleimide) and 10.06 µmol MPTMS (ratio 1:25) were separately conjugated in a glovebox one day prior to the nanoparticle synthesis. 100 µL of 2.0 M ammonia in ethanol was dissolved in 10 mL DI water to prepare a 0.02 M ammonia solution. 1 mL of this solution was then added into 9 mL of DI water in a 25 mL flask under stirring (600 rpm) at room temperature. 0.43 mmol TMOS and 0.403 µmol TMR dye maleimide conjugate were added to the solution, and the reaction was left stirring at room temperature overnight. 0.95 µmol of pre-synthesized Thiol-PEG-Silane (MW2000 g/mol) and 0.21 mmol PEG-Silane (MW 500 g/mol) were then added dropwise to the solution. The molar ratios of the reactants used per 1 equivalent (eq.) of TMOS were: 0.0023 eq. Thiol-PEG-Silane, 0.001 eq. TMR, 0.093 eq. ammonia, 0.49 eq. PEG-Silane, and 1292 eq. H_2O. This solution was stirred at room temperature overnight, then heated without any stirring and allowed to sit at 80 °C overnight. Afterwards, the solution was cooled to room temperature and dialyzed (10K MWCO, SnakeSkin) in 2000 mL DI water, with one buffer exchange after 24 hours. After two days of dialysis, the solution was syringe

filtered (0.2 µm, Millipore) and up-concentrated by spin-filtration (30K MWCO, GE Vivaspin). In order to remove aggregates and free dyes from the particles, GPC purification was performed using a 0.9 wt% sodium chloride solution as described elsewhere.[37,38] Afterwards, particles were transferred back into DI water. FCS measurements were performed on these purified particles to determine their size and average number of dyes encapsulated in each particle as described previously.[37,38]

Fourier Transform Infrared Spectroscopy (FTIR)

A Bruker-Hyperion FTIR instrument was used in transmission mode at a resolution of 4 cm^{-1}, a wavenumber range of 600–1800 cm^{-1}, and 2048 scan accumulation for measurement of both background and samples. The sample chamber was purged for 30 min with nitrogen before each measurement. Bulk measurements were performed on KBr pellets using identical parameter sets. KBr was dried overnight immediately before use at 110 °C, and KBr pellets were made with 1.6 mg of sample and 78 mg of KBr. The powder samples and dried KBr were first ground separately in a gate mortar to a fine powder. The appropriate amount of KBr and sample were then mixed together and ground for an additional 3–5 minutes. The final powder mixture was pressed in a Qwik Handi-Press for 2 minutes or until the pellets appeared thin and transparent.

Atomic Force Microscopy (AFM)

AFM data was collected using a Digital Instruments Multimode scanning probe microscope. Monolithic silicon non-contact high resonance frequency AFM tips with a force constant between 21–78 N/m were purchased from NanoWorld. All images were collected in tapping mode at a resolution of 512 by 512 pixels and at a scan rate of 1.2–1.0 Hz.

Small-Angle X-ray Scattering (SAXS) and Grazing Incidence Small-Angle X-ray Scattering (GISAXS)

Bulk SAXS and thin film GISAXS patterns were obtained at the Cornell High Energy Synchrotron Source (CHESS) at station G1, with a typical beam energy of 9.78 keV and sample-to-detector distance of 2 meters. GISAXS patterns were obtained 0.09° below the films' critical angle of 0.2325°, very close to grazing incidence. Patterns were recorded on a Dectris PILATUA1.3 200k pixel array detector and integrated radially (bulk SAXS) or by line cut (GISAXS) using the Nika software package[42] for Igor Pro.

X-ray Photoelectron Spectroscopy (XPS)

Samples were analyzed using a Surface Science Instruments SSX-100 with operating pressure ~$2x10^{-9}$ Torr. Monochromatic Al K-α x-rays (1486.6 eV) were used with beam diameter of 1 mm. Photoelectrons were collected at a 55° emission angle. A hemispherical analyzer determined electron kinetic energy, using a pass energy of 50 V, and a flood gun was used for charge neutralization of non-conductive samples.

ACKNOWLEDGEMENTS

This work was supported by the U.S. Department of Energy, Office of Science, Basic Energy Sciences, under Award No. DESC0010560. We thank the Cornell Center for Materials Research (CCMR) and the Cornell High Energy Synchrotron Source (CHESS) for use of their facilities, in particular the x-ray photoemission spectroscopy and polymer characterization facilities of CCMR. CCMR Facilities are supported by the National Science Foundation under Award Number DMR-1120296; CHESS is supported by the National Science Foundation and the National Institutes of Health/National Institute of General Medical Sciences under NSF award DMR-1332208. PAB was supported by the NSF Graduate Research Fellowship Program under DGE-1144153. The authors would additionally like to thank Jon Shu for his assistance with XPS characterization.

Appendix Information NMR spectra, GPC chromatography, GISAXS pattern, XPS characterization, characterization of silica NPs, and AFM of silica NPs with 1 hour reaction time

2.6 References

(1) Xia, Y. N.; Whitesides, G. M. Soft Lithography. *Annu. Rev. Mater. Sci.* **1998**, *37* (5), 551–575.

(2) Wouters, D.; Schubert, U. S. Nanolithography and Nanochemistry: Probe-Related Patterning Techniques and Chemical Modification for Nanometer-Sized Devices. *Angew. Chemie - Int. Ed.* **2004**, *43* (19), 2480–2495.

(3) Ogaki, R.; Alexander, M.; Kingshott, P. Chemical Patterning in Biointerface Science. *Mater. Today* **2010**, *13* (4), 22–35.

(4) Quist, A. P.; Chand, A.; Ramachandran, S.; Daraio, C.; Jin, S.; Lal, R. Atomic Force Microscopy Imaging and Electrical Recording of Lipid Bilayers Supported over Microfabricated Silicon Chip Nanopores: Lab-on-a-Chip System for Lipid Membranes and Ion Channels. *Langmuir* **2007**, *23* (3), 1375–1380.

(5) Barbey, R.; Lavanant, L.; Paripovic, D.; Schuwer, N.; Sugnaux, C.; Tugulu, S.; Klok, H.-A. Polymer Brushes via Surface-Initiated Controlled Radical Polymerization: Synthesis, Characterization, Properties, and Applications. *Chem. Rev.* **2009**, *109* (Copyright (C) 2012 American Chemical Society (ACS). All Rights Reserved.), 5437–5527.

(6) Orski, S. V; Fries, K. H.; Sontag, S. K.; Locklin, J. Fabrication of Nanostructures Using Polymer Brushes. *J. Mater. Chem.* **2011**, *21* (37), 14135.

(7) Evans, R. A. The Rise of Azide-Alkyne 1,3-Dipolar “Click” Cycloaddition and

Its Application to Polymer Science and Surface Modification. *Aust. J. Chem.* **2007**, *60* (6), 384–395.

(8) Escorihuela, J.; Marcelis, A. T. M.; Zuilhof, H. Metal-Free Click Chemistry Reactions on Surfaces. *Adv. Mater. Interfaces* **2015**, *2* (13), 1–42.

(9) Collman, J. P.; Devaraj, N. K.; Chidsey, C. E. D. "Clicking" Functionality onto Electrode Surfaces. *Langmuir* **2004**, *20* (4), 1051–1053.

(10) Fleischmann, S.; Hinrichs, K.; Oertel, U.; Reichelt, S.; Eichhorn, K. J.; Voit, B. Modification of Polymer Surfaces by Click Chemistry. *Macromol. Rapid Commun.* **2008**, *29* (12–13), 1177–1185.

(11) Arnold, R. M.; Huddleston, N. E.; Locklin, J. Utilizing Click Chemistry to Design Functional Interfaces through Post-Polymerization Modification. *J. Mater. Chem.* **2012**, *22* (2007), 19357.

(12) Lu, W.; Lieber, C. M. Nanoelectronics from the Bottom Up. *Nat. Mater.* **2007**, *6* (11), 841–850.

(13) Nie, Z.; Kumacheva, E. Patterning Surfaces with Functional Polymers. *Nat. Mater.* **2008**, *7* (4), 277–290.

(14) Nuraje, N.; Mohammed, S.; Yang, L.; Matsui, H. Biomineralization Nanolithography: Combination of Bottom-up and Top-down Fabrication to Grow Arrays of Monodisperse Gold Nanopartieles along Peptide Lines. *Angew. Chemie - Int. Ed.* **2009**, *48* (14), 2546–2548.

(15) Park, M.; Harrison, C.; Chaikin, P. M.; Register, R. A.; Adamson, D. A. Block Copolymer Lithography: Periodic Arrays of ~10^{11} Holes in 1 Square Centimeter. *Science.* **1997**, *276* (5317), 1401–1404.

(16) Cheng, J. Y.; Mayes, A. M.; Ross, C. A. Nanostructure Engineering by Templated Self-Assembly of Block Copolymers. *Nat. Mater.* **2004**, *3* (11), 823–828.

(17) Bates, F. S.; Fredrickson, G. H. Block Copolymers—Designer Soft Materials. *Phys. Today* **1999**, *52* (2), 32.

(18) Segalman, R. A. Patterning with Block Copolymer Thin Films. *Mater. Sci. Eng. R Reports* **2005**, *48* (6), 191–226.

(19) Olsen, B. D.; Segalman, R. A. Self-Assembly of Rod–coil Block Copolymers. *Mater. Sci. Eng. R Reports* **2008**, *62* (2), 37–66.

(20) Lowe, A. B. Thiol-Yne "Click"/coupling Chemistry and Recent Applications in Polymer and Materials Synthesis and Modification. *Polym.* **2014**, *55* (22), 5517–5549.

(21) Sumerlin, B. S.; Vogt, A. P. Macromolecular Engineering through Click Chemistry and Other Efficient Transformations. *Macromolecules* **2010**, *43* (1), 1–13.

(22) Dimitriou, M. D.; Zhou, Z.; Yoo, H.-S.; Killops, K. L.; Finlay, J. A.; Cone, G.; Sundaram, H. S.; Lynd, N. A.; Barteau, K. P.; Campos, L. M.; Fischer, D. A.; Callow, M. E.; Callow, J. A.; Ober, C. K.; Hawker, C. J.; Kramer, E. J. A General Approach to Controlling the Surface Composition of Poly(Ethylene Oxide)-Based Block Copolymers for Antifouling Coatings. *Langmuir* **2011**, *27* (22), 13762–13772.

(23) Zoelen, W. Van; Buss, H. G.; Ellebracht, N. C.; Lynd, N. a; Fischer, D. a; Finlay, J.; Hill, S.; Callow, M. E.; Callow, J. a; Kramer, E. J.; Zuckermann, R. N.; Segalman, R. a. Sequence of Hydrophobic and Hydrophilic Residues in Amphiphilic Polymer Coatings Affects Surface Structure and Marine Antifouling/ Fouling Release Properties. *ACS Macro Lett.* **2014**, 3 (4), 364-368.

(24) Riedel, M.; Stadermann, J.; Komber, H.; Simon, F.; Voit, B. Synthesis, Post-Modification and Self-Assembled Thin Films of Pentafluorostyrene Containing Block Copolymers. *Eur. Polym. J.* **2011**, *47* (4), 675–684.

(25) Speetjens, F. W.; Carter, M. C. D.; Kim, M.; Gopalan, P.; Mahanthappa, M. K.; Lynn, D. M. Post-Fabrication Placement of Arbitrary Chemical Functionality on Microphase-Separated Thin Films of Amine-Reactive Block Copolymers. *ACS Macro Lett.* **2014**, *3* (11), 1178–1182.

(26) Wei, W.; Samad, L.; Choi, J. W.; Joo, Y.; Way, A.; Arnold, M. S.; Jin, S.; Gopalan, P. Synthesis of Molybdenum Disulfide Nanowire Arrays Using a Block Copolymer Template. *Chem. Mater.* **2016**, *28* (11), 4017–4023.

(27) Romulus, J.; Henssler, J. T.; Weck, M. Postpolymerization Modification of Block Copolymers. *Macromolecules* **2014**, *47* (16), 5437–5449.

(28) Fournier, D.; Hoogenboom, R.; Schubert, U. S. Clicking Polymers: A Straightforward Approach to Novel Macromolecular Architectures. *Chem. Soc. Rev.* **2007**, *36* (8), 1369–1380.

(29) Barteau, K. P.; Wolffs, M.; Lynd, N. A.; Fredrickson, G. H.; Kramer, E. J.; Hawker, C. J. Allyl Glycidyl Ether-Based Polymer Electrolytes for Room Temperature Lithium Batteries. *Macromolecules* **2013**, *46* (22), 8988–8994.

(30) Bang, J.; Kim, B. J.; Stein, G. E.; Russell, T. P.; Li, X.; Wang, J.; Kramer, E. J.; Hawker, C. J. Effect of Humidity on the Ordering of PEO-Based Copolymer Thin Films. *Macromolecules* **2007**, *40* (19), 7019–7025.

(31) Di, Z.; Posselt, D.; Smilgies, D. M.; Papadakis, C. M. Structural Rearrangements in a Lamellar Diblock Copolymer Thin Film during Treatment with Saturated Solvent Vapor. *Macromolecules* **2010**, *43* (1), 418–427.

(32) DeOliveira, D. B.; Laursen, R. A. Control of Calcite Crystal Morphology by a Peptide Designed to Bind to a Specific Surface. *J. Am. Chem. Soc.* **1997**, *119* (44), 10627–10631.

(33) Nudelman, F.; Pieterse, K.; George, A.; Bomans, P. H.; Friedrich, H.; Brylka, L. J.; Hilbers, P. A.; de With, G.; Sommerdijk, N. A. The Role of Collagen in

Bone Apatite Formation in the Presence of Hydroxyapatite Nucleation Inhibitors. *Nat. Mater.* **2010**, *9* (12), 1004–1009.

(34) Arakaki, A.; Shimizu, K.; Oda, M.; Sakamoto, T.; Nishimura, T.; Kato, T. Biomineralization-Inspired Synthesis of Functional Organic/inorganic Hybrid Materials: Organic Molecular Control of Self-Organization of Hybrids. *Org. Biomol. Chem.* **2015**, *13* (4), 974–989.

(35) Socrates, G. *Infrared and Raman Characteristic Group Frequencies: Tables and Charts*, 3rd ed.; John Wiley and Sons, Ltd, Chichester, 2004.

(36) Hartgerink, J. D.; Beniash, E.; Stupp, S. I. Self-Assembly and Mineralization of Peptide-Amphiphile Nanofibers. *Science.* **2001**, *294* (5547), 1684–1688.

(37) Ma, K.; Mendoza, C.; Hanson, M.; Werner-Zwanziger, U.; Zwanziger, J.; Wiesner, U. Control of Ultrasmall Sub-10 Nm Ligand-Functionalized Fluorescent Core-Shell Silica Nanoparticle Growth in Water. *Chem. Mater.* **2015**, *27* (11), 4119–4133.

(38) Ma, K.; Zhang, D.; Cong, Y.; Wiesner, U. Elucidating the Mechanism of Silica Nanoparticle PEGylation Processes Using Fluorescence Correlation Spectroscopies. *Chem. Mater.* **2016**, *28* (5), 1537–1545.

(39) Mammen, M.; Choi, S.-K.; Whitesides, G. M. Polyvalent Interactions in Biological Systems: Implications for Design and Use of Multivalent Ligands and Inhibitors. *Angew. Chem. Int. Ed.* **1998**, *37* (20), 2754–2794.

(40) Mulder, A.; Huskens, J.; Reinhoudt, D. N. Multivalency in Supramolecular Chemistry and Nanofabrication. *Org. Biomol. Chem.* **2004**, *2*, 3409–3424.

(41) Badjić, J. D.; Nelson, A.; Cantrill, S. J.; Turnbull, W. B.; Stoddart, J. F. Multivalency and Cooperativity in Supramolecular Chemistry. *Acc. Chem. Res.* **2005**, *38* (9), 723–732.

(42) Ilavsky, J. Nika: Software for Two-Dimensional Data Reduction. *J. Appl.*

Crystallogr. **2012**, *45* (2), 324–328.

APPENDIX ONE

BLOCK COPOLYMER DIRECTED NANOSTRUCTURED SURFACES AS TEMPLATES FOR CONFINED SURFACE REACTIONS

List of Appendix Information Figures and Procedures

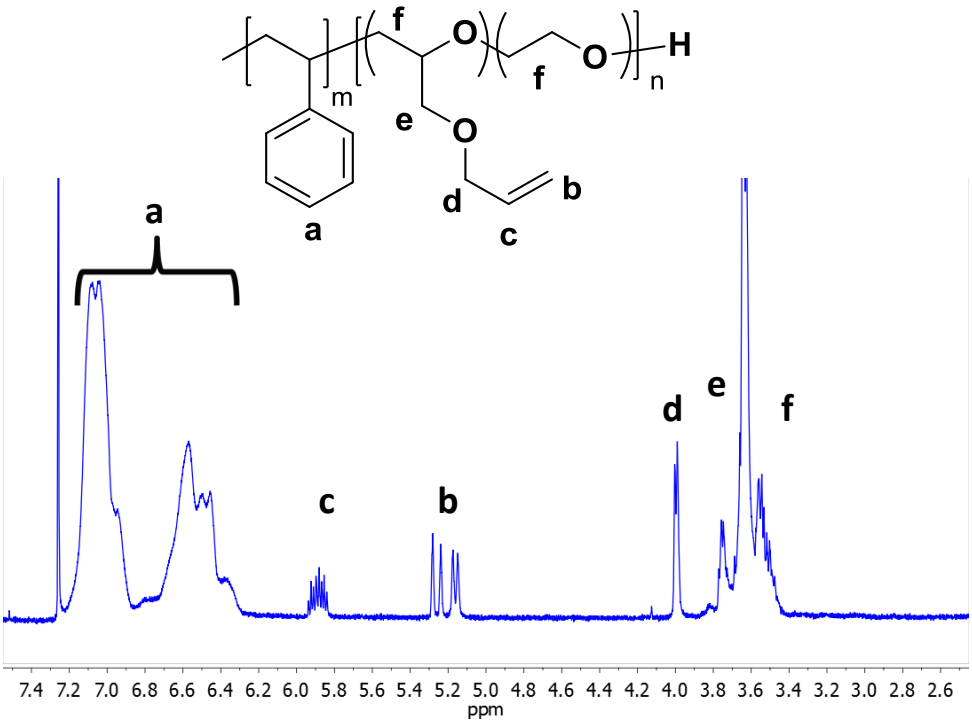

Figure A1.1: Solution ^{1}H-NMR of PS-*b*-P(AGE-*co*-EO) with peak assignments as shown.

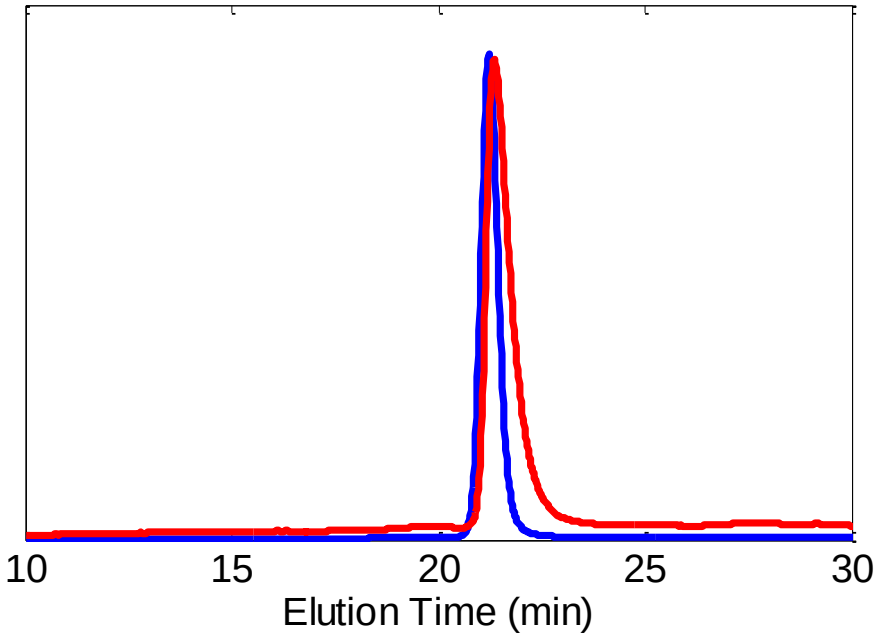

Figure A1.2: Gel permeation chromatography (GPC) traces of parent PS-OH in blue and final PS-*b*-P(AGE-*co*-EO) in red.

Table A1.1. Molecular characterization of PS-*b*-P(AGE-*co*-EO).

M_n, PS (kg/mol)[a]	M_n, P(AGE-*co*-EO) (kg/mol)[b]	f_v, PS[c]	f_v P(AGE-*co*-EO[c]	EO/AGE [b]	M_n total (kg/mol) [a]	M_w total (kg/mol) [a]	Đ [a], PS	Đ [a], total
20.3	8.2	0.7	0.3	3:1	28.5	30.7	1.02	1.08

[a]Parameters were determined by GPC in tetrahydrofuran, referenced to PS homopolymer standards.

[b]Parameters determined by ^{1}H NMR.

[c]volume fractions calculated assuming polymer densities of 1.05 g/mL for PS, 1.06 g/mL for PEO, and 1.10 g/mL for PAGE

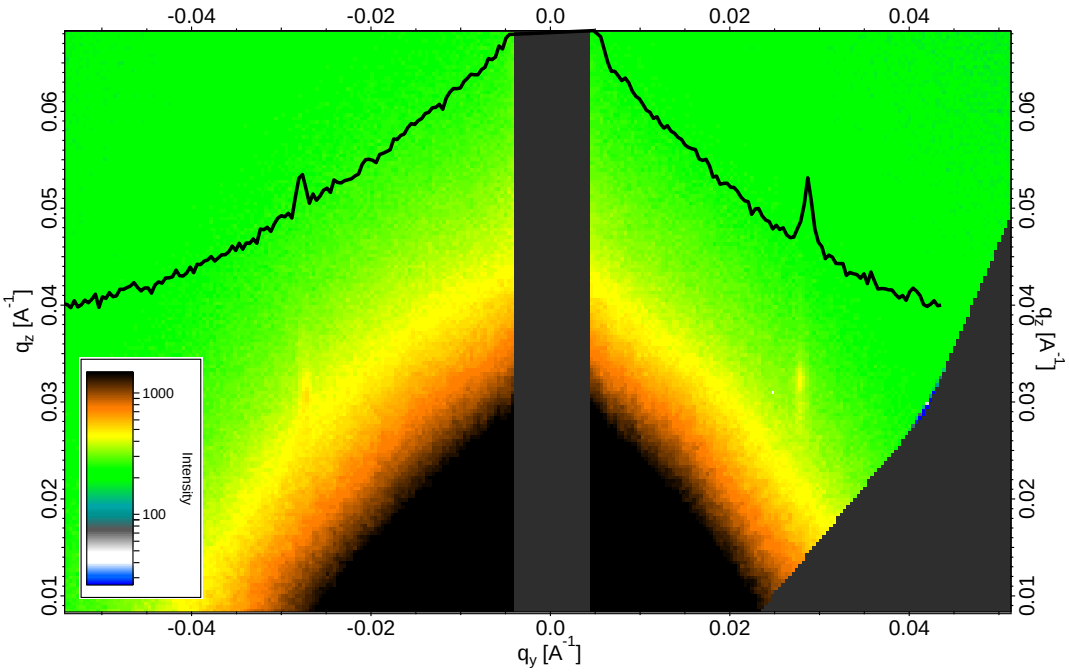

Figure A1.3: Characterization of BCP thin film. GISAXS pattern of PS-*b*-P(AGE-*co*-EO) BCP thin film displaying a reflection at an in-plane position corresponding to a spacing of 26 nm

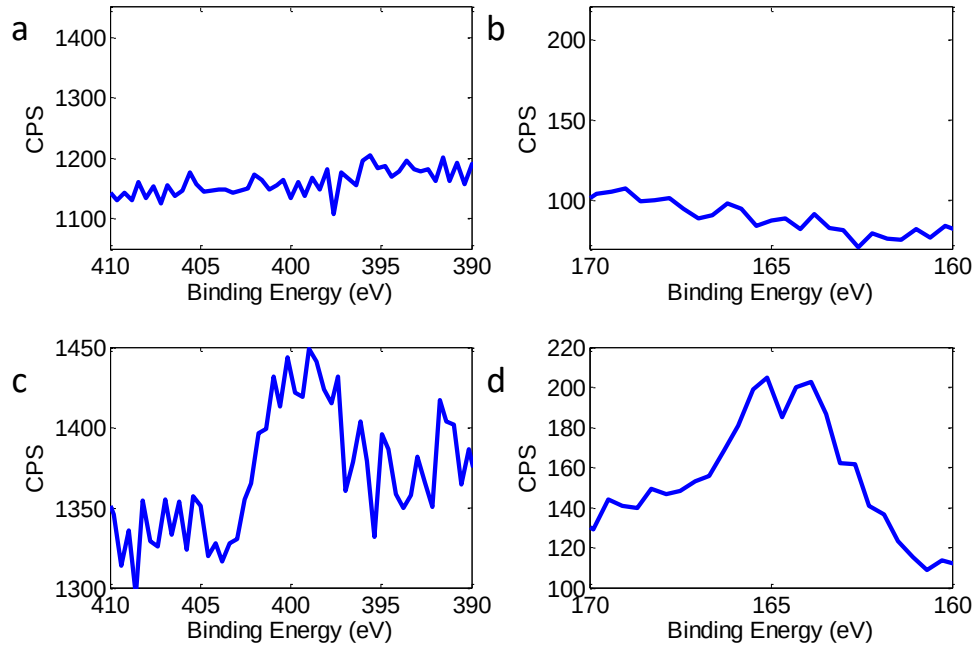

Figure A1.4: XPS characterization result for parent and cysteine surface functionalized BCP thin films. Comparison of XPS results for parent (a,b) and cysteine functionalized (c,d) thin films around values of the binding energy as expected for nitrogen (1s; a,c) and sulfur (2p; b,d) at 398 and 164 eV, respectively. Appearance of both N and S peaks in the conjugated films as compared to parent BCP film control suggests that cysteine is present on the reacted film

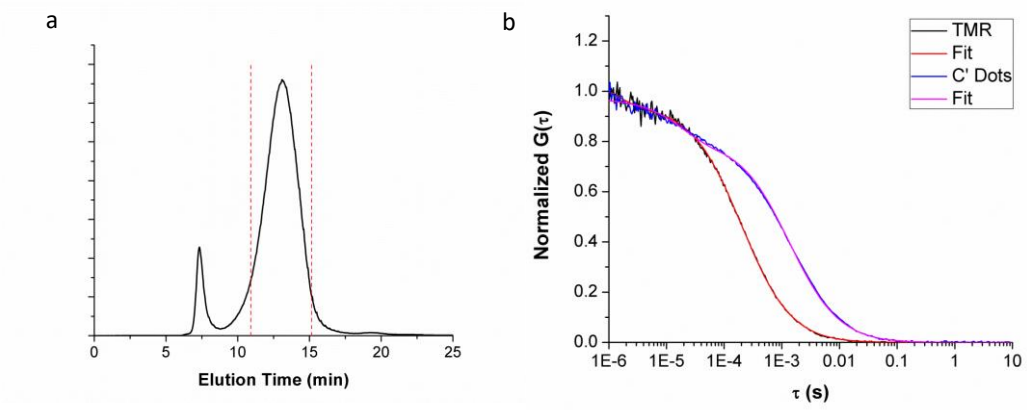

Figure A1.5: Characterization of thiolated silica nanoparticles: (a) Gel permeation chromatography (GPC) trace of an as-synthesized thiolated silica nanoparticle batch. The peak at short elution time around 7 minutes is an aggregation peak, while the main peak around 13 minutes is the desired particle peak. Particle material between the red lines was collected for the silica patterning experiments. (b) FCS curves and corresponding fits for free dye (TMR) and TMR encapsulating and thiolated nanoparticles.

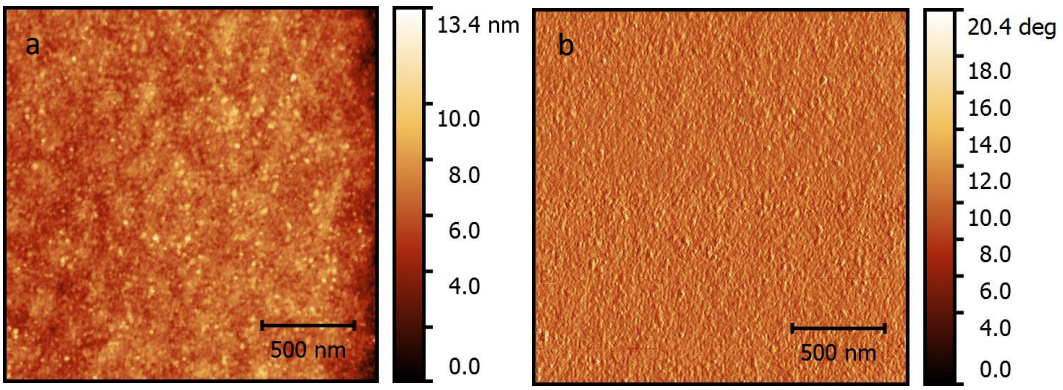

Figure A1.6: AFM height (a) and phase (b) profiles of BCP thin film after 1 hour reaction time with silica NPs.

CHAPTER THREE

NANOPATTERNING OF CRYSTALLINE TRANSITION METAL OXIDES BY SURFACE TEMPLATED NUCLEATION ON BLOCK-COPOLYMER MESOSTRUCTURES*

3.1 Abstract

While patterning the nucleation of crystalline inorganics at the nanometer length scale via low temperature, aqueous growth methods is highly desirable, it remains synthetically challenging. We report a generalizable approach for fabricating crystalline nanostructured inorganics at temperatures below 60 °C with periodicities on the order of 50 nm. A block copolymer (BCP) of polystyrene-*block*-poly[(allyl glycidyl ether)-*co*-(ethylene oxide)] (PS-*b*-P(AGE-*co*-EO)) is used to prepare periodically-ordered, reactive thin film templates that are post-assembly functionalized with an amino acid, cysteine, via thiol-ene click chemistry, exclusively at the sites of the exposed P(AGE-*co*-EO) domains. These functionalized areas subsequently template the confined crystallization of copper (I) oxide (Cu_2O) and zinc oxide (ZnO) with high fidelity, from aqueous solutions at low temperatures. The demonstrated method provides a versatile materials platform to control the growth of nanostructured crystalline materials via the introduction of a plethora of surface functional groups by means of facile thiol-ene click chemistry. The resulting organic substrates can be used to template the growth of multiple different crystalline inorganic materials on surfaces nanostructured via BCP self-assembly.

---

*Reprinted (adapted) with permission from K.W. Oleske, K.P. Barteau, P.A. Beaucage, E. Asenath-Smith, U. Wiesner, and L.A. Estroff, Nanopatterning of Crystalline Transition Metal Oxides by Surface Templated Nucleation on Block Copolymer Mesostructures, *Cryst. Growth Des.*, **2017**, 17 (11), 5775-5782 Copyright 2017 American Chemical Society.

3.2 Introduction

Although many methods exist for the synthesis of a wide range of transition metal oxide nanoparticles (0D) and nanorods (1D),[1,2] it is more challenging to template the nucleation and growth of oxides with extended and regular 2D nanopatterns. One promising strategy for the synthesis of ordered 2D nanoarrays of crystalline materials is to create chemically patterned surfaces that display organic functional groups known to nucleate the target material.[3–9] This type of approach relies on patterning a surface with nucleating domains (usually with charged functionality) surrounded by a passivating chemistry that does not favor nucleation. The difference in surface energies between the two regions then directs the heterogenous nucleation of the inorganic material only in the favorable regions. While well-established at the micron length scale using, for example, ink-jet printing, robotic deposition, and microcontact printing,[10,11] such surface-functionalization strategies for templating the growth of inorganics have not been widely realized at the tens of nanometers length scale.[12] Both top-down lithographic and direct writing techniques can achieve chemical patterning at these small length scales but are expensive and/or time-intensive processes.[13,14] Alternatively, bottom-up approaches rely on self-assembly of polymeric materials to create the nanoscale patterns and introduce the organic functionality.[10,15–17] Combinations of bottom-up and top-down approaches have also been employed for higher resolution and spatial control.[18–21] Expanding the scope of these bottom-up approaches requires the introduction of new chemistries to broaden the diversity of inorganic materials that can be templated in this way. Here, we introduce a versatile approach called *inorganic surface templating on assembled mesostructured polymers*, or simply "iSTAMP", and demonstrate its application for the growth of hexagonally ordered 2D arrays of crystalline ZnO and Cu_2O particles with periodicities of 50 nm.

Block copolymer (BCP) thin films are a desirable platform for the fabrication of 2D nanoscale templates for the growth of inorganic materials. There is a rich and well-understood diversity of mesoscale morphologies that can be achieved by tuning the chemistry and composition of amphiphilic BCPs.[22–26] Amphiphilic BCPs have been used to structure direct a variety of inorganic materials through selectively loading the hydrophilic block with inorganic precursors that are then heated, reduced or sulfurized.[27–36] This method relies on the spatial localization of the inorganic moieties within one block during BCP self-assembly and is limited by their miscibility/solubility with the common solvent(s) as well as the particular polymer block.[37–39] This approach has been extensively studied and has recently been extended to non-equilibrium-type scenarios.[20,40,41] An alternative strategy separates the BCP assembly from the nucleation and growth of the inorganic phase. Here, the nucleating functionality, usually charged moieties, must be exposed at the surface and, after incubation in a growth solution, will result in selective nucleation of the inorganic material only in regions displaying the hydrophilic block. Such a method should expand the diversity of both inorganic materials and the accessible BCP mesostructures. In an initial demonstration, Jin, Nealey, and co-workers used a poly(styrene-*block*-acrylic acid) template to direct the nucleation of metal sulfide nanocrystals.[42] Here we introduce iSTAMP, the use of a BCP thin film template[43] with a modular hydrophilic block amenable to thiol-ene "click chemistry" to template the hydrothermal growth of transition metal oxides.

Experimental Design: Our BCP template is made of a hexagonally mesostructured poly(styrene)-*block*-poly[(allyl glycidyl ether)-*co*-(ethylene oxide)] (PS-*b*-P(AGE-*co*-EO)) thin film (**iSTAMP0**, Scheme 3.1).[44] It has two chemically distinct surface functionalities: hydrophobic PS and hydrophilic, alkene containing P(AGE-*co*-EO). We have previously demonstrated the use of thiol-ene click

chemistry to tailor the surface chemistry of the hydrophilic domains using *surface templating on assembled mesostructured polymers* (STAMP).[43] Here, we use STAMP to attach a small molecule (cysteine) to the P(AGE-*co*-EO) block (**iSTAMP1**, Scheme 3.1). This zwitterionic domain is designed to play two roles in directing the selective nucleation of inorganic materials from aqueous solutions: 1) The charged amine and carboxylate moieties will attract ions, thus locally increasing the supersaturation and driving nucleation; 2) the interfacial energy between the charged domains and the inorganic materials should be low as compared to the hydrophobic PS block, promoting heterogeneous nucleation only on the hydrophilic domains. Moreover, the topology of the substrate, in which the hydrophilic domains are lower in height than the PS matrix due to selective swelling during the thin film assembly and functionalization, should also aid in directing the nucleation and growth of the inorganic crystals. Crystal growth in confinement has been used to control the size, shape, and crystallography of both organic and inorganic materials.[45,46] This highly generalizable method for the synthesis of 2D nanostructures of inorganic materials, iSTAMP, uses nanoconfined functionalization to promote the nucleation of crystalline oxides under hydrothermal conditions (below 60 °C) and allows for a diversity of both the surface chemistry in the hydrophilic block as well as the inorganic material.

3.3 Results and Discussion

iSTAMP synthesis: PS-*b*-P(AGE-*co*-EO) was synthesized by anionic polymerization according to previously reported methods that have been modified as noted in the Experimental Section.[43,44] The resulting polymer had a molar mass of 75.6 kg/mol, a polydispersity of 1.11, and volume fractions of 0.76 for PS and 0.24 for the P(AGE-*co*-EO) polyether block, as determined through a combination of ^{1}H-NMR and GPC (see Supporting Information for characterization, Figure A2.1, Figure A2.2, and Table A2.1). A ratio of 4:1 EO:AGE incorporation in the polyether block was used in

order to provide a reasonable number of allyl groups for post-polymerization reaction while simultaneously suppressing any PEO crystallization.[47]

The PS-*b*-P(AGE-*co*-EO) was spin coated onto a silicon wafer, resulting in thin films with hexagonally packed standing up cylinders (**iSTAMP0**; Scheme 3.1). As previously reported, after thiol-ene click chemical functionalization with cysteine (Cys), which exposes both amine and carboxylate groups at the surface, the hexagonally ordered surface remains intact and nanostructured (**iSTAMP1**; Scheme 3.1). In the initial report of this chemistry, we used x-ray photoelectron spectroscopy to quantify the sulfur content of **iSTAMP1** and determined that the thiol-ene click reaction on the surface neared completion after 8 h.[43]

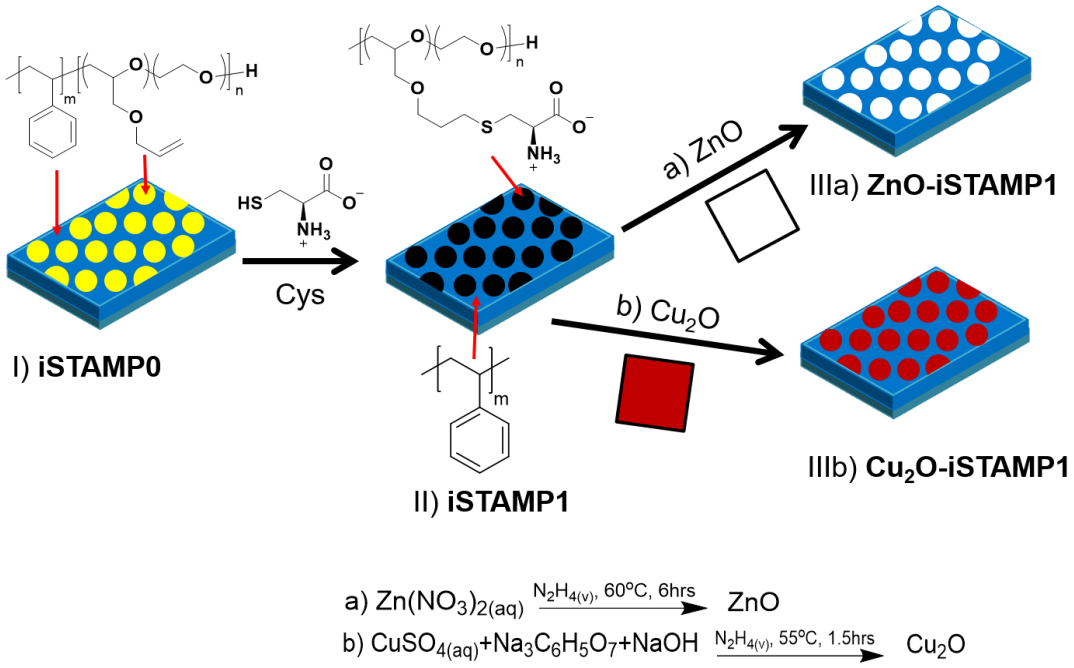

Scheme 3.1: BCP thin film assembly (**iSTAMP0**), functionalization via thiol-ene click chemistry (**iSTAMP1**), and subsequent inorganic templating (**ZnO-iSTAMP1** and **Cu₂O-iSTAMP1**).

Following thiol-ene click chemical functionalization, iSTAMP was used to grow copper (I) oxide (Cu_2O) or zinc oxide (ZnO). Ensuring sensitivity to the surface

functionalization requires these crystallizations to be performed at low supersaturations.[48] To achieve these conditions, we adapted vapor diffusion based syntheses of both ZnO and Cu_2O, in which hydrazine vapor is slowly introduced into the growth solutions to trigger nucleation selectively on the zwitterionic domains (Scheme 3.1). In the Cu_2O growth using a modified Fehling's reagent, the hydrazine serves as a reducing agent,[49,50] whereas in the ZnO growth, the hydrazine slowly raises the pH of an aqueous zinc salt solution.[51]

Morphological characterization: The mesostructure of the resulting thin films, **Cu_2O-iSTAMP1** and **ZnO-iSTAMP1**, respectively, were characterized using atomic force microscopy (AFM) and scanning electron microscopy with a backscattered electron detector (SEM-BSE), which is sensitive to changes in electron density in the sample and is used to image the spatial distribution of inorganic component on the films (Fig. 3.1a-f).

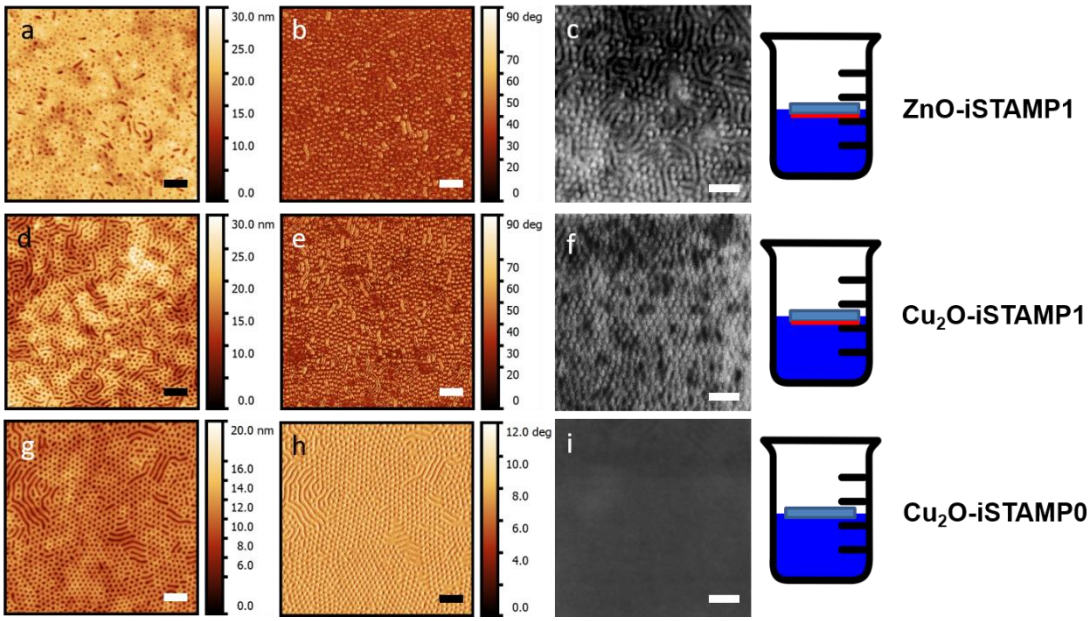

Figure 3.1: Representative template AFM height and phase images of **ZnO-iSTAMP1** (a,b), **Cu_2O-iSTAMP1** (d,e), and **Cu_2O-iSTAMP0** (control) (g,h) with corresponding SEM-BSE images of **ZnO-iSTAMP1** (c), **Cu_2O-iSTAMP1** (f), and of **Cu_2O-iSTAMP0** (control) (i). Scale bars: 200 nm.

AFM height and phase images of both **ZnO-iSTAMP1** (Fig. 3.1a,b) and **Cu_2O-iSTAMP1** (Fig. 3.1d,e) are consistent with hexagonally-packed standing up cylinders, with the occasional lying-down cylinders, as expected from the similar morphology of the control, **iSTAMP0** (Fig. A2.3). The AFM phase images for both **Cu_2O-iSTAMP1** and **ZnO-iSTAMP1** films (Fig. 3.1b,e) show increased phase contrast compared to the unmineralized film, **iSTAMP0** (Fig. A2.3), resulting from an increased modulus difference between the two regions and indicating that the inorganic material is deposited only on one of the blocks. SEM-BSE images reveal that the inorganic component is localized to the minority domain, i.e., the cylinders (Fig. 3.1c,f). Similar to the AFM images, both **Cu_2O-iSTAMP1** and **ZnO-iSTAMP1** SEM-BSE images display a hexagonal morphology, with the brighter parts of the SEM-BSE images corresponding to the minority phase. In SEM-BSE, brighter areas correspond to regions with higher *Z* elements, indicating that the inorganic material is deposited on the minority block, consistent with heterogeneous nucleation on the zwitterionic domains (Scheme 3.1).

To further characterize the mesostructure of **Cu_2O-iSTAMP1** and **ZnO-iSTAMP1**, samples were examined using transmission electron microscopy (TEM, Fig. 3.2).

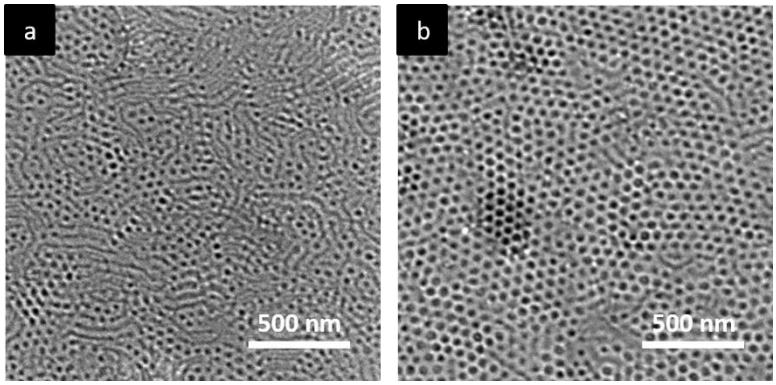

Figure 3.2: Brightfield TEM images of unstained (a) **ZnO-iSTAMP1** and (b) **Cu_2O-iSTAMP1**.

Since these samples were not stained, the contrast in the images results from the inorganic material. The TEM images of both **ZnO-iSTAMP1** and **Cu_2O-iSTAMP1** show hexagonally packed nanostructures, interspersed with lying-down cylinders. In both samples, the dense inorganic material (appearing dark) is associated with the minority phase, which is consistent with the AFM and SEM-BSE results in Fig 1.

In addition to the patterned zwitterionic functionality provided by **iSTAMP1**, there is also topology, which may contribute to the templating ability of the surface. According to the AFM data (Fig. 3.1), the hydrophilic minority domain is lower in height than the majority PS domain, leading to nanoscale "wells" on the surfaces of **iSTAMP0** and **iSTAMP1**, with an average depth of 7.9 ± 1 nm (Fig. A2.4). To determine the thickness of the inorganic layer, we measured the reduction in depth of 20 cylinders of **ZnO-iSTAMP1** or **Cu_2O-iSTAMP1** as compared to the wells on **iSTAMP0** (Fig. A2.4), i.e., determined how much inorganic material was deposited into the hydrophilic "wells". **Cu_2O-iSTAMP1** and **ZnO-iSTAMP1** had average depths of 5.5 ± 2 nm and 3.3 ± 3 nm, respectfully, leading to Cu_2O thickness of 2.4 ± 1.7 nm and ZnO thickness of 4.6 ± 2.0 nm. It is important to note that despite the lower height of some of the inorganic domains as compared to the PS matrix, the surfaces of these oxides are still accessible to solution since the reaction is performed at temperatures well below the glass transition of PS, and therefore no significant rearrangement of the matrix is observed or expected.

To probe the importance of mesostructured functionality and topology for templating the inorganic nucleation, several control experiments were performed. First, Cu_2O and ZnO were grown on glass slides with no BCP template (Figure A2.5). In these experiments, poorly defined Cu_2O aggregates on the order of 500 nm and faceted ZnO crystals (2 – 10 μm) were grown, demonstrating the importance of the

BCP **iSTAMP1** in defining the sizes of the observed 50 nm 2D nanostructures. In the second control experiment, the iSTAMP method was carried out on **iSTAMP0**, which has the same scale topology as **iSTAMP1**, but with hydrophilic and uncharged P(AGE-*co*-EO) domains, i.e., without the thiol-ene reaction step (results shown for Cu_2O in Fig 1g–i). After reaction, the BCP thin film hexagonal morphology and topology was still present (Fig. 3.1g,h). Significantly, however, there was no clear increase in phase contrast in the AFM phase image (compare Fig. 3.1b,e–h), no change in the average hydrophilic cylinder depth in the AFM height image (compare Fig. 3.1g, A2.3), and the corresponding SEM-BSE image showed no regions with brighter contrast (Fig. 3.1i). Taken together, these data suggest that no inorganic material was deposited on **iSTAMP0**. This control experiment indicates that topology alone is not sufficient to template the nucleation of the oxides and that the zwitterionic functionality in **iSTAMP1** is essential for promoting the nucleation of the inorganic materials.

The variation in the thickness of inorganic material deposited on the zwitterionic domains is likely a result of a distribution of heterogeneous nucleation events throughout the duration of the reaction time. The continuous diffusion of one of the reagents, hydrazine, into the reaction mixture maintains supersaturation until the inorganic ions are depleted from the solution. Future studies will explore changes to the reaction conditions to establish more uniform sizes of inorganic particles by creating a "nucleation burst" followed by a reduction in supersaturation to levels where only growth can occur with no new nucleation events. There will need to be a careful balance between maintaining solution conditions such that heterogeneous nucleation remains sensitive to the surface chemistry, while still achieving more uniform nucleation events.

X-ray characterization: The phase of the deposited inorganic oxides was

determined by powder x-ray diffraction (pXRD) (Fig. A2.6). The peaks in the **ZnO-iSTAMP1** diffraction pattern indexed to the (101), (102) and (110) reflections of the zincite wurtzite crystal structure (Fig. A2.6a).[52] Peaks in the pXRD pattern of **Cu_2O-iSTAMP1** indexed to the (111) and (200) reflections of the cubic-phase crystal structure of cuprite.[53]

To examine the nanoscale film structure and inorganic oxide quality in parallel over a larger film area, the iSTAMP patterned films were simultaneously measured in grazing incidence small angle x-ray scattering (GISAXS) and grazing incidence wide angle x-ray scattering (GIWAXS) configurations (Figure 3.3).

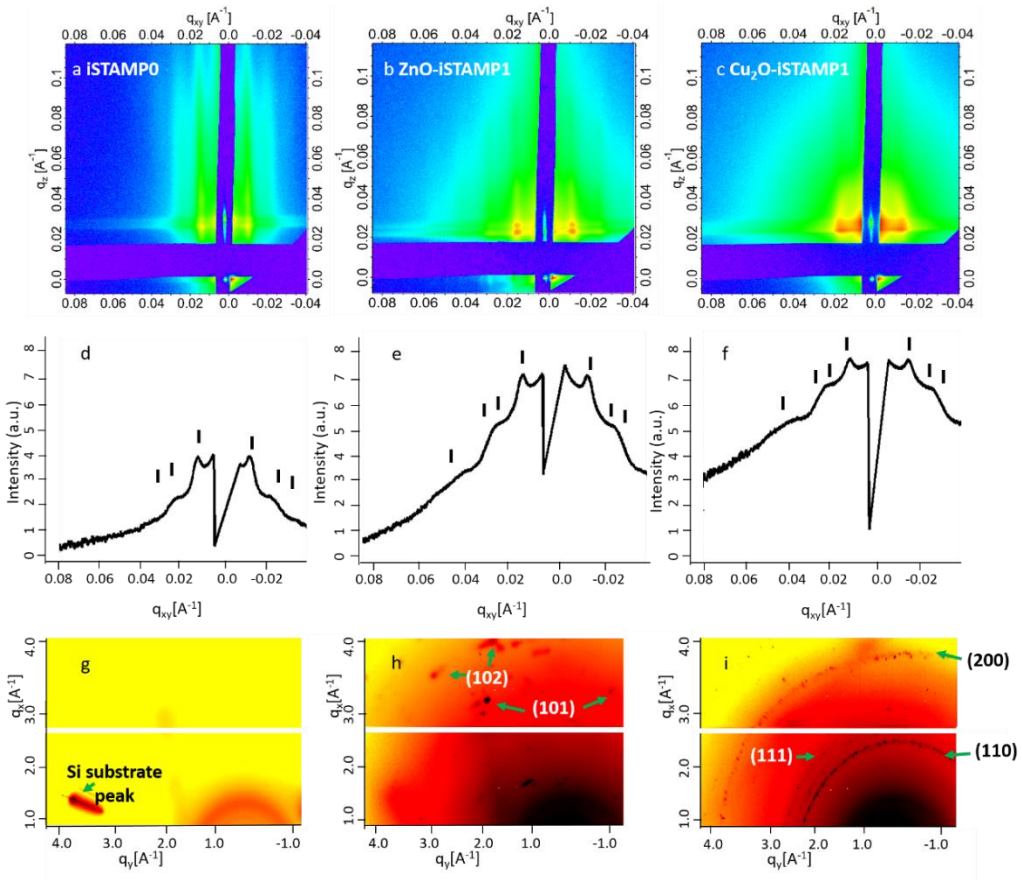

Figure 3.3: 2D GISAXS patterns of (a) **iSTAMP0**, (b) **ZnO-iSTAMP1**, and (c) **Cu$_2$O-iSTAMP1**. Integrated 1D GISAXS patterns of (d) **iSTAMP0**, (e) **ZnO-iSTAMP1**, and (f) **Cu$_2$O-iSTAMP1** with expected peak positions indicated for a hexagonal lattice with cylinder-to-cylinder distance of 52 nm. Corresponding GIWAXS patterns of (g) **iSTAMP0** with labeled Si substrate peak, (h) **ZnO-iSTAMP1** with indexed reflections (JCPDS No. 36-1451), and (i) **Cu$_2$O-iSTAMP1** with indexed reflections (JCPDS No. 05-0667).

GISAXS patterns were collected over a range of incident angles, including above the polymer critical angle where surface structure dominates (not shown), and between the polymer critical angle ($\alpha_{BCP} = 0.12°$) and silicon wafer critical angle ($\alpha_{Si} = 0.17°$) where the bulk structure of the film contributes significantly via coherent interference. The GISAXS patterns for **iSTAMP0**, **ZnO-iSTAMP1**, and **Cu$_2$O-iSTAMP1** measured at $\alpha_i = 0.14°$ are shown in Fig. 3.3 a-c. Vertical Bragg rods appear in the pattern for **iSTAMP0** at $q_{xy}^* = 0.014$ A^{-1} and more weakly at $q_{xy} = 0.024$ A^{-1}, ($q_{xy}/q_{xy}^* = 1.75$) (Figure 3a), supporting a hexagonal close packed (HCP) cylinder

morphology with an average cylinder-to-cylinder distance of 52 nm, which is close to the AFM measured distance of 57 nm and the TEM measured distance of 50 nm. The Bragg rods extending uninterrupted in q_z are indicative of finite length cylinders oriented perpendicular to the film. Given the absence of additional features in the GISAXS pattern, we assume the cylinder domains to be bounded only at the air and wafer interfaces. It is worth noting that even well below the polymer critical angle (α_i = 0.02°), the Bragg rods appear in the **iSTAMP0** film (Figure A2.7a), here arising from uniform, periodic height variations in the top surface of the film due to the selective swelling of the polymer domains during solvent annealing (see Fig. 3.1g for typical height variation).[54]

After inorganic templating, the increased surface roughness causes the Bragg rods to disappear in the low incident angle GISAXS patterns for both **ZnO-iSTAMP1** and **Cu_2O-iSTAMP1** (Fig. A2.7). However, at α_i = 0.14° (Fig 3.3b,c) the Bragg rods are still weakly present and, combined with the absence of new features in the specular profiles (Figure A2.7), indicate that the HCP cylinders of the polymer are not infiltrated throughout by the inorganic. In contrast to the lack of change in the specular profiles, the in-plane profiles of the GISAXS patterns along the Yoneda line (q_z = 0.03 A^{-1}) show increased scattering intensity and the appearance of additional higher order reflections (Fig. 3.3 d-f). Compared to the **iSTAMP0** profile, for which only one clear higher order reflection appears, additional higher order reflections are observed both for **ZnO-iSTAMP1** and **Cu_2O-iSTAMP1** and have been indexed to the same hexagonal structure factor (√3, √4, and √7 relative to the first-order reflection). The presence of stronger scattering from **ZnO-iSTAMP1** and **Cu_2O-iSTAMP1** arises from the increased scattering contrast between the templated oxide domains and polymer domains on the surface of the film, and the appearance of higher order reflections demonstrate that the patterning of the oxide onto the HCP cylinder domains

is retained over long range dimensions and provides a sharper electron density contrast.

The GIWAXS patterns for **iSTAMP0**, **ZnO-iSTAMP1**, and **Cu_2O-iSTAMP1** measured simultaneously with GISAXS are shown in Fig. 3.3g–i. As expected for **iSTAMP0**, no Bragg spots are observed other than from the underlying Si wafer. The spots in the GIWAXS pattern for **ZnO-iSTAMP1** index to the (101) and (102) reflections of the wurtzite crystal structure (Fig. 3.3h) and are consistent with the pXRD (Fig A2.6a).[52] For **Cu_2O-iSTAMP1**, the spotty rings index to the (111), (200) (both observed by pXRD), and the (110) reflection, corresponding to the cubic-phase crystal structure of cuprite (Fig. 3.3i, A2.6b).[53] The simultaneous observation of crystalline oxide by GIWAXS and enhanced HCP pattern by GISAXS demonstrates iSTAMP's ability to template inorganic materials that are both mesostructured and crystalline.

3.4 Conclusion

A mesostructured, NH_3^+/COO^- functionalized BCP thin film was used to template the growth of crystalline oxides on a 50 nm length scale. The versatility of our iSTAMP method was demonstrated by using aqueous growth solutions, usually incompatible with BCPs, to grow both crystalline ZnO and Cu_2O at low temperatures (below 60°C) and low pressures, in contrast to other methods that require higher temperatures or pressure.[1] As a result of the low temperature processing, both the crystalline inorganic and BCP template are present in the final composite, which previously has been difficult to accomplish.[33] Both the NH_3^+/COO^- functionality as well as the topology of the template are critical to the mesostructured crystalline growth of these oxides. The zwitterionic functionality locally increases the ionic concentrations near the surfaces, as well as creating a favorable interfacial energy, as compared to PS, for the nucleation of the zinc and copper oxides. The topology of the

substrate further helps to direct the growth of the inorganic crystals by confining them to the hydrophilic domains. This approach provides opportunities to combine multiple geometries of nanoscale patterns and topologies with various organic functionalities to direct and modulate the nucleation and growth of a range of inorganic species. The demonstrated iSTAMP method is thus anticipated to provide new organic-inorganic composites for applications in diverse fields including biomaterials, catalysis, and microelectronics.

3.5 Experimental Methods

Materials

Allyl glycidyl ether was purchased from TCI America. All other chemicals used were purchased from Sigma-Aldrich and used as received unless otherwise noted. Deionized (DI) water was generated using a Millipore Milli-Q system. <100> silicon wafers were purchased from WRS Materials.

Polymer Synthesis and Characterization

PS-*b*-P(AGE-*co*-EO) was synthesized by anionic polymerization as previously reported.[43,44] Molar mass and polydispersity of PS-OH were determined to be M_n = 58,000 g/mol and Đ = 1.03 by refractive index gel permeation chromatography (GPC) in THF using polystyrene standards. The final PS-*b*-P(AGE-*co*-EO) had a molar mass of M_n = 75,600 g/mol as calculated by ^{1}H NMR using the PS-OH M_n reported above, and a polydispersity of Đ = 1.11, as measured in THF by GPC relative to polystyrene standards. The peak assignments in the ^{1}H NMR spectrum of the final polymer can be found in Supporting Information Figure A2.1 and agrees with previous reports on PS-*b*-P(AGE-*co*-EO).[43]

Polymer Thin Film Assembly and Surface Functionalization by Thiol-ene Chemistry

PS-*b*-P(AGE-*co*-EO) thin films were fabricated and characterized as previously reported.[43] The films were self-assembled by solvent annealing in a benzene saturated

atmosphere for 18 hours at room temperature. PS-*b*-P(AGE-*co*-EO) thin films were then surface functionalized with cysteine using the previously reported STAMP protocol.[43]

Inorganic growth on BCP Thin Film Surfaces

The approach to surface crystallization of Cu_2O templated by the BCP nanostructure was adapted from previous work.[49,50] Stock solutions of 0.068 M copper (II) sulfate ($CuSO_4$), 0.074 M trisodium citrate (Na_3-cit) and 0.24 M sodium hydroxide (NaOH) were prepared for the Cu_2O growth. 0.5 mL of 0.068 M $CuSO_4$, 0.5 mL of 0.074 M Na_3-cit, and 0.75 mL of DI water were added to a 20 mL scintillation vial. 0.25 mL of 0.24 M NaOH solution was then added dropwise while agitating the same scintillation vial. The BCP thin film template was floated on top of the growth solution with the BCP functionalized surface facing the growth solution to prevent bulk crystals formed in solution from falling onto the template. Water tension prevented the template from sinking to the bottom. A petri dish with two slides on top was placed into a jacketed reactor with an inside temperature of 55 °C filled with 18 mL of water. The scintillation vial with growth solution and BCP template was balanced on top of the slides above the petri dish. 2 mL of hydrazine was added to the water, and the jacketed reactor was then closed. The growth was allowed to proceed for 1.5 hours, and the final composite was rinsed twice with water and once with ethanol.

Crystallization of ZnO was performed using a stock solution of 200 mM zinc nitrate $Zn(NO_3)_2$. 2 mL of stock solution was added to a 20 mL scintillation vial. The BCP thin film template was floated on top of the growth solution as described for Cu_2O growth and was allowed to soak for 1 hour before growth. A petri dish with two slides on top was placed into a jacketed reactor with an inside temperature of 60 °C filled with 15 mL of water. The scintillation vial with growth solution and BCP template was balanced on top of the slides above the petri dish. 5 mL of hydrazine

was added to the water, and the jacketed reactor was then closed. The growth was allowed to proceed for 6 hours, and the final composite film was rinsed twice with water and once with ethanol.

Control crystallizations were performed using similar reaction conditions with the following changes. The polymer film was replaced by a cleaned glass slide placed on the bottom of the scintillation vial with growth solution, since it could not float. In addition, the Cu_2O growth was allowed to proceed for 4.5 hours and the ZnO growth was allowed to proceed for 8 hours.

Atomic Force Microscopy (AFM)

All images were collected in tapping mode in air on a Digital Instruments Multimode scanning probe microscope at a resolution of 512 by 512 pixels and at a scan rate of 1.2−1.0 Hz. Monolithic silicon non-contact high resonance frequency AFM tips with a force constant between 21−78 N/m (NanoWorld) were used for imaging.

Scanning Electron Microscopy using a Backscattered Electron Detector (SEM-BSE)

SEM-BSE images were acquired with back-scattered electrons using a LEO 1550 FESEM. Images were collected at 1 kV at a working distance of ~3 mm on uncoated samples.

Transmission Electron Microscopy (TEM)

To prepare samples for TEM, a droplet of an aqueous solution of high molar mass poly(acrylic acid) was placed on the respective sample and left to dry overnight.[55] A razor blade was used to remove the droplet and film and placed into a recrystallization dish filled with DI water with the droplet facing down. The poly(acrylic acid) droplet dissolved after 2 hours and the sample was collected onto a TEM grid. The samples were imaged as-is, with no staining. TEM images were collected using a FEI T12 Spirit TEM at 120 kV.

Powder X-ray Diffraction (pXRD)

All pXRD measurements were obtained using a Scintag theta-theta X-ray diffractometer with CuK_α radiation operating at 40 kV and 30 mA with a scan rate of 1°/min, slit sizes for outcoming x-rays of 2 mm and 4 mm, and slit sizes for incoming x-rays of 1 mm and 0.5 mm.

Grazing Incidence Small-Angle X-ray Scattering (GISAXS) and Grazing Incidence Wide-Angle X-ray Scattering (GISAXS and GIWAXS)

Thin film GISAXS and GIWAXS patterns were obtained at the Cornell High Energy Synchrotron Source (CHESS) at station G1, with a typical beam energy of 9.78 keV and sample-to-detector distance of 1.7 meters for the GISAXS patterns and 0.7 meters for the GIWAXS patterns. A beam size of 250 µm x 250 µm was defined using a standard three-slit setup. GISAXS and GIWAXS patterns were obtained between 0.02° and 0.2°. GISAXS patterns were recorded on a Dectris Eiger 1M pixel array detector (PAD), and GIWAXS patterns were recorded on a Dectris Pilatus 100k PAD. GISAXS and GIWAXS patterns were collected immediately after one another without motion of the sample or incident beam, leading to the same illuminated surface for both measurements. Both GISAXS and GIWAXS patterns were analyzed using the Nika software package for Igor Pro.[56]

ACKNOWLEDGEMENTS

This work was supported by the U.S. Department of Energy, Office of Science, Basic Energy Sciences, under Award No. DE-SC0010560. We thank the Cornell Center for Materials Research (CCMR) and the Cornell High Energy Synchrotron Source (CHESS) for use of their facilities, in particular the powder x-ray diffraction, electron microscopy and polymer characterization facilities of CCMR. CCMR facilities are supported by the National Science Foundation under Award Number DMR-1719875; NMR facilities are supported by the National Science Foundation under Award

Number NSF-MRI (CHE-1531632); CHESS is supported by the National Science Foundation and the National Institutes of Health/National Institute of General Medical Sciences under NSF award DMR-1332208. PAB was supported by the NSF Graduate Research Fellowship Program under DGE-1650441.

Appendix Information

Figures A2.1-A2.7 and Table A2.1: ^{1}H-NMR spectra, GPC chromatograms, additional SEM of controls, pXRD patterns, and additional GISAXS images.

3.6 References

(1) Guo, T.; Yao, M.-S.; Lin, Y.-H.; Nan, C.-W. A Comprehensive Review on Synthesis Methods for Transition-Metal Oxide Nanostructures. *CrystEngComm* **2015**, *17* (19), 3551–3585.

(2) Kwon, S. G.; Hyeon, T. Colloidal Chemical Synthesis and Formation Kinetics of Uniformly Sized Nanocrystals of Metals, Oxides, and Chalcogenides. *Acc. Chem. Res.* **2008**, *41* (12), 1696–1709.

(3) Woodson, M.; Liu, J. Functional Nanostructures from Surface Chemistry Patterning. *Phys. Chem. Chem. Phys.* **2007**, *9* (2), 207–225.

(4) Brutchey, R. L.; Morse, D. E. Silicattein and the Translation of Its Molecular Mechanism of Biosilicification into Low Temperature Nanomaterial Synthesis. *Chem. Rev.* **2008**, *108* (11), 4915–4934.

(5) Aizenberg, J. Crystallization in Patterns: A Bio-Inspired Approach. *Adv. Mater.* **2004**, *16* (15), 1295–1302.

(6) Tian, Z. R.; Voigt, J. a; Liu, J.; McKenzie, B.; McDermott, M. J.; Rodriguez, M. A.; Konishi, H.; Xu, H. Complex and Oriented ZnO Nanostructures. *Nat. Mater.* **2003**, *2* (12), 821–826.

(7) Kisailus, D.; Choi, J. H.; Weaver, J. C.; Yang, W.; Morse, D. E. Enzymatic Synthesis and Nanostructural Control of Gallium Oxide at Low Temperature. *Adv. Mater.* **2005**, *17* (3), 314–318.

(8) Chen, C. L.; Rosi, N. L. Peptide-Based Methods for the Preparation of Nanostructured Inorganic Materials. *Angew. Chemie - Int. Ed.* **2010**, *49* (11), 1924–1942.

(9) Chen, C. L.; Su, C.; Cai, Y.; Zhang, H.; Xu, A.; Kang, B.; Loye, H. Multidimensional Frameworks Assembled from Silver (I) Coordination Polymers Containing Flexible Bis (Thioquinolyl) Ligands : Role of the Intra- and Intermolecular Aromatic Stacking Interactions. *Inorg. Chem.* **2003**, *42* (12), 3738–3750.

(10) Nie, Z.; Kumacheva, E. Patterning Surfaces with Functional Polymers. *Nat. Mater.* **2008**, *7* (4), 277–290.

(11) Aizenberg, J.; Black, a J.; Whitesides, G. M. Control of Crystal Nucleation by Patterned Self-Assembled Monolayers. *Nature* **1999**, *398* (6727), 495–498.

(12) Arora, H.; Du, P.; Tan, K. W.; Hyun, J. K.; Grazul, J.; Xin, H. L.; Muller, D. A.; Thompson, M. O.; Wiesner, U. Block Copolymer Self-Assembly Directed Single-Crystal Homo- and Heteroepitaxial Nanostructures. *Science* **2010**, *330* (6001), 214–220.

(13) Piner, R. D.; Zhu, J.; Xu, F.; Hong, S. "Dip-Pen" Nanolithography. *Science* **1999**, *283* (5402), 661–663.

(14) Giam, L. R.; He, S.; Horwitz, N. E.; Eichelsdoerfer, D. J.; Chai, J.; Zheng, Z.; Kim, D.; Shim, W.; Mirkin, C. A. Positionally Defined, Binary Semiconductor Nanoparticles Synthesized by Scanning Probe Block Copolymer Lithography. *Nano Lett.* **2012**, *12* (2), 1022–1025.

(15) Lu, W.; Lieber, C. M. Nanoelectronics from the Bottom Up. *Nat. Mater.* **2007**,

6 (11), 841–850.

(16) Kang, H.; Detcheverry, F. A.; Mangham, A. N.; Stoykovich, M. P.; Daoulas, K. C.; Hamers, R. J.; Muller, M.; De Pablo, J. J.; Nealey, P. F. Hierarchical Assembly of Nanoparticle Superstructures from Block Copolymer-Nanoparticle Composites. *Phys. Rev. Lett.* **2008**, *100* (14), 1–4.

(17) La, Y. H.; Stoykovich, M. P.; Park, S. M.; Nealey, P. F. Directed Assembly of Cylinder-Forming Block Copolymers into Patterned Structures to Fabricate Arrays of Spherical Domains and Nanoparticles. *Chem. Mater.* **2007**, *19* (18), 4538–4544.

(18) Nuraje, N.; Mohammed, S.; Yang, L.; Matsui, H. Biomineralization Nanolithography: Combination of Bottom-up and Top-down Fabrication to Grow Arrays of Monodisperse Gold Nanopartieles along Peptide Lines. *Angew. Chemie - Int. Ed.* **2009**, *48* (14), 2546–2548.

(19) Du, P.; Li, M.; Douki, K.; Li, X.; Garcia, C. B. W.; Jain, A.; Smilgies, D. M.; Fetters, L. J.; Gruner, S. M.; Wiesner, U.; et al. Additive-Driven Phase-Selective Chemistry in Block Copolymer Thin Films: The Convergence of Top-down and Bottom-up Approaches. *Adv. Mater.* **2004**, *16* (12), 953–957.

(20) Tan, K. W.; Jung, B.; Werner, J. G.; Rhoades, E. R.; Thompson, M. O.; Wiesner, U. Transient Laser Heating Induced Hierarchical Porous Structures from Block Copolymer-Directed Self-Assembly. *Science* **2015**, *349* (6243), 54–58.

(21) Sai, H.; Tan, K. W.; Hur, K.; Asenath-Smith, E.; Hovden, R.; Jiang, Y.; Riccio, M.; Muller, D. A.; Elser, V.; Estroff, L. A.; et al. Hierarchical Porous Polymer Scaffolds from Block Copolymers. *Science* **2013**, *341* (6145), 530–534.

(22) Park, M. Block Copolymer Lithography: Periodic Arrays of 10^{11} Holes in 1 Square Centimeter. *Science* **1997**, *276* (5317), 1401–1404.

(23) Cheng, J. Y.; Mayes, A. M.; Ross, C. A. Nanostructure Engineering by Templated Self-Assembly of Block Copolymers. *Nat. Mater.* **2004**, *3* (11), 823–828.

(24) Bates, F. S.; Fredrickson, G. H. Block Copolymers—Designer Soft Materials. *Phys. Today* **1999**, *52* (2), 32.

(25) Segalman, R. A. Patterning with Block Copolymer Thin Films. *Mater. Sci. Eng. R Reports* **2005**, *48* (6), 191–226.

(26) Floudas, G.; Vazaiou, B.; Schipper, F.; Ulrich, R.; Wiesner, U.; Iatrou, H.; Hadjichristidis, N. Poly(Ethylene Oxide-b-Isoprene) Diblock Copolymer Phase Diagram. *Macromolecules* **2001**, *34* (9), 2947–2957.

(27) Chai, J.; Buriak, J. M. Using Cylindrical Domains of Block Copolymers to Self-Assemble and Align Metallic Nanowires. *ACS Nano* **2008**, *2* (3), 489–501.

(28) Chai, J.; Wang, D.; Fan, X. N.; Buriak, J. M. Assembly of Aligned Linear Metallic Patterns on Silicon. *Nat. Nanotechnol.* **2007**, *2* (8), 500–506.

(29) Chen, X.; Perepichka, I. I.; Bazuin, C. G. Double-Striped Metallic Patterns from PS-b-P4VP Nanostrand Templates. *ACS Appl. Mater. Interfaces* **2014**, *6* (20), 18360–18367.

(30) Dong, B.; Kim, H.; Sun, Z.; Russell, T. P.; Knoll, W.; Gutmann, J. S. Organic-Inorganic Nanohybridization by Block Copolymer Thin Films. *Adv. Funct. Mater.* **2005**, *15* (7), 1160–1164.

(31) Wei, W.; Samad, L.; Choi, J. W.; Joo, Y.; Way, A.; Arnold, M. S.; Jin, S.; Gopalan, P. Synthesis of Molybdenum Disulfide Nanowire Arrays Using a Block Copolymer Template. *Chem. Mater.* **2016**, *28* (11), 4017–4023.

(32) Templin, M.; Franck, A.; Chesne, A. Du; Leist, H.; Zhang, Y.; Ulrich, R.; Schädler, V.; Wiesner, U. Organically Modified Aluminosilicate Mesostructures from Block Copolymer Phases. *Science* **1997**, *278* (5344),

1795–1798.

(33) Lee, J.; Orilall, M. C.; Warren, S. C.; Kamperman, M.; DiSalvo, F. J.; Wiesner, U. Direct Access to Thermally Stable and Highly Crystalline Mesoporous Transition-Metal Oxides with Uniform Pores. *Nat. Mater.* **2008**, *7* (3), 222–228.

(34) Warren, S. C.; Messina, L. C.; Slaughter, L. S.; Kamperman, M.; Zhou, Q.; Gruner, S. M.; DiSalvo, F. J.; Wiesner, U. Ordered Mesoporous Materials from Metal Nanoparticle-Block Copolymer Self-Assembly. *Science* **2008**, *320* (5884), 1748–1752.

(35) Robbins, S. W.; Beaucage, P. A.; Sai, H.; Tan, K. W.; Werner, J. G.; Sethna, J. P.; DiSalvo, F. J.; Gruner, S. M.; Van Dover, R. B.; Wiesner, U. Block Copolymer Self-Assembly-Directed Synthesis of Mesoporous Gyroidal Superconductors. *Sci. Adv.* **2016**, *2* (1), 1–8.

(36) Hur, K.; Wiesner, U. Design and Applications of Multi-Scale Organic-Inorganic Hybrid Materials Derived From Block Copolymer Self-Assembly, Special Issue on: Hierarchical Polymer Structures: 60 Years after the Staudinger Nobel Prize. *Adv. Polym. Sci.* **2013**, *262*, 259–294.

(37) Warren, S. C.; Disalvo, F. J.; Wiesner, U. Nanoparticle-Tuned Assembly and Disassembly of Mesostructured Silica Hybrids. *Nat. Mater.* **2007**, *6* (2), 156–161.

(38) Hoheisel, T. N.; Hur, K.; Wiesner, U. B. Block Copolymer-Nanoparticle Hybrid Self-Assembly. *Prog. Polym. Sci.* **2015**, *40* (1), 3–32.

(39) Song, R. Q.; Hoheisel, T. N.; Sai, H.; Li, Z.; Carloni, J. D.; Wang, S.; Youngman, R. E.; Baker, S. P.; Gruner, S. M.; Wiesner, U.; et al. Formation of Periodically-Ordered Calcium Phosphate Nanostructures by Block Copolymer-Directed Self-Assembly. *Chem. Mater.* **2016**, *28* (3), 838–847.

(40) Gu, Y.; Dorin, R. M.; Wiesner, U. Asymmetric Organic − Inorganic Hybrid

Membrane Formation via Block Copolymer − Nanoparticle Co-Assembly. *Nano Lett.* **2013**, *13*, 5323–5328.

(41) Gu, Y.; Werner, J. G.; Dorin, R. M.; Robbins, S. W.; Wiesner, U. Graded Porous Inorganic Materials Derived from Self-Assembled Block Copolymer Templates. *Nanoscale* **2015**, *7* (13), 5826–5834.

(42) Morin, S. A.; La, Y. H.; Liu, C. C.; Streifer, J. A.; Hamers, R. J.; Nealey, P. F.; Jin, S. Assembly of Nanocrystal Arrays by Block-Copolymer-Directed Nucleation. *Angew. Chemie - Int. Ed.* **2009**, *48* (12), 2135–2139.

(43) Oleske, K. W.; Barteau, K. P.; Turker, M. Z.; Beaucage, P. A.; Estroff, L. A.; Wiesner, U. Block Copolymer Directed Nanostructured Surfaces as Templates for Confined Surface Reactions. *Macromolecules* **2017**, *50* (2), 542–549.

(44) Dimitriou, M. D.; Zhou, Z.; Yoo, H.-S.; Killops, K. L.; Finlay, J. A.; Cone, G.; Sundaram, H. S.; Lynd, N. A.; Barteau, K. P.; Campos, L. M.; et al. A General Approach to Controlling the Surface Composition of Poly(Ethylene Oxide)-Based Block Copolymers for Antifouling Coatings. *Langmuir* **2011**, *27* (22), 13762–13772.

(45) Jiang, Q.; Ward, M. D. Crystallization under Nanoscale Confinement. *Chem. Soc. Rev.* **2014**, *43* (7), 2066–2079.

(46) Whittaker, M. L.; Dove, P. M.; Joester, D. Nucleation on Surfaces and in Confinement. *MRS Bull.* **2016**, *41* (5), 388–392.

(47) Barteau, K. P.; Wolffs, M.; Lynd, N. A.; Fredrickson, G. H.; Kramer, E. J.; Hawker, C. J. Allyl Glycidyl Ether-Based Polymer Electrolytes for Room Temperature Lithium Batteries. *Macromolecules* **2013**, *46* (22), 8988–8994.

(48) Hamm, L. M.; Giuffre, A. J.; Han, N.; Tao, J.; Wang, D.; De Yoreo, J. J.; Dove, P. M. Reconciling Disparate Views of Template-Directed Nucleation through Measurement of Calcite Nucleation Kinetics and Binding Energies. *Proc. Natl.*

Acad. Sci. U. S. A. **2014**, *111* (4), 1304–1309.

(49) Asenath-Smith, E.; Noble, J. M.; Hovden, R.; Uhl, A. M.; DiCorato, A.; Kim, Y.-Y.; Kulak, A. N.; Meldrum, F. C.; Kourkoutis, L. F.; Estroff, L. A. Physical Confinement Promoting Formation of Cu_2O–Au Heterostructures with Au Nanoparticles Entrapped within Crystalline Cu_2O Nanorods. *Chem. Mater.* **2017**, *29* (2), 555–563.

(50) DiCorato, A. E.; Asenath-Smith, E.; Kulak, A. N.; Meldrum, F. C.; Estroff, L. A. Cooperative Effects of Confinement and Surface Functionalization Enable the Formation of Au/Cu_2O Metal–Semiconductor Heterostructures. *Cryst. Growth Des.* **2016**, *16* (12), 6804–6811.

(51) Schwenzer, B.; Roth, K. M.; Gomm, J. R.; Murr, M.; Morse, D. E. Kinetically Controlled Vapor-Diffusion Synthesis of Novel Nanostructured Metal Hydroxide and Phosphate Films Using No Organic Reagents. *J. Mater. Chem.* **2006**, *16* (4), 401–407.

(52) Kisailus, D.; Schwenzer, B.; Gomm, J.; Weaver, J. C.; Morse, D. E. Kinetically Controlled Catalytic Formation of Zinc Oxide Thin Films at Low Temperature. *J. Am. Chem. Soc.* **2006**, *128* (31), 10276–10280.

(53) Susman, M. D.; Feldman, Y.; Vaskevich, A.; Rubinstein, I. Chemical Deposition of Cu_2O Nanocrystals with Precise Morphology. *ACS Nano* **2014**, *8* (1), 162–174.

(54) Bang, J.; Kim, B. J.; Stein, G. E.; Russell, T. P.; Li, X.; Wang, J.; Kramer, E. J.; Hawker, C. J. Effect of Humidity on the Ordering of PEO-Based Copolymer Thin Films. *Macromolecules* **2007**, *40* (19), 7019–7025.

(55) Kopp, S.; Wittmann, J. C.; Lotz, B. Epitaxial Crystallization and Crystalline Polymorphism of Poly(1-Butene): Form I. *Polymer (Guildf).* **1994**, *35* (5), 916–924.

(56) Ilavsky, J. Nika: Software for Two-Dimensional Data Reduction. *J. Appl. Crystallogr*. **2012**, *45* (2), 324–328.

APPENDIX TWO

NANOPATTERNING OF CRYSTALLINE TRANSITION METAL OXIDES BY SURFACE TEMPLATED NUCLEATION ON BLOCK-COPOLYMER MESOSTRUCTURES

List of Appendix Information Tables and Figures

Table S1. Molecular characterization of PS-*b*-P(AGE-*co*-EO).

M_n, PS (kg/mol)[a]	M_n, P(AGE-*co*-EO) (kg/mol)[b]	f_v, PS[c]	f_v P(AGE-*co*-EO)[c]	EO/AGE [b]	M_n total (kg/mol) [a]	M_w total (kg/mol) [a]	Đ [a], PS	Đ [a], total
58.0	17.6	0.76	0.24	4:1	75.6	83.9	1.03	1.11

[a]Parameters were determined by GPC in tetrahydrofuran, referenced to PS homopolymer standards.

[b]Parameters determined by ^{1}H NMR.

[c]volume fractions calculated assuming polymer densities of 1.05 g/mL for PS, 1.06 g/mL for PEO, and 1.10 g/mL for PAGE

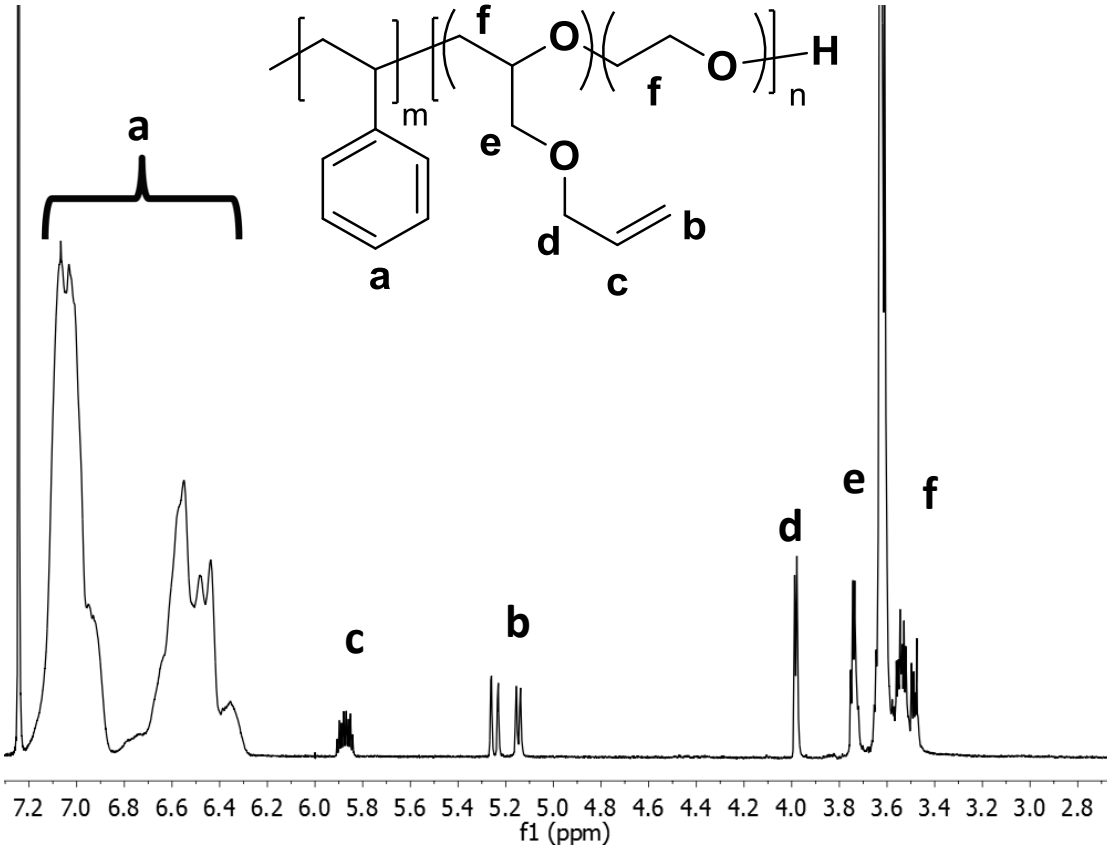

Figure A2.1: Solution ^{1}H-NMR of PS-*b*-P(AGE-*co*-EO) with peak assignments as shown.

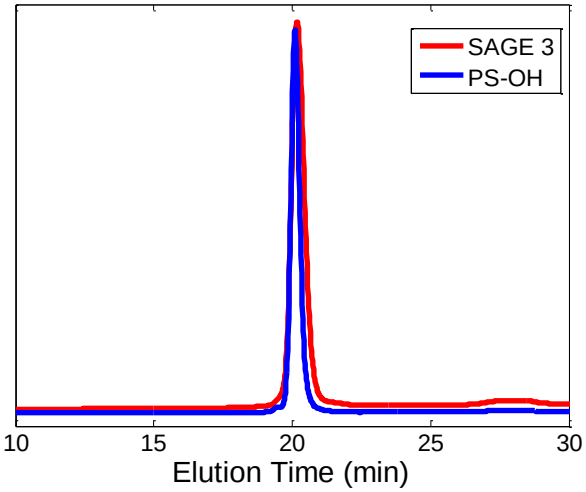

Figure A2.2: Gel permeation chromatography (GPC) traces of parent PS-OH in blue and final PS-*b*-P(AGE-*co*-EO) in red.

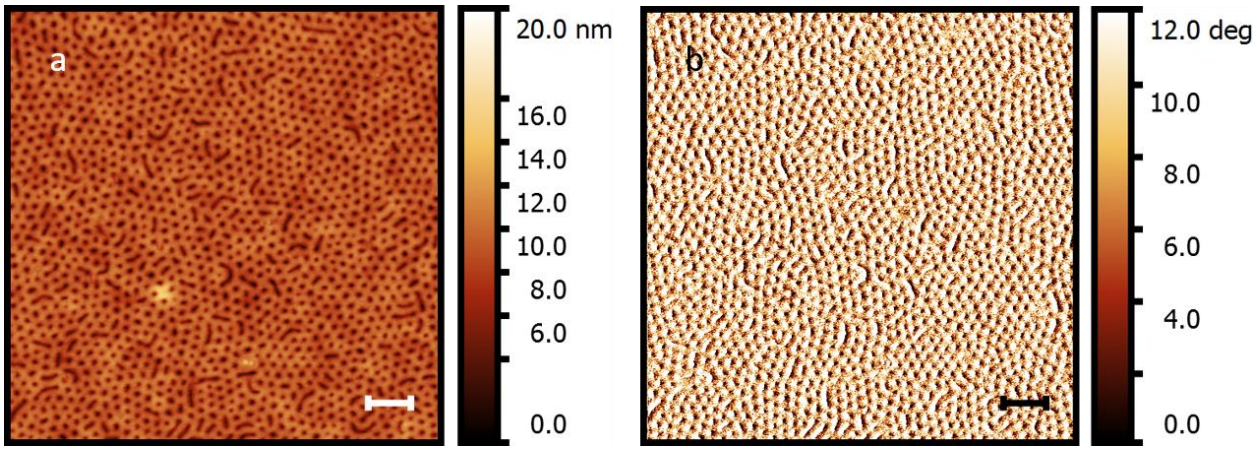

Figure A2.3: Representative AFM height (a) and phase (b) images of **iSTAMP0.**

Scale bars: 200 nm.

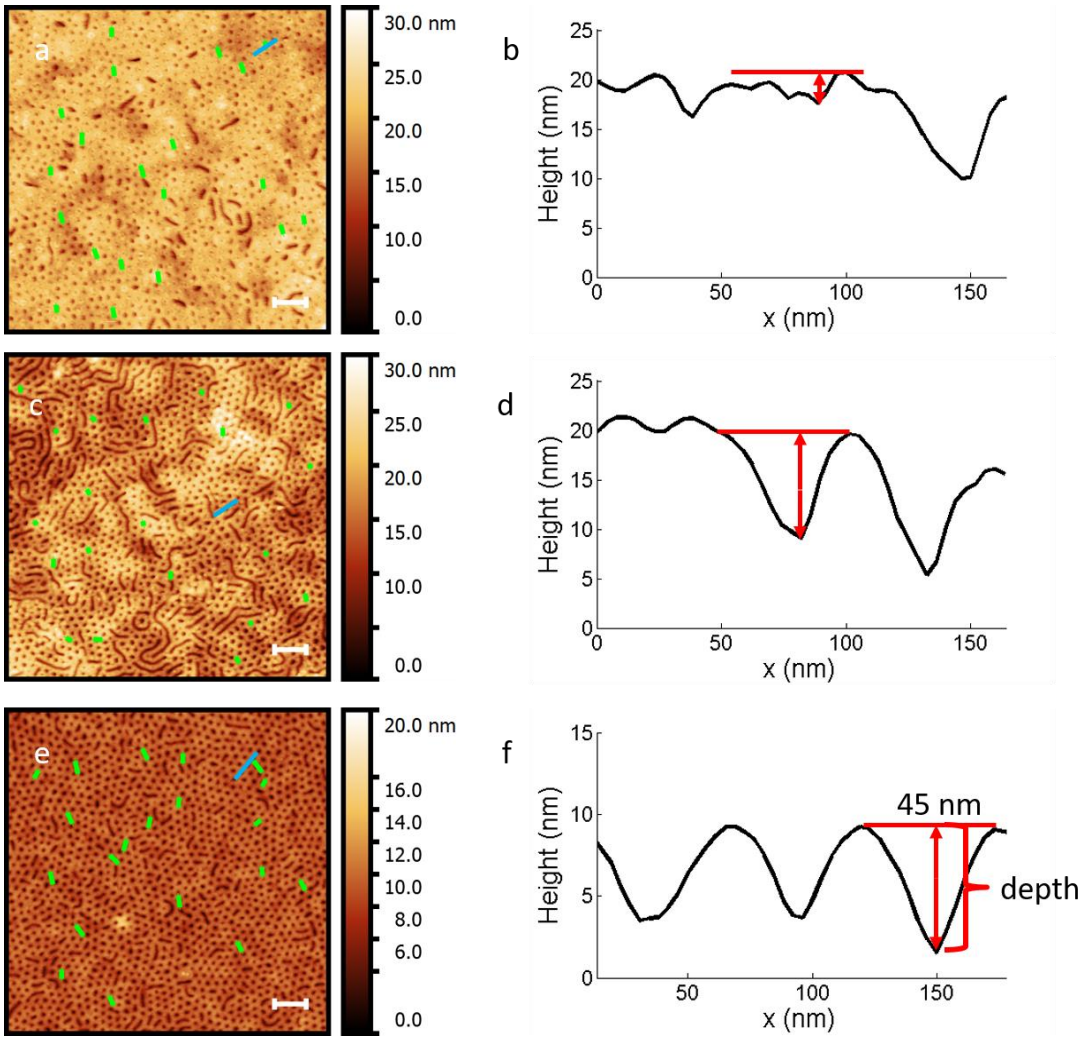

Figure A2.4: AFM height profiles of (a) **ZnO-iSTAMP1** (c) **Cu_2O-iSTAMP1** (e) **iSTAMP0** with respective representative line profiles of 3 cylinders marked in blue with example measured depths with widths of 45 nm marked in red (n = 20) (b,d,f) of Scale bars: 200 nm.

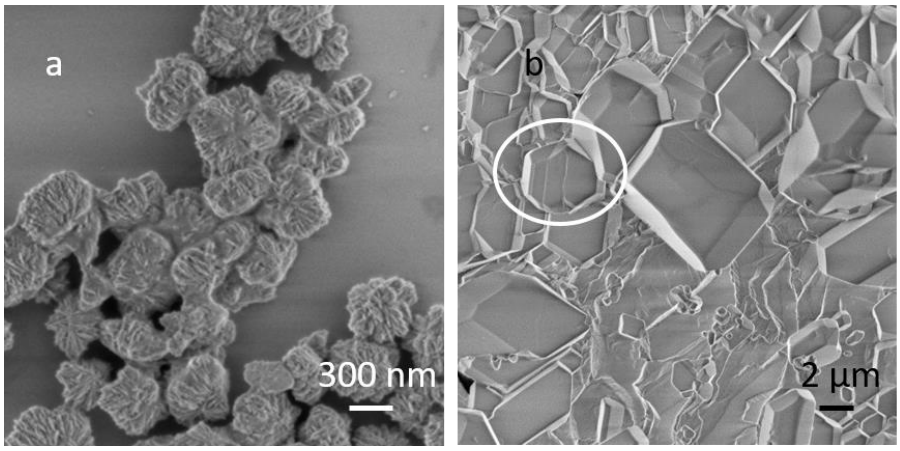

Figure A2.5: SEM images of control crystal growth experiments on unfunctionalized glass slides of (a) Cu_2O and (b) ZnO, an individual ZnO crystal is circled in (b).

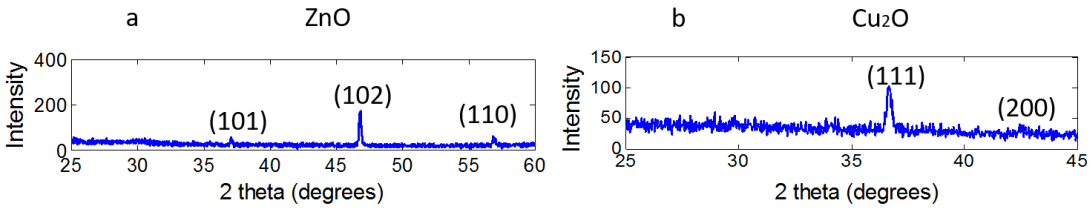

Figure A2.6: pXRD patterns of (a) **ZnO-iSTAMP1** and (b) **Cu_2O-iSTAMP1**. The diffraction peaks are labeled with crystallographic indexes according to JCPDS No. 36-1451 (ZnO) and JCPDS No. 05-0667 (Cu_2O).

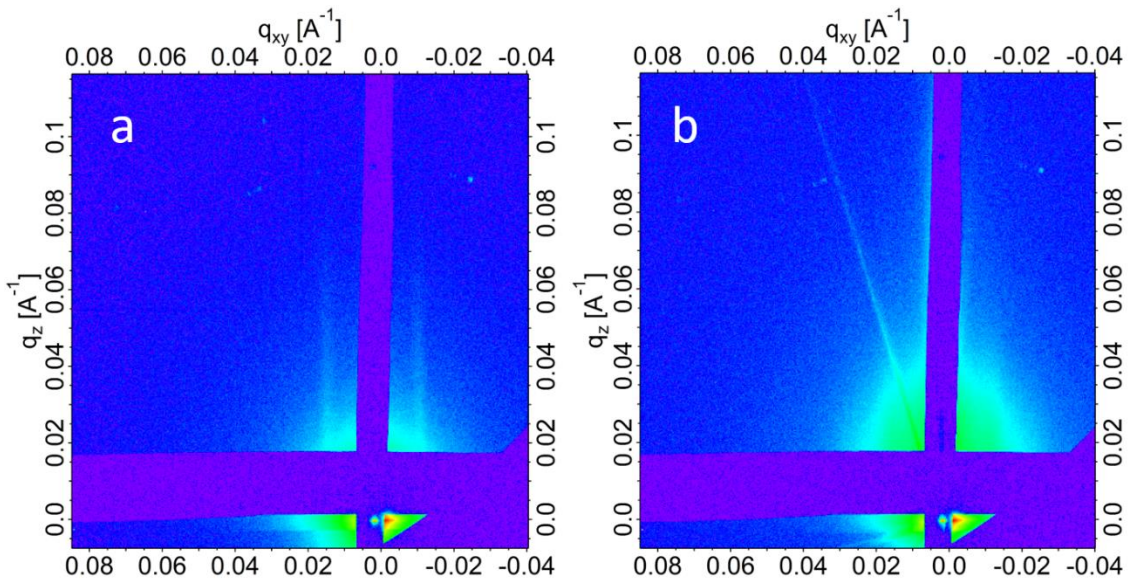

Figure A2.7: GISAXS images at polymer critical angle (α_i = 0.02°) (a) **iSTAMP0** and (b) **ZnO-iSTAMP1.**

CHAPTER FOUR

INTERPLAY OF SURFACE CHEMISTRY AND NANOCONFINEMENT IN DIRECTING CRYSTALLIZATION OF NANOSTRUCTURED TRANSITION METAL OXIDES

4.1 Abstract

In biomineralization, a common strategy for generating nanostructured crystalline inorganics is to combine surface chemistry with nanometer confinement to simultaneously control nucleation and growth. Implementing similar strategies in experimental systems to direct heterogeneous nucleation and growth of transition metal oxides at the nanoscale remains a major challenge. Here, employing polymer self-assembly to fabricate model thin film surfaces, with tunable chemistry and topology, we investigated templating the low temperature growth of zinc oxide (ZnO) and copper (I) oxide (Cu_2O). A polystyrene-*block*-poly[(allyl glycidyl ether)-*co*-(ethylene oxide)] (PS-*b*-P(AGE-*co*-EO)) block copolymer was used to prepare reactive thin film substrates periodically-ordered on the 50 nm scale that were post-assembly functionalized with 3-mercaptopropionic acid, cysteamine, or 2-mercaptoethanol to provide nanoscopically confined anionic, cationic, and neutral surfaces for inorganic material formation. The templated organic-inorganic composites were characterized by a combination of atomic force microscopy (AFM), transmission electron microscopy (TEM), and grazing incidence wide- and small-angle x-ray scattering (GIWAXS and GISAXS). The study elucidated details on how oxide material growth, shape, crystal structure, and orientation vary as a function of surface chemistry, topology, and confinement. Specifically, two different growth pathways are proposed: one based upon chelation of metal cations by anionic substrates and the other based upon binding of pre-formed clusters to cationic

substrates. Such model studies may help to develop design criteria to access low temperature pathways to nanostructured crystalline materials for a number of different applications including energy conversion and storage.

4.2 Introduction

Biology couples nanoscale confinement and surface chemistry to grow, at low temperatures (< 100°C), hierarchical composite structures formed from nanometer scale organic and inorganic building blocks, such as bones and teeth.[1] The combination of confinement and local surface chemistry enables organisms to use organic matrices to control precisely the location and number of nucleation events, which in turn determine the polymorph, orientation, shape, and size of the crystalline phase.[2,3,4,5,6,7,8] While organisms in biology readily combine confinement with surface chemical functionality to create composites of organic and crystalline inorganic materials, it is still difficult to achieve this level of structural control, particularly at the 10's of nanometer scale, in completely synthetic systems. Most synthetic approaches to date have used either confinement or patterned surface chemical functionality when synthesizing crystalline inorganic structures.

Crystallization under nanoscale confinement is used to study how the kinetics and thermodynamics of nucleation and growth change compared to bulk crystallization.[9] For example, it has been observed that metastable polymorphs can be stabilized in confinement, and that crystals grown in confinement can have different crystal properties (e.g., suppression of freezing points).[10–14] One synthetic method for achieving confinement, based upon biological inspiration, uses synthetic liposomes, vesicles made up of one or more lipid bilayers, to grow crystalline iron oxides, calcium phosphates, and earth alkaline carbonates.[15,16] The size of the synthetic liposome can range from 50 nm to 50 μm in diameter, and this variable changes the

nucleation and growth rate of the respective inorganic phase.[17,18] Track-etch membranes have also been able to confine inorganic crystallization on the nanoscale in at least one direction to control the nucleation and growth of multiple different inorganic materials.[19–22] It has been observed that the degree of confinement can control the inorganic's nucleation rate,[20,23,24] and sometimes even capture metastable precursors which are difficult to observe in bulk approaches.[19,21,25] To date, however, these studies have not paired nano-confinement effects with surface chemistry.

The use of patterned surface chemistry, on the micron scale, is well-established as a method to direct the nucleation and growth of various crystalline inorganic materials.[26,27] For example, self-assembled monolayers (SAMs) patterned on metal substrates can control the location, number, and crystallographic orientation of calcite ($CaCO_3$) crystals grown on the surface.[28–32] Moving beyond calcite and SAMs, the nucleation and growth of various metals,[33–35] metal oxides,[35] and metal sulfides[36] have been controlled by directly writing a block copolymer, poly(ethylene oxide)-*b*-poly(2-vinylpyridine), into a desired pattern. The pendant pyridine groups are proposed to coordinates to metal ions and direct the location of nucleation and growth. In all direct writing cases, high pressures (850-1000 Torr) or temperatures (500°C) were necessary, however, in order to crystallize the respective inorganic.

Moving to the nanoscale, numerous block copolymers (BCPs) have been used to chemically pattern surfaces on the 10s of nm length scale but few studies have looked into templating the nucleation and growth of crystalline inorganics. Poly(styrene)-*b*-poly(acrylic acid) was the first BCP to template the nanopatterned nucleation and growth of inorganic materials in the form of CdS, ZnS, and PbS.[37] Later, poly(styrene)-*b*-poly(2-vinylpyridine) was used to template the nucleation and growth of molybdenum sulfide, but required high temperatures for crystallization (up to 700 °C) causing the underlying organic material to desintegrate.[38] In both cases the

nucleating surface functional group remained the same, and no mechanism was proposed of how the respective crystalline inorganic phase nucleated and grew on the nanopatterned template surface. While previous work on homogeneous and micron-scale patterned surfaces helped to understand mechanisms of how various functional groups control nucleation and subsequent growth of inorganic crystals, comparable efforts on nanostructured surfaces are limited. Our work therefore strives to increase the fundamental understanding of how the combination of surface chemistry and nanoscale confinement affects the heterogenous nucleation and growth of inorganic crystal phases.

Here, we use our previously introduced *inorganic surface templating on assembled mesostructured polymers*, or simply iSTAMP, method to investigate the role of surface chemistry, surface charge and solution pH, degree of confinement, and topology to gain further insights into templating the nucleation and growth of transition metal oxide crystals. Our previous work demonstrated that thiol-ene "click" chemistry can be used to covalently small molecule thiols, e.g., cysteine, to the pendant alkene groups in the hydrophilic block of a BCP, polystyrene-*block*-poly[(allyl glycidyl ether)-*co*-(ethylene oxide)] (PS-*b*-P(AGE-*co*-EO)).[39,40] We observed that the thin film topology created by spin coating and subsequent solvent vapor annealing of PS-*b*-P(AGE-*co*-EO) on a silicon wafer consisted of cylindrical P(AGE-*co*-EO) wells of about 8 nm depth within a PS matrix. The BCP thin film surface with nanoscopically confined Cys surface chemical functionality was then used to template the hydrothermal nucleation and growth of crystalline copper (I) oxide (Cu_2O) and zinc oxide (ZnO). These initial results lead us to ask further questions: How does the topology of the template change during the initial inorganic nucleation? What is the relationship between the topology and location of the initial inorganic nucleation? How does the initial nucleation site affect the final inorganic

crystal? Therefore, we were inspired to manipulate the template topology and chemistry to explore their combined effects on crystallization.

4.3 Results

The iSTAMP method provides a large experimental space in which to explore a range of different chemical surface functionalities and substrate mesostructures. In this work, we varied the surface chemistry by using several different thiols to functionalize the hexagonally packed standing up P(AGE-*co*-EO) cylinders in the thin film BCP templates. We employed mesostructured BCP template, **iSTAMP0**, with a molar mass of 75.6 kg/mol, polydispersity index of 1.11, and volume fractions of 0.76 for PS and 0.24 for the P(AGE-*co*-EO) polyether block,[40] and varied the small molecule that was attached to the P(AGE-*co*-EO) block. In addition to Cys (**iSTAMPR$_1$**)[40], we used 3-mercaptopropionic acid (**iSTAMPR$_2$**), cysteamine (**iSTAMPR$_3$**), or 2-mercaptoethanol (**iSTAMPR$_4$**) to modify the chemistry of the hydrophilic domains from zwitterionic (mixed carboxylate and amine), to anionic (carboxylate), cationic (amine), or neutral (hydroxyl), respectively (Scheme 4.1). For the inorganic component, we initially focused on growth of ZnO using vapor diffusion of hydrazine (see reaction Scheme 4.1).

$$Zn(NO_3)_{2(aq)} \xrightarrow{N_2H_{4(v)},\ 60^oC,\ 1hr\ or\ 6hrs} ZnO \qquad (1)$$

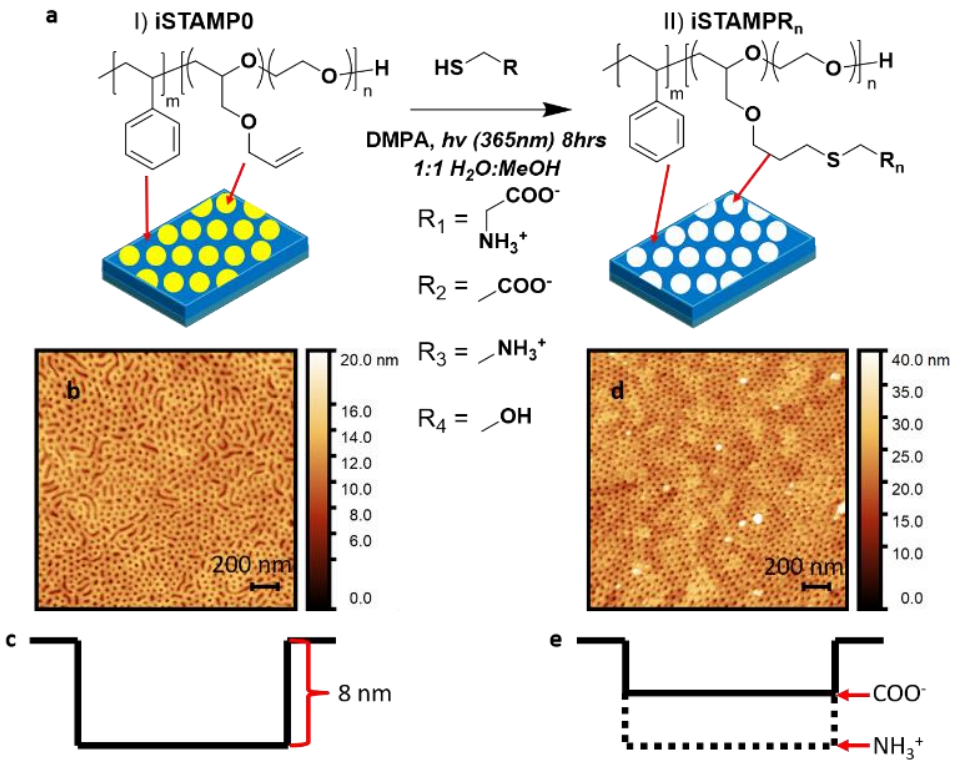

Scheme 4.1: a) Thin film thiol-ene chemistry with various functional groups. b,d) Representative AFM height images of **iSTAMP0** (b) and swollen **iSTAMPR$_n$** (d). c,e) Schematics derived from AFM experiments of height profiles of an **iSTAMP0** cylinder (c) and an **iSTAMPR$_n$** cylinder as a function of chemistry (e).

After functionalization of the BCP templates using thiol-ene click chemistry (Scheme 4.1), we used AFM to characterize the templates before ZnO growth, after 1 hr of ZnO growth, and after 6 hrs of ZnO growth (Figure 4.1). As previously reported, the hexagonally packed cylinder mesostructure as well as the substrate topology were preserved after functionalization.[39,40] For example, the carboxylate-functionalized template, **iSTAMPR$_2$**, had an average cylinder depth of about 8.0 nm ± 1 nm (n = 20 cylinders), approximately the same depth as cylinders in **iSTAMP0** (Fig. 4.1a).[40] To examine the effects of an aqueous, acidic solution with metal cations on the template topology, we incubated the templates in zinc nitrate solution at pH 3 at 60°C for 1 hour (i.e., without introducing hydrazine vapor necessary for inorganic material

growth, see Methods Section for more details) and directly analyzed the resulting AFM height profiles without dehydration (Scheme 4.1, Fig. 4.1a, Figure A3.1, Table A3.1). Both **iSTAMPR$_1$** and **iSTAMPR$_2$** showed a significant change in cylinder well depth upon incubation in this solution, with the average depth reduced to 3.4 nm and 3.8 nm, respectively. In contrast, both **iSTAMPR$_3$** and **iSTAMPR$_4$** did not swell significantly, with average depths of 7.5 nm, comparable to the dry substrates.

After 1 hr of exposure to growth solution with diffusing hydrazine vapor, the pH of the solution increased to pH=5. At this time point (1 hr), **ZnO-iSTAMPR$_2$** had an average cylinder depth of 9.7 nm ± 2 nm and an enhanced phase contrast between the two blocks, as compared to the dried **iSTAMPR$_2$** (Fig. 4.1b,g,h). This increase in height and phase contrast between **iSTAMPR$_2$** and **ZnO-iSTAMPR$_2$** after 1 hr of growth suggested that the inorganic nucleated at the top of the interface between the PS block and the functionalized P(EO-co-AGE) block.

After 6 hours of growth, the pH of the growth solution further increased to pH=11. AFM imaging revealed that the topology of the **ZnO-iSTAMPR$_2$** after 6 hrs of growth changes such that the minority block cylinders are now protruding from the surface, with an average cylinder height of 2.1 nm ± 4.4 nm. This change in height, coupled with an enhanced phase contrast compared to **iSTAMPR$_2$** before inorganic growth, indicates that the inorganic had grown on average approximately 2 nm above the top of the well (Fig. 4.1c,i).

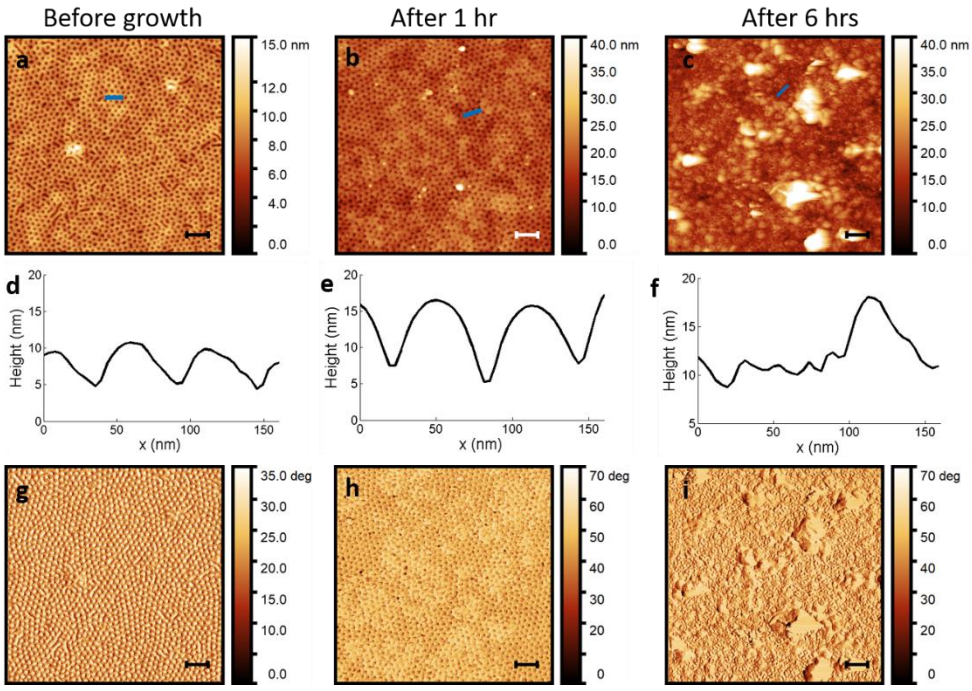

Figure 4.1: Representative AFM height (a-c) and phase images (g-i) of (a,g) dried **iSTAMPR$_2$**, (b,h) **ZnO-iSTAMPR$_2$** after 1 hr of growth, and (c,i) **ZnO-iSTAMPR$_2$** after 6 hrs of growth, with (d,e,f) corresponding line profiles from 3 cylinders represented by a blue line in corresponding AFM height profiles (a,b,c).

AFM was also used to characterize **ZnO-iSTAMPR$_1$**, **ZnO-iSTAMPR$_3$**, and **ZnO-iSTAMPR$_4$** after 6 hours to determine the average amount of inorganic material grown within the cylinder nanowells as a function of surface chemistry (Table 4.1). For all samples, it was assumed that the inorganic has grown such that the wells are completely filled in by inorganic (Scheme 4.2). AFM scans could also identify larger crystals that were not confined within the BCP template, but rather overgrew on the surface of the template (Figure 4.1c, Figure A3.2, and Table 4.1).

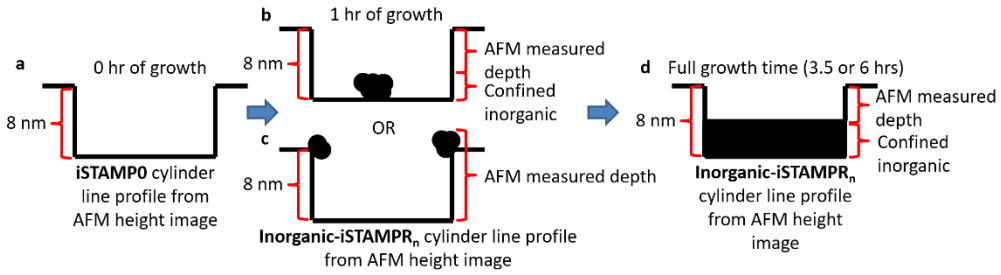

Scheme 4.2: Calculation of amount of confined inorganic from AFM height profile line cut across BCP cylinder

Table 4.1: AFM Height Profile Analysis Summary of Amounts of Confined Inorganic and Inorganic Overgrowth

	Functional Group	Growth Time (hrs)	Average Confined Inorganic (nm)	Standard Deviation (nm)	Inorganic Overgrowth Range (nm)
ZnO-iSTAMPR$_1$*	COO^- & NH_3^+	6	4.6	2.0	N/A
ZnO-iSTAMPR$_2$	COO^-	6	10.1	4.4	30-50
ZnO-iSTAMPR$_3$	NH_3^+	6	6.4	3.0	N/A
ZnO-iSTAMPR$_4$	OH	6	4.3	2.5	N/A
Cu$_2$O-iSTAMPR$_1$*	COO^- & NH_3^+	1.5	2.4	1.7	N/A
Cu$_2$O-iSTAMPR$_1$	COO^- & NH_3^+	3.5	7.3	4.8	120-290
Cu$_2$O-iSTAMPR$_2$	COO^-	3.5	7.7	5.4	N/A
Cu$_2$O-iSTAMPR$_3$	NH_3^+	3.5	4.4	3.7	10-30
Cu$_2$O-iSTAMPR$_4$	OH	3.5	5.4	2.6	N/A

*data previously reported[40]

Based upon this analysis of the 6 hour growth time point, the most amount of "confined inorganic" grew on **ZnO-iSTAMPR$_2$**, followed by **ZnO-iSTAMPR$_3$**, **ZnO-iSTAMPR$_1$,** and **ZnO-iSTAMPR$_4$** (Table 4.1). **ZnO-iSTAMP$_2$** was the only template exhibiting multiple areas of substantial inorganic material overgrowths, 30 and 50 nm in size, visible within the scan area.

To obtain further insight into the differences between early (1 hr) and late (6 hr) stages of inorganic growth, we employed TEM on unstained samples to visualize the location and morphology of the deposited ZnO. We compared the initially deposited ZnO after 1 hr of growth to the later stages of growth, after 6 hrs, for **iSTAMPR$_2$**, **iSTAMPR$_3$**, and **iSTAMPR$_4$** (Figures 4.2, A3.3, A3.4).

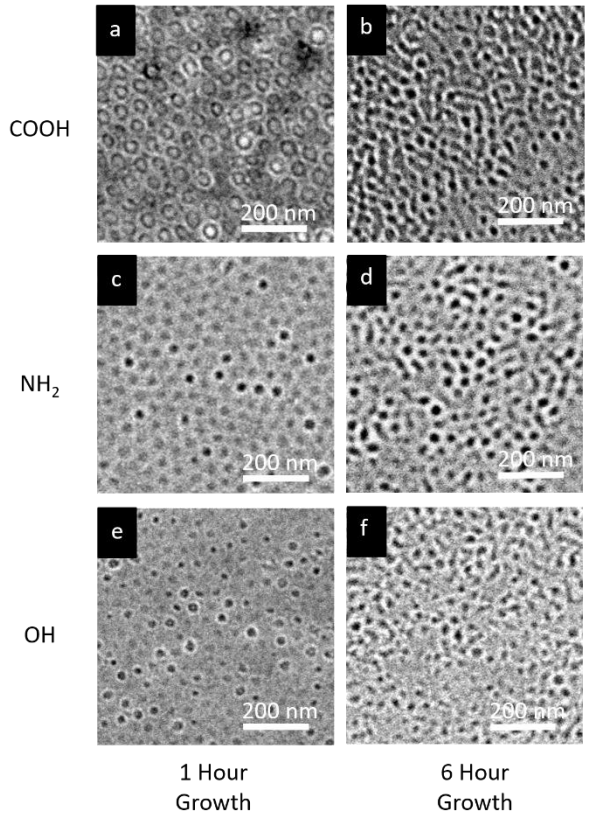

Figure 4.2: Brightfield TEM images of unstained samples after 1 hr and 6 hrs of growth, respectively, of (a,b) **ZnO-iSTAMPR$_2$**, (c,d) **ZnO-iSTAMPR$_3$**, and (e,f) **ZnO-iSTAMPR$_4$**

Interestingly, the different surface chemistries showed different morphologies of the deposited inorganic material. On the **ZnO-iSTAMPR$_2$** surface, after 1 hr of growth, darker ring structures were seen in a hexagonally-packed arrangement (Fig. 4.2a). These ring structures suggest that the increase in well depth observed by AFM (Fig. 4.1b) is the result of the deposition of ZnO at the interface of the PS and the functionalized P(EO-co-AGE) block, i.e. at the top of the edges of the cylinder wells as shown in Scheme 4.2. In contrast, for **ZnO-iSTAMPR$_2$**, and **ZnO-iSTAMPR$_4$**, the inorganic appeared as hexagonally arranged "dots", suggesting that the initial deposition occurs near the center of the functionalized P(EO-co-AGE) block (Figure 4.2c,e). TEM defocus image series were taken on both the "rings" and the "dots" and it was found that the "rings" remained visible throughout the defocus series in the TEM images, unlike the "dots" (Figures A3.3 and A3.4), verifying that the ring geometry was not an imaging artifact.

After 6 hrs of growth, all brightfield TEM images of ZnO grown on **iSTAMPR$_2$**, **iSTAMPR$_3$**, or **iSTAMPR$_4$** exhibited darker regions associated with the minority domains of the BCP template (Fig. 4.2b,d,f). Because these samples were unstained, these darker regions imply that there is more of the respective inorganic in these areas, indicating the inorganic was confined to the functionalized minority block. Qualitatively based upon visual inspection of TEM contrast, **ZnO-iSTAMPR$_2$** had the most deposited inorganic followed by **ZnO-iSTAMPR$_3$** and **ZnO-iSTAMPR$_4$** (Figures 4.2 and A3.5).

In order to further probe the crystal structures of the surface functionalized BCP thin films as well as the nanostructured inorganic materials deposited on these BCP thin films, samples were prepared from the same films as Figure 4.1 and characterized using a combination of grazing-incidence wide-angle x-ray scattering

(GIWAXS), powder x-ray diffraction (pXRD), and grazing-incidence small-angle x-ray scattering (GIWAXS) (Figure 4.3 and Table A3.2, Figures A3.6-A3.7). From pXRD on 6 hr films, we confirmed that the ZnO deposited on the templates had a wurtzite structure, characteristic of the mineral zincite (Fig. A3.7).

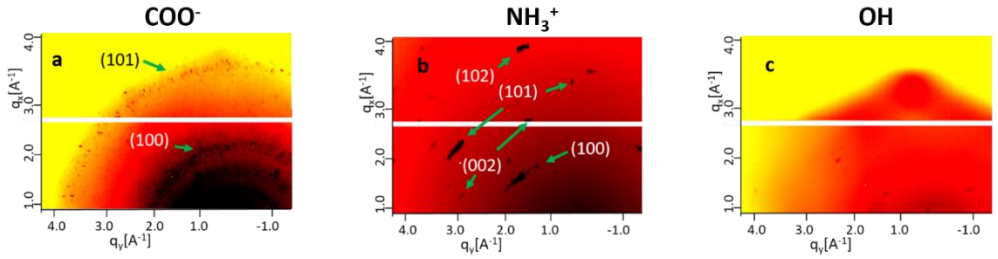

Figure 4.3: GIWAXS patterns of (a) **ZnO-iSTAMPR$_2$**, (b) **ZnO-iSTAMPR$_3$**, and (c) **ZnO-iSTAMPR$_4$** (JCPDS No. 36-1451) after 6 hrs of growth.

Simultaneous GISAXS and GIWAXS experiments were performed on the films after 6 hrs of growth to investigate the crystallinity of the inorganic as well as the BCP mesostructure over a larger area than that probed locally by TEM and AFM. All GISAXS measurements demonstrated a standing up hexagonally packed cylinder structure with a *d* spacing of 45 nm and a cylinder-cylinder distance of 52 nm, consistent with previous work (Table A3.2).[40]

GIWAXS patterns were analyzed to determine the effect of the surface chemistry on the crystallographic orientation of the zincite wurtzite crystals, both perpendicular to the substrate (i.e., growth direction) and within the plane (texture). The two-dimensional (2D) scattering pattern for **ZnO-iSTAMPR$_2$** showed continuous rings of individual (100) and (101) reflections (Fig. 4.3a), suggesting that the confined inorganic is crystallographically isotropically oriented and untextured within the plane of the substrate. Changing the functional group from COO^- to NH_3^+, the 2D-GIWAXS pattern of **ZnO-iSTAMPR$_3$** showed strongly textured arcs for (100), (002), (101), and (102) reflections (Fig. 4.3b), suggesting that the confined inorganic seen in the AFM

and TEM is textured. The peak width along the q-axis of the (100) reflections in the GIWAXS patterns of both **ZnO-iSTAMPR$_2$** and **ZnO-iSTAMPR$_3$** are approximately the same, around 0.05 Å^{-1}. Using the Scherrer equation, the calculated crystal sizes were approximately 15 nm, which is consistent with the particle sizes measured in TEM (~18 nm, N = 40). Therefore, the diffraction signal from both samples come from crystals of similar sizes, strongly suggesting that the ZnO hexagonally arranged inorganic nanostructures observed by TEM are responsible for the observed patterns, rather than larger, unpatterned crystals (Figure A3.6, Table A3.2). Finally, when changing the functionality to an OH group, the GIWAXS pattern of **ZnO-iSTAMPR$_4$** did not exhibit any spots or rings, suggesting that the confined inorganic visualized in the TEM images is amorphous (Figure 4.2e,f). When comparing the pXRD patterns of these samples, the relative ZnO peak heights change, which is also consistent with a change in the respective ZnO crystallographic orientation as a function of template surface chemistry (Figure A3.7).

Having seen a strong effect of surface chemistry on the nucleation and growth of ZnO using **iSTAMP**, we sought to extend the application of this technique to other oxides, in particular, Cu_2O. Towards this end, Cu_2O was grown on **iSTAMPR$_2$**, **iSTAMPR$_3$**, and **iSTAMPR$_4$** (see reaction Scheme 4.2). In contrast to the ZnO growth, the pH of this growth solution remains strongly basic (pH = 13) throughout the entire growth period:

$$CuSO_{4(aq)} + Na_3C_6H_5O_7 + NaOH \xrightarrow{N_2H_{4(v)},\ 55^oC,\ 3.5hrs} Cu_2O \qquad (2)$$

Similar to ZnO growth experiments, AFM height and phase images indicated that inorganic material was deposited on the iSTAMP substrates selectively on the functionalized cylinders. AFM height profile analysis (Figures A3.2 and A3.8) revealed that **iSTAMPR$_1$** and **iSTAMPR$_2$** grew the most confined inorganic after 3.5

hours of growth, followed by **iSTAMPR$_4$**, and **iSTAMPR$_3$** (Table 4.1). We previously reported that after 1.5 hours of growth, **Cu$_2$O-iSTAMPR$_1$** had an average confined inorganic of 2.4 nm ± 1.7 nm.[40] When extending the growth to 3.5 hours the average confined inorganic increased to 7.3 nm ± 4.8 nm, and samples showed a large overgrowths ranging in size between 120 and 290 nm (Table 4.1 and Figure A3.8). Sample **Cu$_2$O-iSTAMPR$_2$** showed similar height values for the confined inorganic, but without overgrowth. Samples **Cu$_2$O-iSTAMPR$_3$** and **Cu$_2$O-iSTAMPR$_4$** showed smaller height values (around 4 and 5 nm, respectively), with detectable overgrowths with sizes ranging between 10 and 30 nm for the former, and no detectable overgrowth for the latter (Table 4.1).

After AFM experiments suggested that Cu_2O was successfully grown on the **iSTAMP$_n$** templates, we further characterized **Cu$_2$O-iSTAMPR$_2$**, **Cu$_2$O-iSTAMPR$_3$**, and **Cu$_2$O-iSTAMPR$_4$** samples with TEM, GIWAXS, pXRD, and GISAXS (Figures 4.4, A3.9 and Table A3.2).

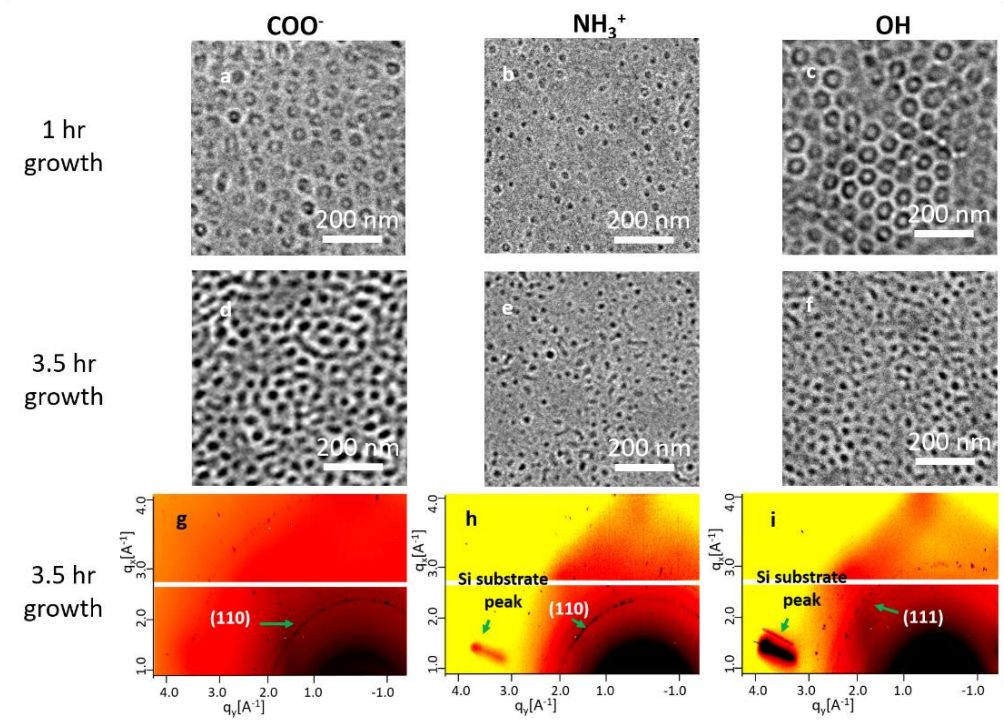

Figure 4.4: Brightfield TEM images of unstained samples after 1 hr (a,b,c) and 3.5 hrs (d,e,f) of inorganic growth, respectively, and corresponding 3.5 hr growth GIWAXS patterns of (a,d,g) **Cu_2O-iSTAMPR$_2$**, (b,e,h) **Cu_2O-iSTAMPR$_3$**, and (c,f,i) **Cu_2O-iSTAMPR$_4$** (JCPDS No. 05-0667).

First, we used TEM to observe the early (1 hr) stages of Cu_2O deposition on **iSTAMPR$_2$**, **iSTAMPR$_3$**, or **iSTAMPR$_4$**. As in the ZnO case, the initial inorganic growth after 1 hr on **iSTAMPR$_2$** occurred mostly at the interface, forming rings of inorganic, while the initial inorganic growth on **iSTAMPR$_3$** occurred mostly in the center of the functionalized cylinders, forming dots. **iSTAMPR$_4$**, on the other hand, formed rings of inorganic at the interface between the two blocks when Cu_2O was grown for 1 hr. All brightfield TEM images of Cu_2O grown on **iSTAMPR$_2$**, **iSTAMPR$_3$**, or **iSTAMPR$_4$** after 3.5 hrs showed darker regions associated with the minority domains of the BCP template, similar to the ZnO growths after 6 hrs (compare with Figure 4.2). In addition, the amount of inorganic as qualitatively visualized by the electron density contrast in TEM in Figures 4.4d-f and A3.9 is the most for **iSTAMPR$_2$**, followed by **iSTAMPR$_4$** and **iSTAMPR$_3$**, consistent with the

corresponding AFM image analysis (Figure A3.2, A3.8, and Table 4.1).

While TEM experiments demonstrated locally that the templated inorganic was mesostructured, GIWAXS and GISAXS experiments were performed to determine on a macroscopic scale whether the copper oxide phase was both mesostructured and crystalline (Figure 4.4, bottom). First, based upon pXRD, the crystalline phase of the inorganic material was determined to be the cubic Cu_2O cuprite structure (Fig. A3.10). GISAXS measurements summarized in Table A3.2 of sample films with Cu_2O growth on these templates corroborated the hexagonally packed standing up cylinder morphology and *d* spacing of the template without any inorganic, just like in the case of ZnO growths. The GIWAXS patterns were analyzed to see how the patterned surface chemistry and topology of the template controls the crystal orientation and texturing of the cubic-phase crystal structure of cuprite. The **Cu_2O-iSTAMPR$_2$** pattern showed a predominant (110) ring of reflections, suggesting that the nucleation occurred on the (110) plane, with no in-plane texturing (Figure 4.4g). When changing the functional group to NH_3^+, the GIWAXS of **Cu_2O-iSTAMPR$_3$** showed a higher intensity arc along the (110) ring at lower azimuthal angles, suggesting that the confined inorganic seen in the AFM and TEM might be weakly textured (Figure 4.4h). Finally, when changing the functionality to an OH group, the GIWAXS of **Cu_2O-iSTAMPR$_4$** showed a predominant (111) ring of reflections, suggesting that the nucleation occurred on the (111) plane, with no detectable in-plane texturing (Figure 4.4i). The change in crystallographic orientation as a function of surface chemistry is also evident when comparing the relative peak intensities of the respective pXRD patterns (Figure A3.10).

4.4 Discussion

We have presented data describing the combined influence of surface

chemistry and surface topology on the nucleation and growth of zinc and copper oxides on BCP thin film templates. To map the process of nucleation and growth, we observed the system at three time points: 1) pre-nucleation (template incubated in zinc nitrate solution without introduction of hydrazine), 2) early stage of growth at around 1 hour, and 3) later stage of growth at around 6 hours, before significant overgrowth of the pattern occurred.

After incubation of the templates in the zinc nitrate growth solution without hydrazine vapor, two of the templates (**iSTAMPR$_1$** and **iSTAMP$_2$**) had significant topology change, while the other two (**iSTAMPR$_3$** and **iSTAMP$_4$**) did not. These changes in the cylinder well height of are difficult to interpret, as there are multiple factors that could be causing the various functionalized templates to swell. The temperature at which the inorganic growth took place (60 °C) was below PS's glass transition temperature [T_g(PS) = 100 °C], but higher than P(EO-co-AGE)'s T_g [P(EO-co-AGE) = -80 °C].[41] Therefore, the PS block was in a glassy state, while the P(EO-co-AGE) block was mobile within its domain, implying that the height differences in the swelling study were mainly due to changes in the P(EO-co-AGE) functionalized blocks. A few potential contributions to these changes include the distribution and density of functional groups on the polymer template surface as well as deeper into the hydrophilic domains, which is related to the penetration of the small thiol molecules during the thiol-ene reaction, which may vary from R-group to R-group. The different functional groups will also chelate Zn^{2+} ions to different amounts (e.g., COO^- will readily chelate metal ions while NH_3^+ will not). All of these effects will change the electrostatics of the polymer chain interactions, which in turn will change the degree of swelling of the P(EO-co-AGE) functionalized blocks. All of these variables are difficult to separate between different film chemistries and will therefore not be further discussed. Instead, to gain mechanistic insights on how inorganic crystals grow

on different surface chemical functionalities that are nanoscopically confined, we will focus the discussion on AFM, TEM, and GIWAXS characterization results.

Combining GIWAXS results with the initial growth visualization via TEM (at 1 hr), we find a correlation between crystallographic texturing and the location of the initial inorganic ZnO growth. When the inorganic growth starts at the interface between hydrophobic PS and hydrophilic P(EO-co-AGE) blocks on top of the rim of the cylinder wells (i.e., rings observed in TEM and an increase in well depth observed by AFM), the resulting ZnO crystals have no preferred crystallographic orientation (i.e., continuous rings in the GIWAXS patterns). We can rationalize this correlation intuitively, because it is likely that there are multiple nucleation events around the rim of the functionalized hexagonal cylindrical well, leading to randomly oriented ZnO crystals. On the other hand, when ZnO growth starts in the center of the functionalized hexagonal cylindrical well (i.e., dots observed in TEM) the resulting ZnO crystals have a preferred orientation (i.e., arcs in the GIWAXS patterns). We hypothesize that this crystallographic texturing is due to role of nanoconfinement in limiting the number of nucleation events to one per functionalized cylinder, coupled with a preferred growth direction imposed by the confinement of the cylindrical well.

When interpreting the crystallization results it is important to consider the change in pH of the growth solution over time. For the ZnO growth, the solution begins at acidic pH, starting at pH 3 and rising to pH 5 after one hour, at which point inorganic has already begun to grow. By 1 hr, the carboxylic acid groups on both **iSTAMPR$_1$** and **iSTAMPR$_2$** will be deprotonated and negatively charged. These negatively charged $–COO^-$ moieties can chelate Zn^{2+} ions from solution thereby locally increasing supersaturation and promoting ZnO nucleation. The untextured GIWAXS patterns from **iSTAMPR$_2$** after 6 hours of growth suggest that strong chelation to Zn^{2+} leads to isotropic crystallization rather than preferential nucleation of

any unique plane of ZnO. In contrast, at pH 5, the amine groups on **iSTAMPR$_3$** will be protonated, resulting in a substrate with positively charged cylinders. On this substrate, according to the GIWAXS patterns, the ZnO crystals are highly textured. While the positively charged NH_3^+ groups will not interact strongly with Zn^{2+} ions, it is possible these functional groups can bind to and stabilize ZnO clusters formed in solution. This model is consistent with reports in the literature of cationic organic groups preferentially binding to the (001) planes of ZnO,[42,43] and offers an explanation for the observed texturing in the GIWAXS patterns. Finally, the loss of crystallinity of ZnO when switching to the neutral hydroxyl functional group (**iSTAMPR$_4$**) suggests that there is not a strong interaction between the –OH group and either Zn^{2+} or ZnO, again consistent with literature.

We can also draw some conclusions from the results of Cu_2O growths onto the four different functionalized templates. Unlike the zinc nitrate growth solution, which changes in pH as more hydrazine is introduced, the pH of the Cu_2O growth solution is consistently around pH 13. Because of the constant basic pH, most -COOH groups are deprotonated and most NH_2 groups are neutral, leading to highly negatively charged but weakly positively charged surfaces, respectively. We therefore would expect that in particular for the templates with amine groups the effects are not as pronounced as for the ZnO growth, consistent with our observation, (compare GIWAXS patterns of Figures 4.3 and 4.4). Template surfaces with $–COO^-$ groups (**iSTAMPR$_1$** and **iSTAMPR$_2$**) chelate Cu^+/Cu^{2+} ions from solution, locally increasing supersaturation and promoting nucleation of Cu_2O. On the other hand, based on known interactions between amine and hydroxyl functional groups and Cu_2O we anticipate Cu_2O clusters to form in solution before chelating to these functional groups in **iSTAMPR$_3$** and **iSTAMPR$_4$**.[44–46] We only observed very weakly textured Cu_2O when templated from **iSTAMPR$_3$**, consistent with a slight preferential binding

orientation of Cu_2O clusters to the amine groups.[47,48,51,52]

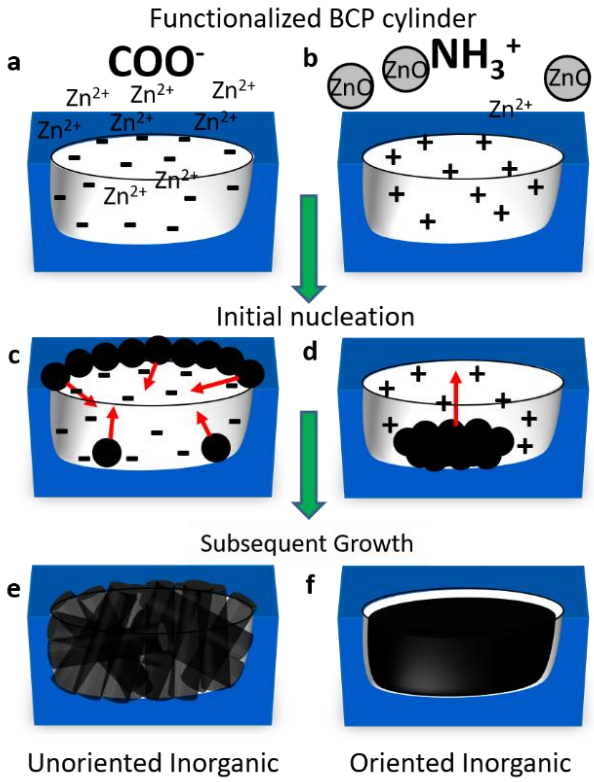

Scheme 4.3: Proposed growth pathways dependent on the surface charge of **iSTAMPR$_n$** surfaces.

Based upon our combined observations of the ZnO and Cu_2O growth on the **iSTAMPR$_n$** templates, we propose two different growth pathways, dependent on the surface charge within the hydrophilic domains. For the case of zinc oxide, our proposed growth pathways are summarized in Scheme 4.3. When P(EO-co-AGE) is functionalized with $–COO^-$ groups, the negative charges chelate Zn^{2+} ions through electrostatic interactions, locally increasing the supersaturation in the vicinity of the cylindrical wells. In addition to this local increase in supersaturation, the energy barrier for heterogeneous nucleation is predicted to be lowest at the interface between the hydrophilic, negatively charged cylinder forming block and the hydrophobic PS

matrix.[49–51] These factors combine to favor nucleation of the ZnO at the interface between these two blocks situated at the rim of the cylindrical wells formed by the P(EO-co-AGE) block (Scheme 4.3c). In contrast, for the template functionalized with NH_3^+ groups, the positive charges repel Zn^{2+} ions via electrostatic interactions. In the absence of a good nucleating substrate, small ZnO clusters begin to form in solution (shown in grey in Scheme 4.3b).[52] These clusters are subsequently stabilized by interactions with the protonated amines of the cylinder forming P(EO-co-AGE) blocks.

After the initial nucleation, the template topology and chemistry continue to direct the growth. For the substrates with carboxylate-functionalized P(EO-co-AGE) blocks, it is likely that there are multiple nucleation events around the top of cylindrical well. Therefore, the subsequent growth will have various different growth directions, most likely all towards the inside of the cylinder well, where the hydrophilic P(EO-co-AGE) block resides, and away from the hydrophobic PS block (see Scheme 4.3e). Because of the circular symmetry, coupled with multiple growth directions, the final crystalline inorganic as examined by GIWAXS over a macroscopic area is isotropic. The proposed growth pathway is consistent with both **ZnO-iSTAMPR$_2$** and **Cu$_2$O-iSTAMPR$_2$** inorganic being untextured. When changing to a hydrophilic P(EO-co-AGE) block functionalized with -NH_3^+ groups, most likely the inorganic initially nucleates in the center of the cylinder well, where nanoconfinement effects are maximized,[1,9] and then grows upward with a common growth direction for all cylinder wells (see Scheme 4.3d). This explanation is consistent with the most textured GIWAXS results for sample **ZnO-iSTAMPR$_3$** and is likely also responsible for the weakly textured results for sample **Cu$_2$O-iSTAMPR$_3$**.

4.5 Conclusion

A variety of surface functional groups were attached via click chemistry to the

nanoscopic hydrophilic domains of an amphiphilic BCP thin film template to study the combined effects of nanoconfinement and chemical functionality on the low temperature crystallization of two transition metal oxides. The inorganic growth pathways of Cu_2O and ZnO on negatively charged, positively charged, and neutral surfaces were explored via materials characterization at different time points of growth to gain mechanistic insights into the roles of surface chemistry and topology in determining how inorganic crystals grow in nanoconfinement. Results suggest that the interplay between supersaturation, crystal surface stabilization, and nanoconfinement determine textured versus untextured crystal growth. Elucidated crystal growth pathways are expected to provide advanced low temperature routes to nanostructured crystalline inorganic materials and composites with applications in energy storage and conversion and catalysis.

4.6 Experimental Methods

Materials

Allyl glycidyl ether was purchased from TCI America. Deionized (DI) water was generated using a Millipore Milli-Q system. <100> silicon wafers were purchased from WRS Materials. Monolithic silicon non-contact high resonance frequency AFM tips with a force constant between 21–78 N/m were purchased from NanoWorld. All other chemicals were purchased from Sigma-Aldrich and used as received unless otherwise noted.

Polymer Synthesis and Characterization

PS-*b*-P(AGE-*co*-EO) was synthesized by anionic polymerization as previously reported. [39,40]

Polymer Thin Film Assembly and Surface Functionalization by Thiol-ene Chemistry

PS-*b*-P(AGE-*co*-EO) thin films were synthesized and characterized as previously reported.[39,40] The functionalization of the PS-*b*-P(AGE-*co*-EO) thin films was adopted

from previous work.[39] 2,2-dimethoxy-2-phenylacetophenone (DMPA) and the respective small molecule (cysteine, 3-mercaptopropionic acid, cysteamine hydrochloride, or 2-mercaptoethanol) were added to a 10 mL 1:1 (v:v) water-methanol mixture to achieve a solution concentration of 0.05 mM DMPA and 0.1 M of the respective small molecule. The resulting solution was covered with aluminum foil and stirred vigorously for 20 minutes. Then the solvent-annealed BCP thin film was added to the solution, and the BCP film containing solution was sparged with nitrogen gas for 15 minutes to remove all oxygen. The reaction mixture, while gently agitated, was exposed to UV light using a Spectroline Model ENF-260C 6W lamp with a wavelength of 365 nm and allowed to run for 8 hours. The reacted film was then washed three times with DI water and methanol and allowed to dry in air.

Functionalized BCP Thin Film Swelling

Zinc nitrate solution (2 mL, 200 mM) was added to a 20 mL scintillation vial at pH 3. The respective BCP thin film template (either **iSTAMPR$_1$**, **iSTAMPR$_2$**, **iSTAMPR$_3$**, or **iSTAMPR$_4$**) was floated on top of the growth solution and was allowed to soak for 1 hour before incubation. The scintillation vial with the growth solution and surface was then placed on a 60°C hot plate for 1 hour to swell. After 1 hour the surface was removed and the solution on top of the surface was wicked off. The surface was then moved to an AFM for imaging and analysis.

Inorganic growth on BCP Thin Film Surface

Crystallization of Cu_2O was adopted from previous work.[40,53,22] While the growth solution and setup remained the same, the growth time was set to 1 hour to assess the early phases of nucleation and growth, and 3.5 hours to assess crystallinity, texturing, and orientation of the final crystal phase. Final composites in either case were rinsed twice with water and once with ethanol.

Crystallization of ZnO was also adopted from previous work,[40] using the same growth

conditions and set up, but the growth time was run for 1 hour to assess the early phases of nucleation and growth, and 6 hours to assess crystallinity, texturing, and orientation of the final crystal phase. The final composites in both cases were rinsed twice with water and once with ethanol.

Atomic Force Microscopy (AFM)

All images were collected in tapping mode in air on a Digital Instruments Multimode scanning probe microscope at a resolution of 512 by 512 pixels and at a scan rate of 1.2–1.0 Hz.

Transmission Electron Microscopy (TEM)

TEM samples were prepared as previously reported and were unstained.[40,54] Defocus experiments were performed by imaging the desired area from 0 µm of defocus and proceeding to image the same area at 10 µm increments of defocus both in positive and negative directions.

Powder X-ray Diffraction (pXRD)

Scintag Theta-Theta X-ray Diffractometer was used to collect all pXRD with a scan rate of 1 °/min, slit sizes for outcoming x-rays of 2 mm and 4 mm, and slit sizes for incoming x-rays of 1 mm and 0.5 mm.

Grazing Incidence Small-Angle X-ray Scattering (GISAXS) and Grazing Incidence Wide-Angle X-ray Scattering (GIWAXS)

GISAXS and GIWAXS patterns were obtained at the Cornell High Energy Synchrotron Source (CHESS) at station G1 with a typical beam energy of 9.78 keV and sample-to-detector distance of 1.7 meters for the GISAXS patterns and 0.7 meters for the GIWAXS patterns, as previously reported.[40] GISAXS and GIWAXS patterns were obtained with an x-ray beam size of 250 µm x 250 µm at an angle of 0.14°. Dectris Eiger 1M pixel array detector (PAD) recorded the GISAXS patterns, and Dectris Pilatus 100k PAD recorded the GIWAXS data sets. The measurements

illuminated the same surface because GISAXS and GIWAXS patterns were collected immediately after one another without moving the sample or incident beam. Collected patterns were analyzed using the Nika software package for Igor Pro.[55]

ACKNOLWEDGEMENTS

The U.S. Department of Energy, Office of Science, Basic Energy Sciences supported this work under Award No. DESC0010560. We thank the Cornell High Energy Synchrotron Source (CHESS) and the Cornell Center for Materials Research (CCMR) for use of their facilities, in particular the powder x-ray diffraction and electron microscopy facilities of CCMR. CCMR facilities are supported by the National Science Foundation under Award Number DMR- 1719875; CHESS is supported by the National Science Foundation and the National Institutes of Health/National Institute of General Medical Sciences under NSF award DMR-1332208. PAB was supported by the NSF Graduate Research Fellowship Program under DGE-1144153.

Appendix Information additional AFMs, GISAXS characterization, additional TEM images

4.7 References

(1) Whittaker, M. L.; Dove, P. M.; Joester, D. Nucleation on Surfaces and in Confinement. *MRS Bull.* **2016**, *41* (5), 388–392.

(2) Marsh, M. E. Coccolith Crystals of Pleurochrysis Carterae: Crystallographic Faces, Organization, and Development. *Protoplasma* **1999**, *207* (1–2), 54–66.

(3) Marsh, M. E.; Ridall, A. L.; Azadi, P.; Duke, P. J. Galacturonomannan and Golgi-Derived Membrane Linked to Growth and Shaping of Biogenic Calcite. *J. Struct. Biol.* **2002**, *139* (1), 39–45.

(4) Sone, E. D.; Weiner, S.; Addadi, L. Biomineralization of Limpet Teeth: A Cryo-TEM Study of the Organic Matrix and the Onset of Mineral Deposition. *J. Struct. Biol.* **2007**, *158* (3), 428–444.

(5) Scheffel, A.; Gruska, M.; Faivre, D.; Linaroudis, A.; Plitzko, J. M.; Schüler, D. An Acidic Protein Aligns Magnetosomes along a Filamentous Structure in Magnetotactic Bacteria. *Nature* **2006**, *440* (7080), 110–114.

(6) Abreu, F.; Sousa, A. A.; Aronova, M. A.; Kim, Y.; Cox, D.; Leapman, R. D.; Andrade, L. R.; Kachar, B.; Bazylinski, D. A.; Lins, U. Cryo-Electron Tomography of the Magnetotactic Vibrio Magnetovibrio Blakemorei: Insights into the Biomineralization of Prismatic Magnetosomes. *J. Struct. Biol.* **2013**, *181* (2), 162–168.

(7) Weiner, S.; Wagner, H. D. THE MATERIAL BONE: Structure-Mechanical Function Relations. *Annu. Rev. Mater. Sci.* **1998**, *28* (1), 271–298.

(8) Mahamid, J.; Sharir, A.; Gur, D.; Zelzer, E.; Addadi, L.; Weiner, S. Bone Mineralization Proceeds through Intracellular Calcium Phosphate Loaded Vesicles: A Cryo-Electron Microscopy Study. *J. Struct. Biol.* **2011**, *174* (3), 527–535.

(9) Jiang, Q.; Ward, M. D. Crystallization under Nanoscale Confinement. *Chem. Soc. Rev.* **2014**, *43* (7), 2066–2079.

(10) Rault, J.; Neffati, R.; Judeinstein, P. Melting of Ice in Porous Glass: Why Water and Solvents Confined in Small Pores Do Not Crystallize? *Eur. Phys. J. B* **2003**, *36* (4), 627–637.

(11) Unruh, K. M.; Huber, T. E.; Huber, C. A. Melting and Freezing Behavior of Indium Metal in Porous Glasses. *Phys. Rev. B* **1993**, *48* (12), 9021–9027.

(12) Jackson, C. L.; McKenna, G. B. Vitrification and Crystallization of Organic Liquids Confined to Nanoscale Pores. *Chem. Mater.* **1996**, *8* (8), 2128–2137.

(13) Alcoutlabi, M.; McKenna, G. B. Effects of Confinement on Material Behaviour at the Nanometre Size Scale. *J. Phys. Condens. Matter* **2005**, *17* (15).

(14) Hamilton, B. D.; Hillmyer, M. A.; Ward, M. D. Glycine Polymorphism in Nanoscale Crystallization Chambers. *Cryst. Growth Des.* **2008**, *8* (9), 3368–3375.

(15) Mann, S.; Hannington, J. P.; Williams, R. J. P. Phospholipid Vesicles as a Model System for Biomineralization. *Nature* **1986**, *324* (6097), 565–567.

(16) Collier, J. H.; Messersmith, P. B. Phospholipid Strategies in Biomineralization and Biomaterials Research. *Annu. Rev. Mater. Res.* **2001**, *31*, 237–263.

(17) Tester, C. C.; Whittaker, M. L.; Joester, D. Controlling Nucleation in Giant Liposomes. *Chem. Commun.* **2014**, *50* (42), 5619–5622.

(18) Wolf, S. E.; Müller, L.; Barrea, R.; Kampf, C. J.; Leiterer, J.; Panne, U.; Hoffmann, T.; Emmerling, F.; Tremel, W. Carbonate-Coordinated Metal Complexes Precede the Formation of Liquid Amorphous Mineral Emulsions of Divalent Metal Carbonates. *Nanoscale* **2011**, *3* (3), 1158.

(19) Stephens, C. J.; Ladden, S. F.; Meldrum, F. C.; Christenson, H. K. Amorphous Calcium Carbonate Is Stabilized in Confinement. *Adv. Funct. Mater.* **2010**, *20* (13), 2108–2115.

(20) Loste, E.; Park, R. J.; Warren, J.; Meldrum, F. C. Precipitation of Calcium Carbonate in Confinement. *Adv. Funct. Mater.* **2004**, *14* (12), 1211–1220.

(21) Wang, Y. W.; Christenson, H. K.; Meldrum, F. C. Confinement Increases the Lifetimes of Hydroxyapatite Precursors. *Chem. Mater.* **2014**, *26* (20), 5830–5838.

(22) Asenath-Smith, E.; Noble, J. M.; Hovden, R.; Uhl, A. M.; DiCorato, A.; Kim, Y.-Y.; Kulak, A. N.; Meldrum, F. C.; Kourkoutis, L. F.; Estroff, L. A. Physical Confinement Promoting Formation of Cu_2O–Au Heterostructures with Au

Nanoparticles Entrapped within Crystalline Cu_2O Nanorods. *Chem. Mater.* **2017**, *29* (2), 555–563.

(23) Schenk, A. S.; Albarracin, E. J.; Kim, Y.-Y.; Ihli, J.; Meldrum, F. C. Confinement Stabilises Single Crystal Vaterite Rods. *Chem. Commun.* **2014**, *50* (36), 4729.

(24) Cantaert, B.; Beniash, E.; Meldrum, F. C. Nanoscale Confinement Controls the Crystallization of Calcium Phosphate: Relevance to Bone Formation. *Chemistry* **2013**, *19* (44), 14918–14924.

(25) Wang, Y. W.; Christenson, H. K.; Meldrum, F. C. Confinement Leads to Control over Calcium Sulfate Polymorph. *Adv. Funct. Mater.* **2013**, *23* (45), 5615–5623.

(26) Aizenberg, J.; Black, A. J.; Whitesides, G. M. Oriented Growth of Calcite Controlled by Self-Assembled Monolayers of Functionalized Alkanethiols Supported on Gold and Silver. *J. Am. Chem. Soc.* **1999**, *121* (18), 4500–4509.

(27) Aizenberg, J.; Black, a J.; Whitesides, G. M. Control of Crystal Nucleation by Patterned Self-Assembled Monolayers. *Nature* **1999**, *398* (6727), 495–498.

(28) Addadi, L.; Moradian, J.; Shay, E.; Maroudas, N. G.; Weiner, S. A Chemical Model for the Cooperation of Sulfates and Carboxylates in Calcite Crystal Nucleation: Relevance to Biomineralization. *Proc. Natl. Acad. Sci. U. S. A.* **1987**, *84* (9), 2732–2736.

(29) Mann, S. Molecular Tectonics in Biomineralization and Biomimetic Materials Chemistry. *Nature* **1993**, *365*, 499–505.

(30) Mann, S.; Archibald, D. D.; Didymus, J. M.; Douglas, T.; Heywood, B. R.; Meldrum, F. C.; Reeves, N. J. Crystallization at Inorganic-Organic Interfaces: Biominerals and Biomimetic Synthesis. *Science (80-.).* **1993**, *261* (43), 1286–1292.

(31) Aizenberg, J. Crystallization in Patterns: A Bio-Inspired Approach. *Adv. Mater.* **2004**, *16* (15), 1295–1302.

(32) Aizenberg, J. Direct Fabrication of Large Micropatterned Single Crystals. *Science.* **2003**, *299* (5610), 1205–1208.

(33) Huang, L.; Braunschweig, A. B.; Shim, W.; Qin, L.; Lim, J. K.; Hurst, S. J.; Huo, F.; Xue, C.; Jang, J. W.; Mirkin, C. A. Matrix-Assisted Dip-Pen Nanolithography and Polymer Pen Lithography. *Small* **2010**, *6* (10), 1077–1081.

(34) Chai, J.; Huo, F.; Zheng, Z.; Giam, L. R.; Shim, W.; Mirkin, C. a. Scanning Probe Block Copolymer Lithography. *Proc. Natl. Acad. Sci. U. S. A.* **2010**, *107* (47), 20202–20206.

(35) Liu, G.; Eichelsdoerfer, D. J.; Rasin, B.; Zhou, Y.; Brown, K. A.; Liao, X.; Mirkin, C. A. Delineating the Pathways for the Site-Directed Synthesis of Individual Nanoparticles on Surfaces. *Proc. Natl. Acad. Sci. U. S. A.* **2013**, *110* (3), 887–891.

(36) Giam, L. R.; He, S.; Horwitz, N. E.; Eichelsdoerfer, D. J.; Chai, J.; Zheng, Z.; Kim, D.; Shim, W.; Mirkin, C. A. Positionally Defined, Binary Semiconductor Nanoparticles Synthesized by Scanning Probe Block Copolymer Lithography. *Nano Lett.* **2012**, *12* (2), 1022–1025.

(37) Morin, S. A.; La, Y. H.; Liu, C. C.; Streifer, J. A.; Hamers, R. J.; Nealey, P. F.; Jin, S. Assembly of Nanocrystal Arrays by Block-Copolymer-Directed Nucleation. *Angew. Chemie - Int. Ed.* **2009**, *48* (12), 2135–2139.

(38) Wei, W.; Samad, L.; Choi, J. W.; Joo, Y.; Way, A.; Arnold, M. S.; Jin, S.; Gopalan, P. Synthesis of Molybdenum Disulfide Nanowire Arrays Using a Block Copolymer Template. *Chem. Mater.* **2016**, *28* (11), 4017–4023.

(39) Oleske, K. W.; Barteau, K. P.; Turker, M. Z.; Beaucage, P. A.; Estroff, L. A.;

Wiesner, U. Block Copolymer Directed Nanostructured Surfaces as Templates for Confined Surface Reactions. *Macromolecules* **2017**, *50* (2), 542–549.

(40) Oleske, K. W.; Barteau, K. P.; Beaucage, P. A.; Asenath-Smith, E.; Wiesner, U.; Estroff, L. A. Nanopatterning of Crystalline Transition Metal Oxides by Surface Templated Nucleation on Block-Copolymer Mesostructures. *Cryst. Growth Des.* **2017**, *17* (11), 5775–5782.

(41) Dimitriou, M. D.; Zhou, Z.; Yoo, H.-S.; Killops, K. L.; Finlay, J. A.; Cone, G.; Sundaram, H. S.; Lynd, N. A.; Barteau, K. P.; Campos, L. M.; et al. A General Approach to Controlling the Surface Composition of Poly(ethylene Oxide)-Based Block Copolymers for Antifouling Coatings. *Langmuir* **2011**, *27* (22), 13762–13772.

(42) Tang, H.; Chang, J. C.; Shan, Y.; Lee, S. T. Surfactant-Assisted Alignment of ZnO Nanocrystals to Superstructures. *J. Phys. Chem. B* **2008**, *112* (13), 4016–4021.

(43) Moreira, N. H.; Domınguez, A.; Frauenheim, T.; da Rosa, A. L. On the Stabilization Mechanisms of Organic Functional Groups on ZnO Surfaces. *Phys. Chem. Chem. Phys.* **2012**, *14* (44), 15445–15451.

(44) Yao, K. X.; Yin, X. M.; Wang, T. H.; Zeng, H. C. Two Types of Cu2O Nanocrystals Unifaceted with {001} or {110} Planes. *J. Am. Chem. Soc.* **2010**, No. 14, 55–59.

(45) Onsten, A.; Weissenrieder, J.; Stoltz, D.; Yu, S.; Gothelid, M.; Karlsson, U. O. Role of Defects in Surface Chemistry on Cu2O (111). *J. Phys. Chem. C* **2013**, *117* (38), 19357–19364.

(46) Besharat, Z.; Halldin Stenlid, J.; Soldemo, M.; Marks, K.; Önsten, A.; Johnson, M.; Öström, H.; Weissenrieder, J.; Brinck, T.; Göthelid, M. Dehydrogenation of Methanol on Cu2O (100) and (111). *J. Chem. Phys.* **2017**, *146* (24), 1–8.

(47) Susman, M. D.; Feldman, Y.; Vaskevich, A.; Rubinstein, I. Chemical Deposition of Cu_2O Nanocrystals with Precise Morphology. *ACS Nano* **2014**, *8* (1), 162–174.

(48) Susman, M. D.; Feldman, Y.; Vaskevich, A.; Rubinstein, I. Chemical Deposition and Stabilization of Plasmonic Copper Nanoparticle Films on Transparent Substrates. *Chem. Mater.* **2012**, *24* (13), 2501–2508.

(49) Kisailus, D.; Truong, Q.; Amemiya, Y.; Weaver, J. C.; Morse, D. E. Self-Assembled Bifunctional Surface Mimics an Enzymatic and Templating Protein for the Synthesis of a Metal Oxide Semiconductor. *Proc. Natl. Acad. Sci.* **2006**, *103* (15), 5652–5657.

(50) Gómez, L. R.; García, N. a; Vitelli, V.; Lorenzana, J.; Vega, D. A. Phase Nucleation in Curved Space. *Nat. Commun.* **2015**, *6*, 6856.

(51) Schmelzer, J.; Gutzow, I.; Jr, J. S. Curvature-Dependent Surface Tension and Nucleation Theory. *J. Colloid Interface Sci.* **1996**, *665*, 657–665.

(52) Thanh, N. T. K.; Maclean, N.; Mahiddine, S. Mechanisms of Nucleation and Growth of Nanoparticles in Solution. *Chem. Rev.* **2014**, *114* (15), 7610–7630.

(53) DiCorato, A. E.; Asenath-Smith, E.; Kulak, A. N.; Meldrum, F. C.; Estroff, L. A. Cooperative Effects of Confinement and Surface Functionalization Enable the Formation of Au/Cu2O Metal–Semiconductor Heterostructures. *Cryst. Growth Des.* **2016**, *16* (12), 6804–6811.

(54) Kopp, S.; Wittmann, J. C.; Lotz, B. Epitaxial Crystallization and Crystalline Polymorphism of poly(1-Butene): Form I. *Polymer (Guildf).* **1994**, *35* (5), 916–924.

(55) Ilavsky, J. Nika: Software for Two-Dimensional Data Reduction. *J. Appl. Crystallogr.* **2012**, *45* (2), 324–328.

APPENDIX THREE

INTERPLAY OF SURFACE CHEMISTRY AND NANOCONFINEMENT IN DIRECTING CRYSTALLIZATION OF NANOSTRUCTURED TRANSITION METAL OXIDES

List of Appendix Information Tables and Figures

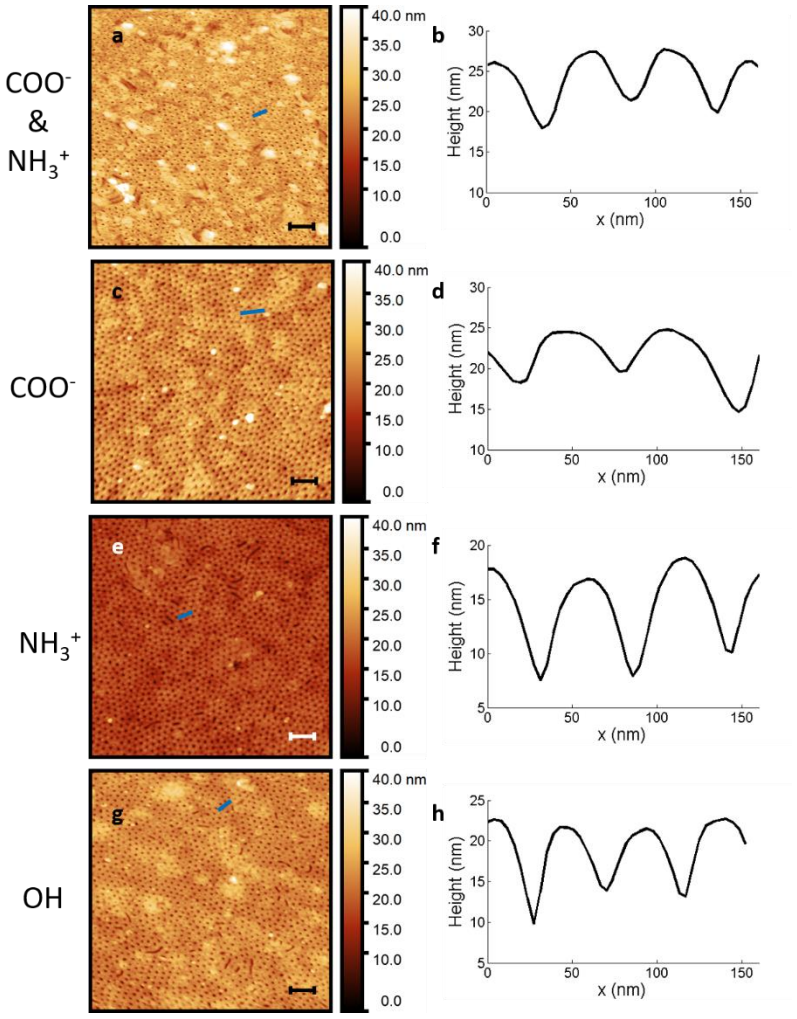

Figure A3.1: Representative AFM height profiles of (a) **iSTAMPR1**, (c) **iSTAMPR2**, (e) **iSTAMPR3**, (g) **iSTAMPR4**, (b,d,f,h) with representative line profiles of 3 cylinders marked in blue in the respective height image scale bars 200 nm

Table A3.1: Swelling AFM Height Profile Analysis Summary

	COO^- & NH_3^+ R_1	COO^- R_2	NH_3^+ R_3	OH R_4
Average Depth (nm)	3.8	3.4	7.5	7.5
Standard Deviation (nm)	1.9	2.0	0.6	0.9
Average Swelling (nm)	4.1	4.5	0.4	0.4

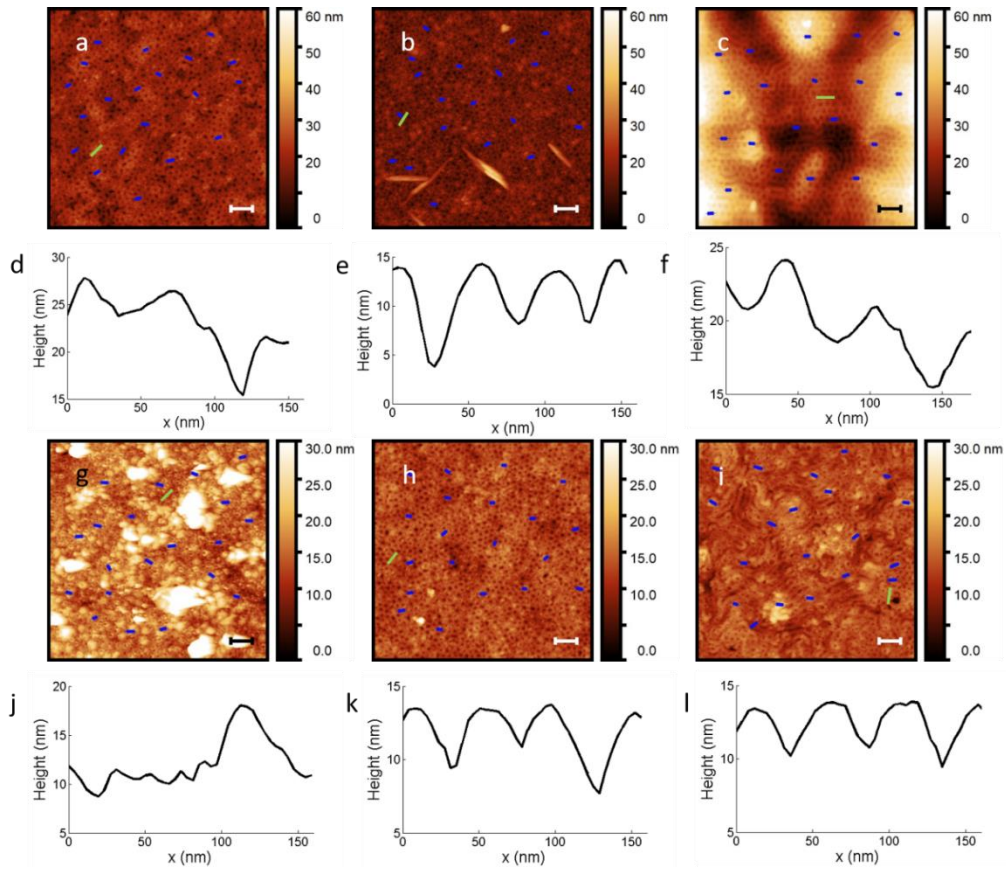

Figure A3.2: Representative AFM height profiles with marked cylinders in blue for confined inorganic measurement of (a) **Cu_2O-iSTAMPR$_2$**, (b) **Cu_2O-iSTAMPR$_3$**, (c) **Cu_2O-iSTAMPR$_4$**, (g) **ZnO-iSTAMPR$_2$**, (h) **ZnO-iSTAMPR$_3$**, (i) **ZnO-iSTAMPR$_4$**, with corresponding line profiles from 3 cylinders shown as green line in corresponding AFM height profile (d) **Cu_2O-iSTAMPR$_2$**, (e) **Cu_2O-iSTAMPR$_3$**, (f) **Cu_2O-iSTAMPR$_4$**, (j) **ZnO-iSTAMPR$_2$**, (k) **ZnO-iSTAMPR$_3$**, (l) **ZnO-iSTAMPR$_4$**

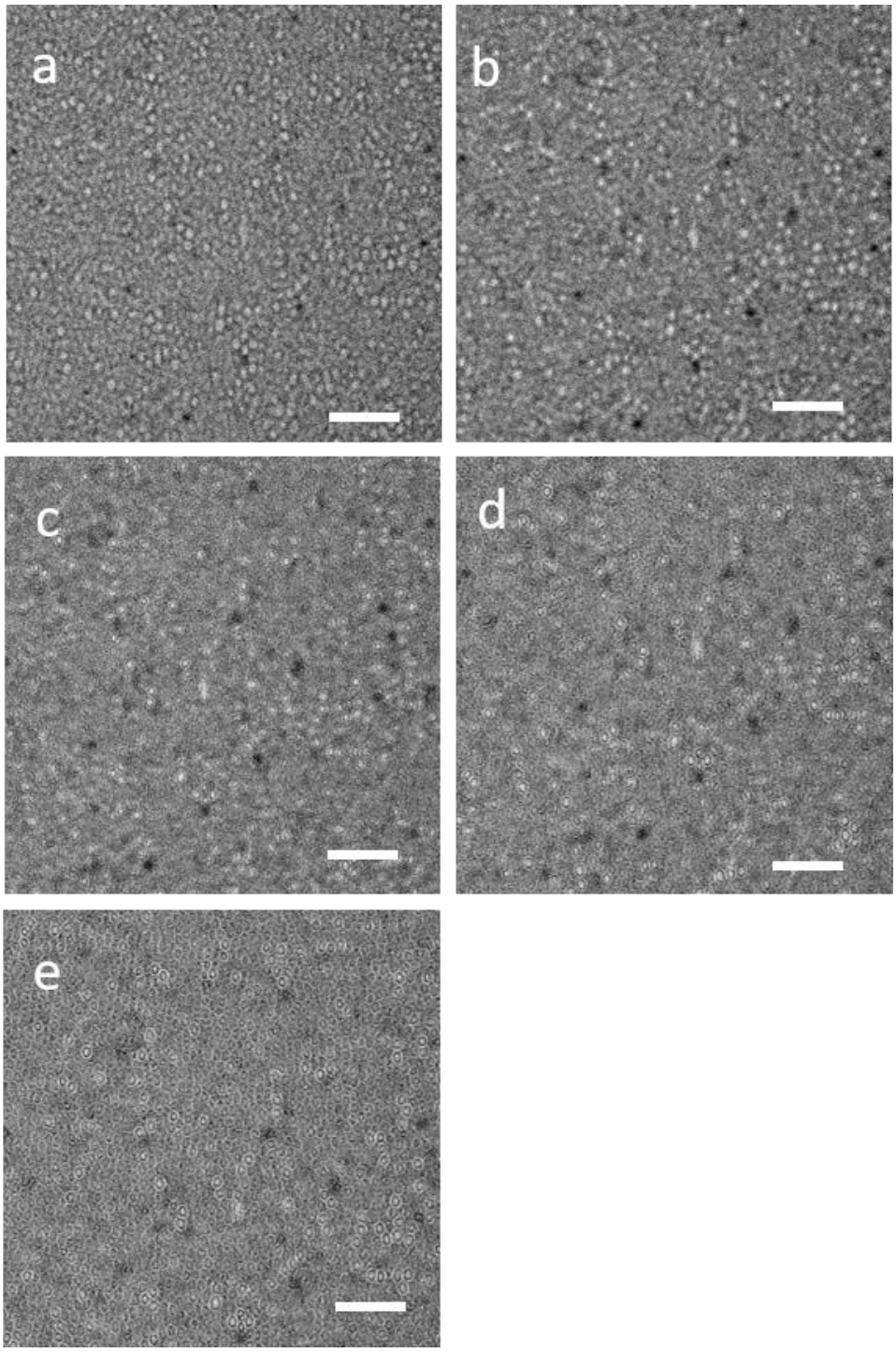

Figure A3.3: Defocus series of bright field TEM images of **ZnO-iSTAMPR$_2$** with a defocus of (a) -20 µm, (b) -10 µm, (c) 0 µm, (d) 10 µm, (e) 20 µm scale bars 500 nm

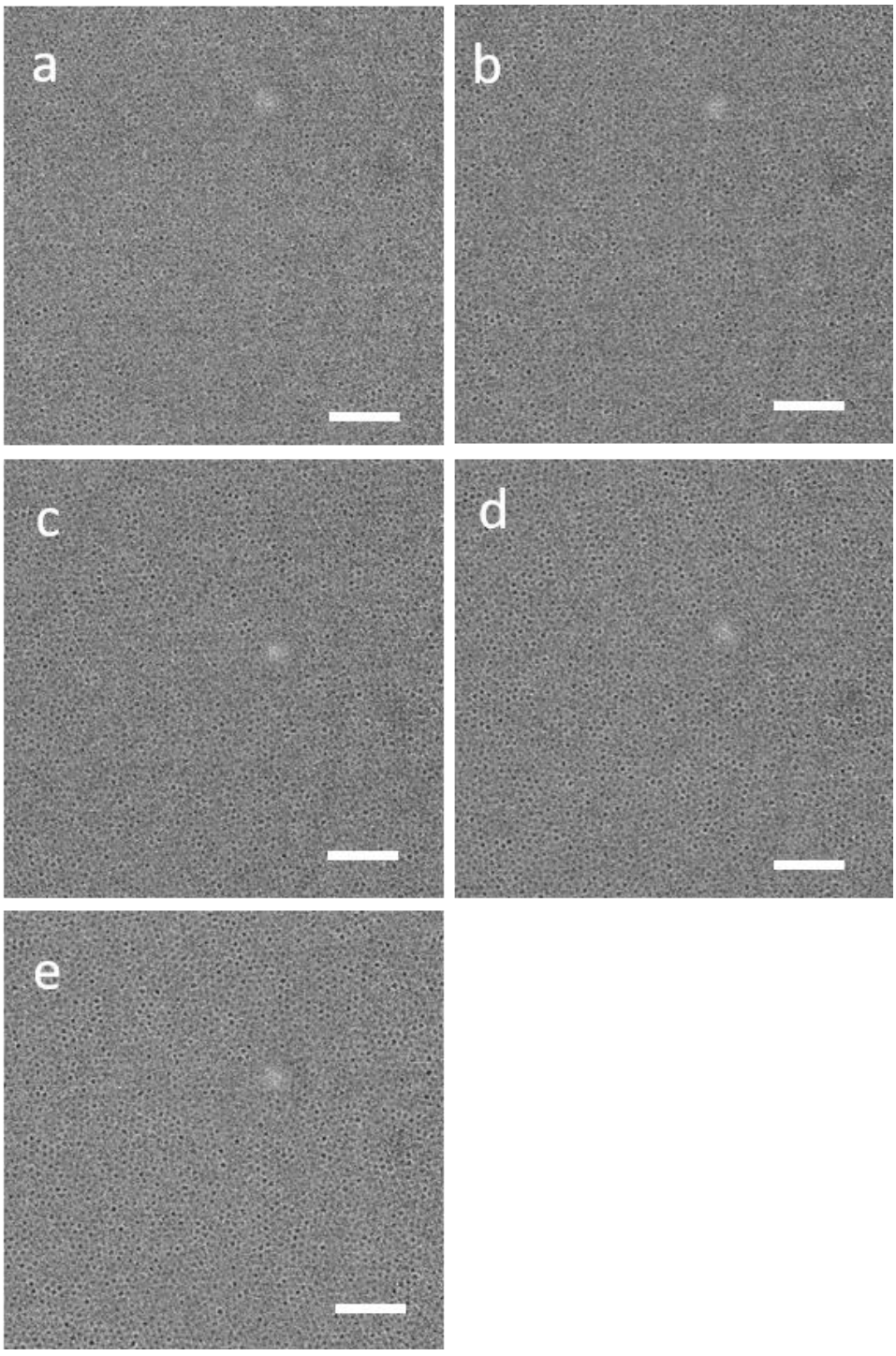

Figure A3.4: Defocus series of bright field TEM images of **ZnO-iSTAMPR$_3$** with a defocus of (a) -20 µm, (b) -10 µm, (c) 0 µm, (d) 10 µm, (e) 20 µm scale bars 500 nm

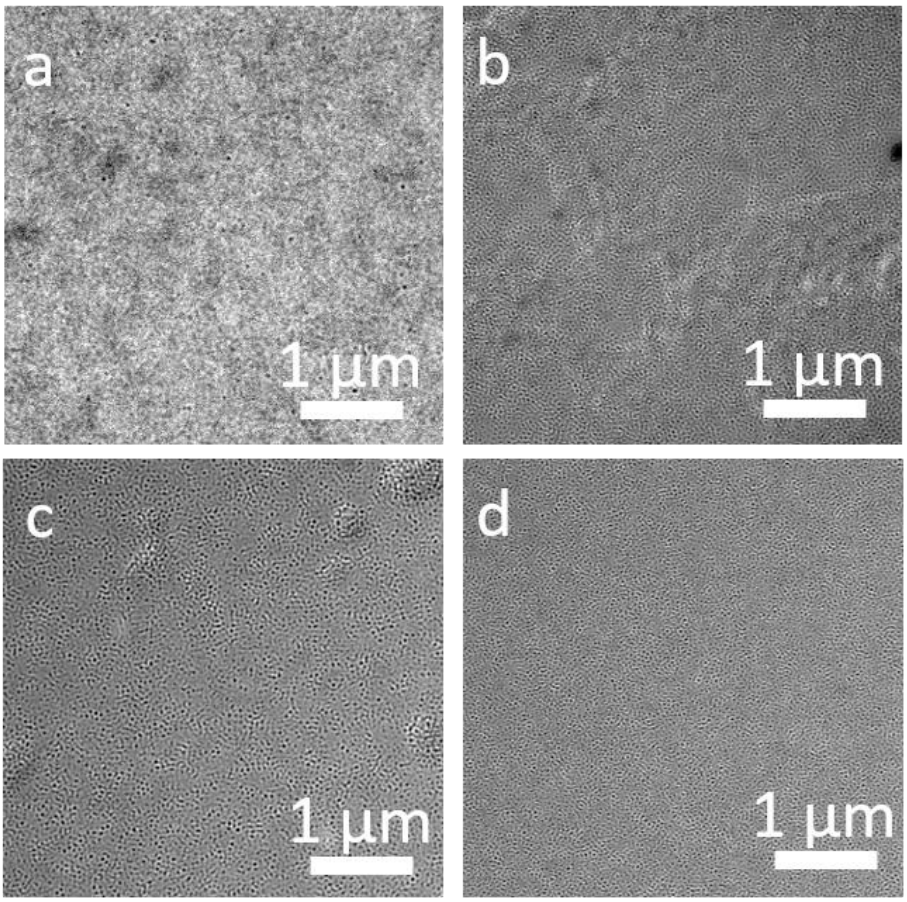

Figure A3.5: Zoomed out Bright field TEM images of (a) **ZnO-iSTAMPR$_1$**, (b) **ZnO-iSTAMPR$_2$**, (c) **ZnO-iSTAMPR$_3$**, (d) **ZnO-iSTAMPR$_4$**

Table A3.2: GISAXS characterization of iSTAMP templates.

Sample	q*(A^{-1})	d (nm)	cylinder-cylinder (nm)
iSTAMP0	0.014	45	52
Cu_2O-iSTAMPR$_1$	0.014	45	52
Cu_2O-iSTAMPR$_2$	0.014	45	52
Cu_2O-iSTAMPR$_3$	0.014	45	52
Cu_2O-iSTAMPR$_4$	0.014	45	52
ZnO-iSTAMPR$_1$	0.014	45	52
ZnO-iSTAMPR$_2$	0.014	45	52
ZnO-iSTAMPR$_3$	0.014	45	52
ZnO-iSTAMPR$_4$	0.014	45	52

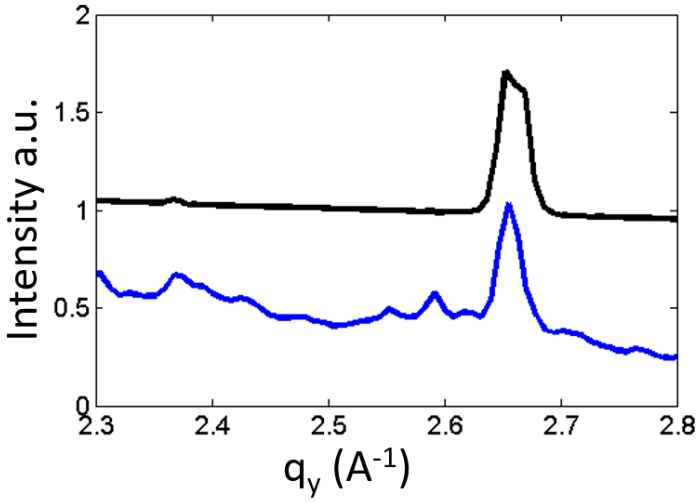

Figure A3.6: Integrated (100) GIWAXS ring and arc for peak width comparison of (blue) **ZnO-iSTAMPR$_2$** and (black) **ZnO-iSTAMPR$_3$**

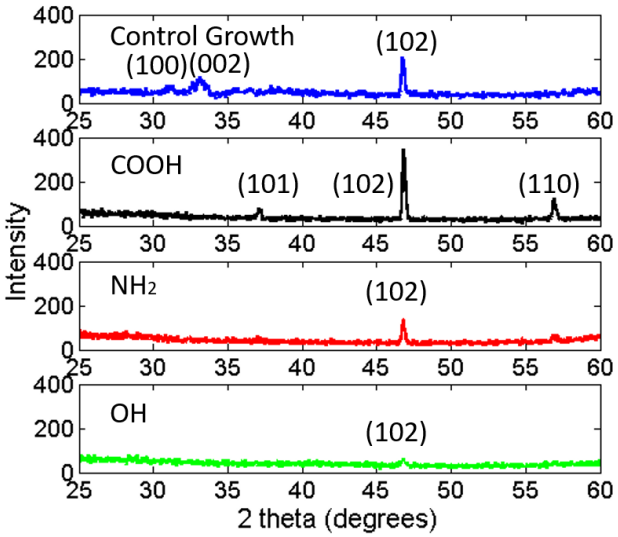

Figure A3.7: pXRD patterns of ZnO control growth on glass slide, **ZnO-iSTAMPR$_2$**, **ZnO-iSTAMPR$_3$**, **ZnO-iSTAMPR$_4$** (JCPDS No. 36-1451)

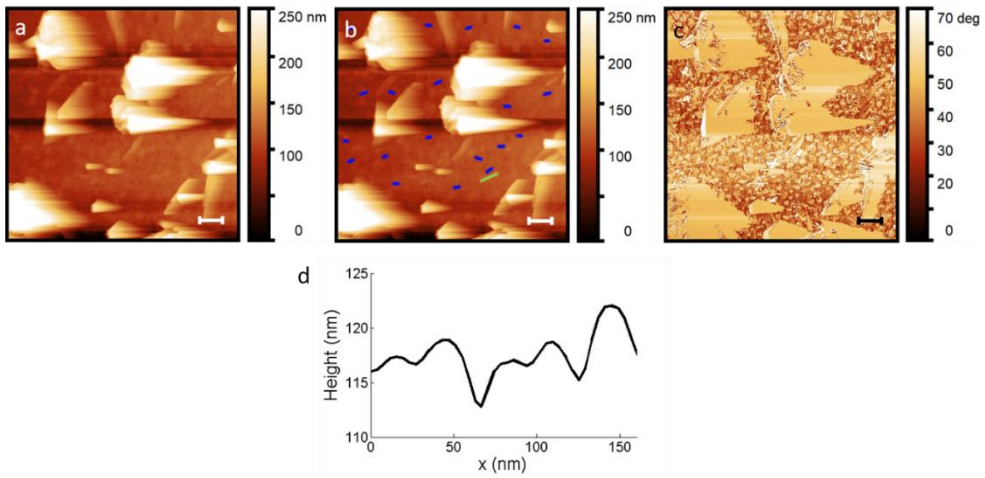

Figure A3.8: Representative AFM image of **Cu_2O-iSTAMPR$_1$** (a) height profile (b) height profile with marked cylinders in blue for confined inorganic measurement (c) phase profile (d) line profile from 3 cylinders shown as green line in (b)

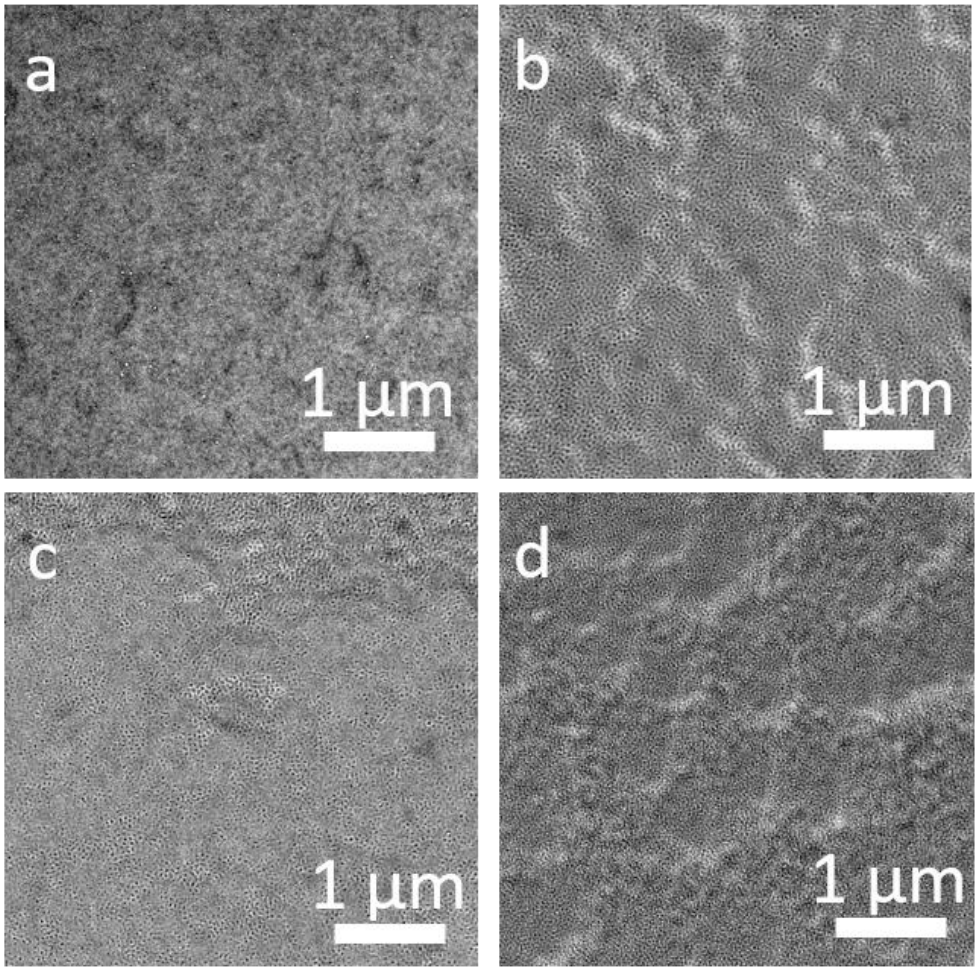

Figure A3.9: Zoomed out Bright field TEM images of (a) **Cu_2O-iSTAMPR$_1$**, (b) **Cu_2O-iSTAMPR$_2$**, (c) **Cu_2O-iSTAMPR$_3$**, (d) **Cu_2O-iSTAMPR$_4$**

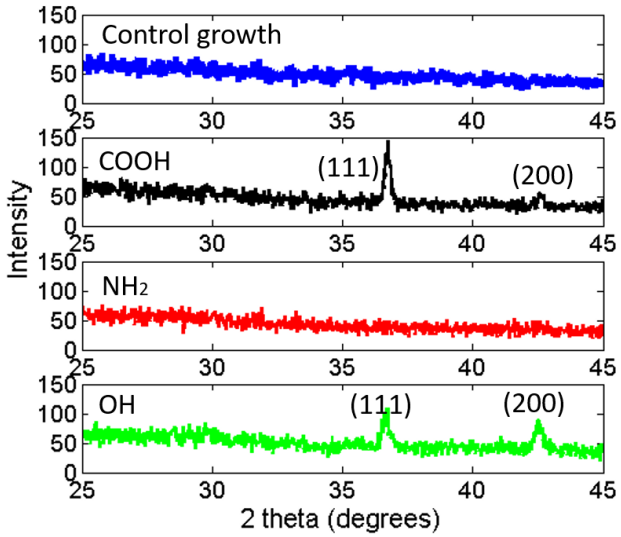

Figure A3.10: pXRD patterns of Cu_2O control growth on glass slide, **Cu_2O-iSTAMPR2**, **Cu_2O-iSTAMPR3**, and **Cu_2O-iSTAMPR4** (JCPDS No. 05-0667)

CHAPTER FIVE

CONCLUSIONS

This thesis presented a versatile approach employing thin film block copolymer self-assembly and subsequent use of click chemistry spatially confined to only one of the blocks to prepare nanostructured surfaces as templates for spatially confined surface reactions directing the nucleation and growth of two transition metal oxides. This method is referred to as surface templating on assembled mesostructured polymers, or simply "STAMP". My methods studied four nanoconfined organic functionalities: cysteine with both COO^- and NH_3^+, COO^-, NH_3^+, and OH, and their effect on the nucleation and growth of the inorganic phase. The results demonstrate that the inorganic crystallinity, texturing, and orientation is controlled by (i) the attached functional group confined to one of the blocks, the P(EO-*co*-AGE) block, in the thin film, (ii) the functional group's interaction with the respective transition metal oxide, and (iii) the location of the initial nucleation and growth of the inorganic.

In Chapter 2, studies demonstrate that a PS-*b*-P(EO-*co*-AGE) block copolymer can be self-assembled into thin films and subsequently be functionalized via thiol-ene click chemistry specifically only in the P(EO-*co*-AGE) block. This process was demonstrated through the successful localized attachment of either cysteine or ultrasmall silica nanoparticles onto the block copolymer surface as demonstrated using various thin film characterization techniques. The reactive block copolymer surface approach to confined chemistries overcomes limitations of bulk approaches in terms of finding solvents compatible with both hydrophobic and hydrophilic chemistries and leads to short reaction times.

Chapter 3 introduced the ability to nanopattern the nucleation and growth of two transition metal oxides at low temperatures and atmospheric pressure onto the

cysteine functionalized surfaces that were described in Chapter 2. Cu_2O or ZnO only nucleates and grows on the block copolymer surface post-functionalization, indicating that block copolymer phase separation between hydrophilic and hydrophobic blocks alone is not sufficient to confine inorganic materials growth. Studies in this chapter also show that the resulting nanostructured, confined inorganic is crystalline.

Chapter 4 utilizes the versatility of the block copolymer thin film thiol-ene click chemistry to first change the functionality of the hydrophilic block from containing both COO^- and NH_3^+ groups to containing either COO^-, NH_3^+, or OH functional groups, and subsequently to show how surface chemistry variations change the final inorganic crystal texturing and orientation. In addition, we performed a time dependent study of inorganic growth to gain insights into the early stages of inorganic structure formation. These experiments yielded information about the combined effects of topology and chemical functionality on the final crystallographic texture of the inorganic material.

Based upon these studies, general mechanistic insights regarding nanopatterned nucleation and growth of transition metal oxides are elucidated. This thesis has demonstrated that thiol-ene chemistry can be applied to block copolymer thin films via the developed STAMP method. Chapter 2 demonstrated that small molecules and nanoparticles can be confined to the reactive block. Building on this result, an interesting direction for this work is attaching a wider range of water-soluble thiol-terminated, di-, tri-, and even longer oligopeptides to expand the diversity of surface functionalization. It is important when moving to longer oligopeptides that the thiol group is not a side chemical functionality but is one of the terminating ends. When the thiol is a side group, the reaction time is significantly longer because it is less chemically available then when it is a terminating end group. A feasible route to functionalizing the peptide with a thiol end group is to attach 3-mercaptopropionic

acid to the N-terminus of the respective peptide. The N-terminus has an amine group that reacts with the carboxylic acid group in the 3-mercaptopropionic acid when activated by 2-(1H-benzotriazol-1-yl)-1,1,3,3-tetramethyluronium hexafluorophosphate (HBTU) and N, N-diisopropylethylamine (DIEA) in dimethylformamide (DMF) while the synthesized peptide is still loaded onto the PS resin. The terminal thiol can be visibly detected with 2,4,6-trinitrobenzenesulfonic acid and once the peptide is cleaved off the PS resin and worked up, HPLC, GPC, and NMR can be performed to help determine if the termination reaction went to completion as well as if all amino acids from the desired sequence. In addition, the time to attach oligopeptides to PS-*b*-P(EO-*co*-AGE) in bulk using thiol-ene chemistry increases as the size of the oligopeptide increases using DMPA as the photoinitator, even when the N-terminus is functionalized with a thiol. It may be possible to decrease the reaction time by changing the photoinitiator or increasing the amount of AGE in the copolymer. If an initiator is selected that goes into aqueous solutions or alcohol solutions exclusively, one may be able to decrease the reaction time. For the surface chemistry reactions, if there are more alkene groups present, it is more likely that larger and larger molecules will become attached. The decrease in reaction time should be seen in both bulk and surface chemistry reactions. Therefore, bulk reactions could be run first in order to determine whether the initiator was worth pursuing or not compared to the DMPA benchmark. In addition, the vast literature on biomineralization regarding sequence-specificity for directing the growth of a range of biominerals, such as hydroxyapatite and iron oxides, opens the opportunity to now explore, in a controlled geometry, the combined influence of nanoconfinement, chemical sequence, and geometry on directing the growth of oriented arrays of crystals. It may also open the possibility to develop routes to large mesostructured single crystals.

Chapters 3 and 4 demonstrated that the functional group confined within the minority block of the hexagonally packed, standing up cylinder morphology dictates the resulting crystallinity, texturing, and orientation. But what happens to the inorganic nucleation and growth when we change the block copolymer thin film morphology? The BCP morphology can be changed by changing the relative weight fractions between the PS and P(EO-*co*-AGE) blocks or in the future any additional blocks added to the base di-block copolymer. Additional BCP morphologies can be explored when expanding the system to tri-block terpolymers. Poly(isoprene)-*block*-poly(styrene)-*block*-poly(ethylene oxide-*co*-allyl glycidyl ether) (PI-*b*-PS-*b*-P(EO-*co*-AGE), has already been synthesized in the Wiesner group, but further exploration is needed in assembling and functionalizing it into a thin film. Because of the PI block, the polymer is no longer soluble in benzene and therefore must be spin coated in other solvents, e.g. tetrahydrofuran. Some likely candidates for annealing solvents to assemble the BCP into a thin film are benzene, toluene, tetrahydrofuran, chloroform, and acetone.

Chapter 4 also explores the mechanism of the nucleation and growth pathway of Cu_2O and ZnO on various functionalized block copolymer surfaces. Further exploration of these ideas requires a technique such as *in-situ* AFM to observe and answer additional questions about the early stages of growth and pattern development on PS-*b*-P(AGE-*co*-EO) functionalized thin films. For example, some unanswered questions include whether growth proceeds via the assembly of particles or clusters from solution? Does this growth process change when the surface functionality is changed, as is suggested by the results in Chap. 4? Spatially where does growth begin and how does it proceed to fill in the patterns? One can start to answer some of these questions by preparing surfaces with attached peptides that are known to chelate to metal ions to nucleate and grow an inorganic or peptides that are known to chelate to a

certain facet of the respective inorganic. Once these surfaces are prepared, *in-situ* AFM growth experiments should be able to determine whether the ions chelate to the peptide and then nucleate and grow in the template or if the inorganic first forms clusters in solution and then those clusters chelate to the peptide. By observing growth in real-time, it could be possible to observe more in depth if it is the chemistry or this topology that drives the location of the initial deposition. At later stages of growth, *in-situ* AFM could more precisely measure deposition rates as a function of solution supersaturation and substrate functionalization. These types of experiments would establish a feedback loop for the organic and inorganic synthesis methods that I have developed, in terms of block copolymer composition, post-polymeric functionalization, and inorganic growth conditions.

To exploit the power of directed self-assembly to prepare mesostructured, hierarchical composite materials with new functions, we need a fundamental understanding of formation mechanisms that lead to the nano-to-mesoscale structures of organic-inorganic assemblies. Studying their nucleation and growth pathways offers insight into crystallinity, texturing, and orientation control at inorganic-organic interfaces. Applying biomineralization concepts to my STAMP and iSTAMP methods can inspire new synthesis approaches for generating organic-crystalline inorganic composites with novel materials properties and has the potential to be broadly applied to a range of inorganic materials. This thesis has provided a starting platform for future nanopatterned organic driven inorganic crystal growth approaches for understanding and controlling inorganic crystallinity, texturing, and orientation.